Thesis

Probing the cosmic dawn and the epoch of reionization with statistical properties of the cosmological 21 cm signal: one-point statistics, power spectrum and bispectrum

Hayato Shimabukuro
Division of Particle and Astrophysical Science Graduate School of Science
Nagoya University

February 24, 2016

Abstract

After the cosmic recombination, there have been no luminous objects. This epoch is often called *the Dark Ages*. The Dark Ages ended by the formation of first luminous objects, because first luminous objects illuminated the Universe. According to the standard cosmological structure formation theory, massive objects such as galaxies started to form after the end of Dark Ages, and ionizing photons from galaxies ionized the neutral hydrogen gas distributed in the Universe. This global transition as known the cosmic reionization dramatically proceeded. This epoch is called *the Epoch of Reionization (EoR)*. Recent observations, such as QSO absorption lines, the Lyα luminosity function of galaxies, and the optical depth of Thomson scattering, have provided us with a large amount of information on the EoR. Ongoing and upcoming telescopes will start observation aimed at detecting the 21 cm line signal from the Inter Galactic Medium(IGM) in the EoR. The 21 cm line emission is due to the spin flip of neutral hydrogen atoms.

In this Thesis, I present the method to probe the thermal history of the IGM through the 21 cm signal statistically with future large radio interferometers. First, I present a detailed analysis of the 21 cm power spectrum by considering components which consist of the 21 cm power spectrum in order to investigate what component mainly contributes to the 21 cm power spectrum at each epoch. I also estimate one-point statistics such as variance and skewness of the probability distribution function of the spin temperature to understand physical behavior of the 21 cm power spectrum since previous works did not focus on one-point statistical values in detail. I find that I can give physical interpretation of the 21 cm power spectrum by combining skewness with variance. I also find that skewness becomes good indicator of the epoch in which the X-ray heating becomes effective. Further, I estimate the detectability of skewness with upcoming radio observations.

Then, I introduce the 21 cm bispectrum as a method to probe the Dark Ages and the EoR. The reason why I introduce it is that various astrophysical processes such as Wouthuysen-Field(WF) effect and the X-ray heating of the IGM expected to cause a non-gaussian distribution of the brightness temperature field. I investigate scale and redshift dependences of the 21 cm bispectrum first, then I study what component(the contribution from the matter fluctuation, the spin temperature and neutral hydrogen fraction) and configurations of the 21 cm bispectrum are dominant at the epoch where each astrophysical process plays an important role. I find that the 21 cm bispectrum is scale invariant except the case that dominant component of the 21 cm bispectrum is the matter fluctuation, and find that the squeezed type of the bispectrum as function of redshift has correlation between large and small scales. Further, I find that dependences on configuration and component are different among redshifts. Therefore, I expect that the bispectrum helps us extract the information on each component of the 21 cm bispectrum.

Finally, I perform the Fisher analysis to estimate an expected error for the EoR model

parameters with MWA and LOFAR as supposed instruments. Because previous works showed the 21 cm power spectrum analysis for the expected observation of these telescopes cannot constrain the parameters, I, then, considered how to improve the constraint by using the 21 cm bispectrum. I find that the bispectrum can put tight constraint on the EoR model parameters compared with that obtained by the power spectrum for both telescopes, and thus break the degeneracy.

Acknowledgement

First of all, I would like to express my sincere gratitude to my supervisors Takahiko Matsubara, Naoshi Sugiyama at cosmology laboratory and Keitaro Takahashi at Kumamoto University for their comprehensive discussions and suggestive advices. Under their sometimes kind and sometimes strict tutelage, I could continue my research life for past five years.

I would like to thank Saleem Zaroubi at Kapteyn Astronomical Institute, Matt Jarvis at Oxford University, Stuart Wyithe and Rachel Webster at University of Melbourne for giving me an opportunity to study the basics of radio interferometry and calibration techniques used in radio observations. Thanks to their great hospitality, I could enjoy my stay in Netherlands, UK and Australia and communicate with people in English without hesitation. Also I wish to thank my collaborators; Susumu Inoue at RIKEN, Shuichiro Yokoyama at Rikkyo University, Shintaro Yoshiura at Kumamoto University, and Kiyotomo Ichiki at Nagoya university. Discussion with them and fruitful comments improved my research. I sincerely appreciate Andrei Mesinger at Scuola Normale Superiore instructing how to use 21 cmFAST and giving helpful comments. Further, I appreciate all members of subscience working group *Epoch of Reionization* in SKA JAPAN consortium. Active monthly discussions broadened my outlook and I could learn various topics.

I should thank Paul Geil, Hansik Kim, Ben Mckinley, Bart Pindor, Pietro Procopi, Jaehong Park and Jack Line at University of Melbourne for a useful discussions and helpful comments about data reduction techniques used in MWA group and about state-of-art simulations of the EoR. I notice the importance of the data calibration to detect the 21 cm signal during my stay in Melbourne.

I deeply thank the staff members in Cosmology laboratory and Ω laboratory, Hiroyuki Tashiro, Atsushi Nishizawa, Yuko Urakawa, Sachiko Kuroyanagi, Kenji Hasegawa, Daisuke Nitta and Tsutomu Takeuchi for constructive comments and advices in seminar and daily life. I received a lot of inspirations from their discussions and opinions. I also wish to thank all members in Cosmology laboratory(special thanks to Shohei Saga), Ω laboratory and Ta Laboratory(special thanks to Yuki Tanaka), and Takahashi laboratory at Kumamoto University for daily discussions and private talks.

Finally, I would like to give my deeply gratitude to my family, grand father and mother for supports and encouragements over my life. Thanks to their understanding for my research life and encouragement, I could spend my Ph.D life and open up a new life as a researcher.

I have been supported by Grants-in-Aid for Japan Society for the Promotion of Science(JSPS) Fellow for three years. Thanks to this financial support, I can continue my research life without facing any financial issues. My work is also partially supported by the JSPS Strategic Young Researcher Overseas Visits Program for Accelerating Brain Circula-

tion from the Ministry of Education, Culture, Sports, Science and Technology (MEXT).

Contents

Chapter 1

Introduction

1.1 Historical review of modern cosmology

Here, we briefly give a historical review of modern cosmology from beginning of the Universe to present day. A schematic picture of evolution of the Universe is shown in Fig.1.1. In our understanding, we think that the Universe began by the accelerating expansion called *inflation* [114, 54]. At the epoch of inflation, it is thought that quantum fluctuations, which are seeds for the large scale structure in the Universe, are embedded. After inflation, the Universe keeps much dense and hot state because energy of inflation changes to thermal energy (*reheating*). Due to the expansion of the Universe, the Universe gets cooled less than $\sim 0.1\mathrm{MeV}(\sim 10^9\mathrm{K})$. At this time, protons and neutrons start to produce deuterium($p+n \to D+\gamma$). Once deuterium is produced, reactions to produce ^{3}H,^{3} He,^{4} He via deuterium begin to occur. In addition to these elements, ^{7}Li is also produced. A series of these processes is called *BigBang nucleosynthesis* (BBN) [2, 3]. At the early Universe, photons remain tightly couple to electrons via Compton scattering and electrons remain couple to protons via Coulomb scattering. Below $T \sim 0.1\mathrm{eV}(\sim 10^4\mathrm{K})$, free electrons are coupled with protons and hydrogen atoms are produced via $e^- + p \to H + \gamma$. This reaction is called *recombination*. At almost same time, an interaction between photons and baryons becomes inefficient, and then photons are decoupled from baryons after last scattering. The photons after last scattering can travel to us and these photons are called *Cosmic microwave background radiation* (*CMB*, *CMBR*). Since there are no luminous objects after recombination, this epoch is called *the Dark Ages (DA)* and the Universe keeps neutral state at this epoch. At $z \sim 30$, first generation luminous objects begin to form inside a dark matter halo. As the result, these ones illuminate the Universe and this period is called *the Cosmic Dawn(CD)*. As structure formation proceeds, ionizing photons emitted by galaxies start to ionize neutral hydrogen atoms in the Universe around $z \sim 15$. This epoch is called *the Epoch of Reionization (EoR)*. Recent observations suggest that the EoR finishes by $z \sim 6$. After the EoR finishes, the Universe experiences some important events. One of them is the accelerating expansion of the Universe. Observations of supernovae indicate that the accelerating expansion of the Universe starts at $z \sim 0.5$. If the Universe consists of only matters which interact each other gravitationally, we cannot explain this accelerating expansion. Consequently, we introduce *the dark energy* to explain this accelerating expansion. Other important discovery is existence of the large scale structure in the Universe. A number of large surveys of galaxies finds that galaxies are not distributed

randomly but have structure on the large scale.

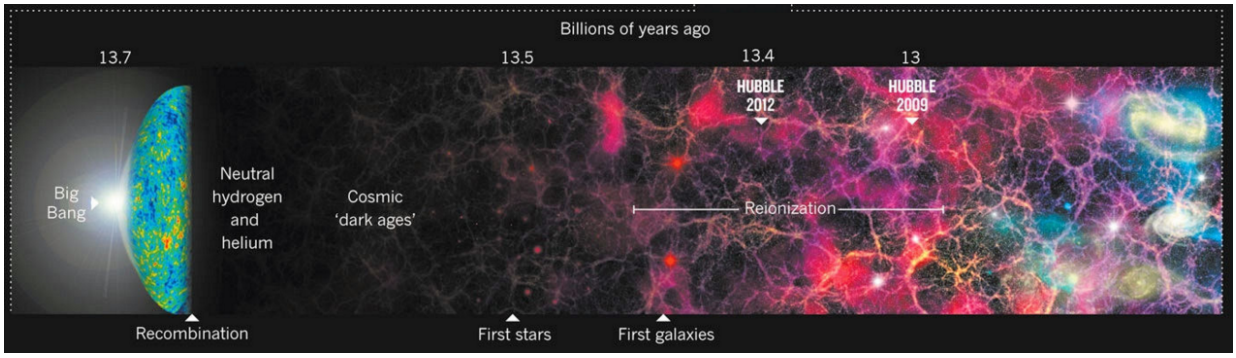

Figure 1.1: History of the Universe. From left to right, the Universe evolves. *credit*: https://the Universe-review.ca

We here briefly see observational evidences for modern cosmology. Through the end of 20th century to 21st century, Our knowledge on the Universe has increased rapidly thanks to development of observational instruments. First, we introduce observational results which confirm BBN[14]. Primeval ^{4}He abundance is estimated from measurements of ^{4}He/H in hot and ionized regions of galaxies. D is measured vis absorption lines in spectrum of distant QSOs($z \sim 2-3$). Primeval ^{7}Li abundance is measured from the atmospheres of oldest stars in our galaxy. However, most robust and precise estimate of the abundance of these primeval elements is brought by baryon to photon ratio measured by the CMB anisotropies. Thus, we show predicted abundance of these primeval elements obtained by the CMB in Fig.1.2.

Next, we introduce observations of the CMB. Big discoveries are brought by COsmic Background Explore (COBE) satellite. They succeed in finding anisotropies of the CMB temperature($\delta T/T \sim 10^{-5}$) and in determining the spectrum of the CMB precisely[10, 39, 120]. The latter shows that CMB photons are perfect blackbody radiation with $T_{\gamma,0} = 2.725 \pm 0.001$K. After COBE, Wilkinson Microwave Anisotropy Probe (WMAP)[121] and Planck[98, 99] are launched to observe the anisotropies of the CMB with higher spacial resolution. These satellites can measure the anisotropies of the CMB and determine the cosmological parameters accurately. We show the comparison of the CMB temperature maps observed by each satellite in Fig.1.3.

Finally, we show result of observations which measure the distribution of galaxies. The large and deep redshift surveys find that the distribution of galaxies is not random and the Universe has the large scale structure(see eg.[31, 32, 125]). As similar as case of the CMB, this discovery also suggests that the Universe needs the deviation from smoothness. One of the most important statistical values to estimate the density (or temperature) fluctuations is a two-point correlation function (or called power spectrum in Fourier space). We also can measure scale of the Baryon Acoustic Oscillation(BAO) by the two-point correlation function(see eg. [125]).

These observations open up a new research and precision cosmology. We can establish the ΛCDM model. The three pillars of the ΛCDM model are

(*i*) *Dark matter and dark energy.*

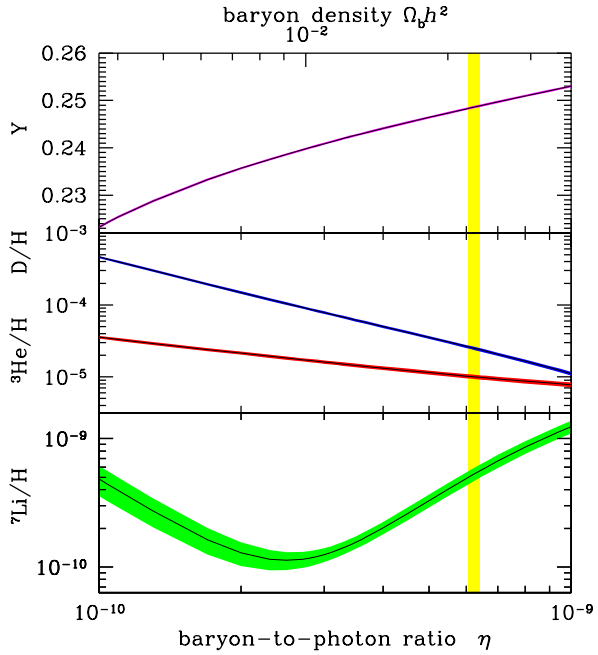

Figure 1.2: This figure shows abundance of each primeval element (^{4}He, D, ^{3}He,^{7} Li from top to bottom) as function of baryon to photon ratio. This relation is predicted by Bigbang nucleosynthesis. The vertical band is range of baryon to photon ratio measured by the CMB. Once we determine baryon to photon ratio, we can estimate abundance of each primeval element. This figure is taken from [38].

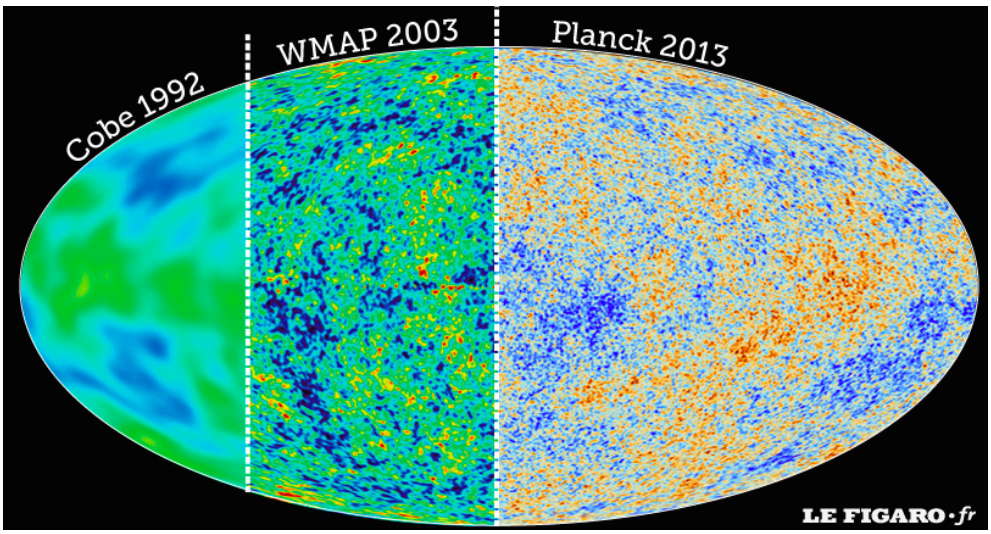

Figure 1.3: Comparison of the CMB temperature maps observed by COBE, WMAP and PLANCK satellites. The resolution becomes better from left to right. *credit*: http://www.legaro.fr

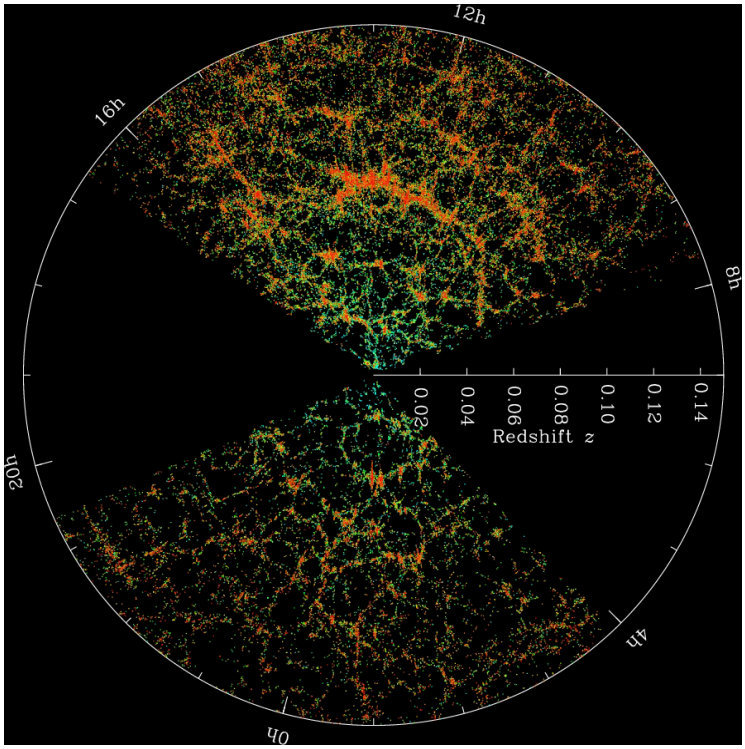

Figure 1.4: SDSS map of the Universe. Each point expresses a galaxy.(*credit*): http://www.sdss.org/science/

(ii) The perturbation theory around zeroth order for density fluctuations to describe the structure formation in the Universe.

(iii) The inflation model to generate the initial quantum fluctuations.

Based on the ΛCDM model, we can consider the evolution of the Universe. The ΛCDM model is a paradigm for the modern cosmology confirmed by both theory and observation.

1.2 Through the Dark Ages to the EoR

We previous referred to the history of the Universe. We here focus on epochs through the Dark Ages to the EoR since these epochs are the frontier for both observation and theory. Recent observations of QSO, CMB and high redshift galaxies constrain neutral hydrogen fraction at the EoR. Observations of distant QSO spectra and the luminosity function of high redshift galaxies indicate that the EoR finishes by $z \sim 6$. On the other hand, An observation of the CMB polarization caused by Thomson scattering implies that the EoR happens at $z \sim 9 - 10$ (see sec 3.2.1 in detail). We show current constraints on fraction of neutral hydrogen atoms obtained by observations in Fig.1.5. Although these observations give constraints on the EoR, we have yet to observe an epoch through the Dark Ages to the EoR. Since we cannot check validness of a theoretical scenario without comparison of theory with observation, we need to observe the epoch through the Dark Ages to the EoR

in detail.

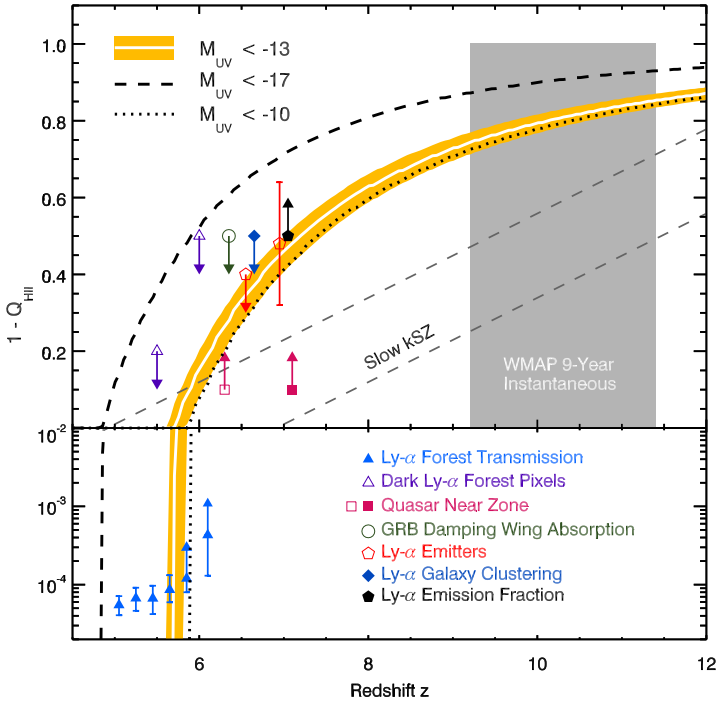

Figure 1.5: Constraint on neutral fraction $1 - Q_{\rm HII}$ as function of redshift obtained by observations(Lyα forest, Lyα galaxies, GRB, QSO). Each point corresponds to various observations. This figure is taken from[108].

Next, we briefly introduce a scenario through the Dark Ages to the EoR. Based on a hierarchical structure formation model, matter fluctuations grow gravitationally and dark matter collapses. Collapsed dark matter makes a dark matter halo at over-dense regions. Inside a dark matter halo, baryonic objects start to form primordial stars at $z \sim 30$[142]. At the epoch when primordial stars form, there are no metals and only hydrogen atoms (and helium) exist. In particular, primordial gas can be cooled via hydrogen molecular cooling. As the result, the gas also collapses and then primordial stars can form. The Cosmic Dawn starts when first luminous objects start to illuminate the Universe. Once the Cosmic Dawn starts, various luminous objects such as supernova, quasar and X-ray binary form. These objects affect not only thermal history of the IGM but also ionization history of the IGM[35, 36, 133, 113]. The temperature of the IGM first decreases adiabatically as the Universe evolves. However, the IGM is heated drastically by X-ray photons after a certain epoch when X-ray sources such as X-ray binaries form. As the Universe evolves more, neutral hydrogen atoms in the Universe are reionized by ionizing photons emitted by galaxies[34].

We expect that next generation optical and infrared telescopes such as JWST(James Webb Space Telescope) and TMT(Thirty Meter Telescope) can give fruitful information on the neutral hydrogen fraction during the EoR by observing high redshift galaxies beyond $z \sim 10$. However these observations are also limited because they can observe the IGM indirectly, thus we need to observe the IGM directly. The 21 cm signal is believed to be

a good probe of the EoR because the 21 cm signal can trace the distribution of neutral hydrogen atoms during the EoR and beyond the EoR. We expect that we can measure the formation and evolution of ionized bubbles via the 21 cm signal.

1.3 21 cm line of neutral hydrogen

As we referred above, current observations for the EoR can access only the IGM at late stage of the EoR. Thus, we need other observations to be able to access the IGM at the EoR and the Cosmic Dawn. The 21 cm line emission due to the hyperfine structure of a neutral hydrogen atom serves as a promising method to investigate the epoch we are interested in. A neutral hydrogen atom emits or absorbs the radio wave corresponding to the energy difference between the singlet and the triplet in neutral hydrogen. This energy difference corresponds to 1420MHz or λ $\sim$21 cm wavelength radio wave. The transition probability between the singlet and the triplet for a hydrogen atom is $\sim 2.9\times10^{-15}\mathrm{s}^{-1}$. This probability is very small, but hydrogen atoms constitute the bulk fraction of the Universe. Therefore, we can access the IGM at the EoR and the cosmic dawn via the 21 cm signal.

The redshifted 21 cm line is suitable for studying thermal and ionized states of the IGM as well as the first objects in the Cosmic Dawn and the EoR [43, 106, 117]. The redshifted 21 cm line has rich information on the IGM. The fundamental value of the 21 cm line is the spin temperature which is determined by the CMB temperature, the kinetic temperature of the IGM and the color temperature of the Lyman alpha (Lyα) radiation field(the color temperature corresponds to the number of Lyα photons). The kinetic temperature decreases adiabatically as the Universe evolves when there are no heating sources. Once X-ray sources such as X-ray binaries form, the IGM begins to be heated by X-ray photons and the gas kinetic temperature increases drastically [89, 20, 104, 36]. Typically, the color temperature is nearly equal to the kinetic temperature because the Lyα scattering rate is very high and a frequent scattering of Lyα photons brings the Lyα radiation field coupling with the IGM whose temperature is equal to the kinetic temperature [43]. The spin temperature of neutral hydrogen atom couples with the color temperature via Lyα photons (called the *Wouthuysen-Field (WF) effect*[139]). Therefore, the spin temperature also couples with the kinetic temperature. Because of this coupling, the spin temperature coupled with the kinetic temperature also increases drastically after X-ray sources form, and exceeds the CMB temperature. As the heating of the IGM proceeds, the thermal phase of the IGM changes and neutral hydrogen atoms start to be reionized by UV radiation from early galaxies [79]. Note that we actually observe the brightness temperature not the spin temperature. The brightness temperature is the spin temperature offsetting from the CMB temperature and is governed by fraction of neutral hydrogen atoms, matter fluctuations and the spin temperature. Therefore, we can extract information on both thermal and ionization state of the IGM from the brightness temperature.

Ongoing radio interferometers, such as Low Frequency Array (LOFAR) [110], Murchison Wide Field Array (MWA) [126], and Precision Array for Probing Epoch of Reionization (PAPER) [101], start observation and serve as a prototype of future high-sensitivity experiments (Fig.1.6). However, the sensitivities of the ongoing experiments are not yet sufficient to obtain image maps of the distribution of neutral hydrogen atoms at the Cosmic Dawn

and the EoR. Alternatively, we try to detect the 21 cm signal statistically. One of the statistical methods to extract the information on physical state of the IGM from the 21 cm line is the power spectrum of the brightness temperature. [43, 104, 112, 4, 90, 102]. The power spectrum of the 21 cm signal might be detectable by ongoing radio interferometers [90]. Recent observations already constrain the 21 cm power spectrum and the IGM temperature at high redshift [29, 1, 51].

Although recent observations put a loose constraint, it is expected that the 21 cm power spectrum at $z = 10 \sim 30$ can be measured much more accurately by the Square Kilometre Array (SKA)[15]. SKA is also expected to have efficient specification to obtain image maps of HI distribution. Furthermore, we can measure the state of the IGM by other method with SKA. The method to measure power spectrum and image maps is based on 21 cm emission lines, whereas another method uses 21 cm absorption lines. When we observe spectrum of high-z radio background source, the 21cm absorption lines are seen in the spectrum. The 21 cm absorption lines reflect distribution of neutral hydrogen atoms along line of sight. This method is similar to the Lyα forest except using the 21 cm absorption lines instead of Lyα absorption lines. Therefore, this method is called the 21 cm forest [40, 21] and SKA is capable to detect the 21 cm forest.

Figure 1.6: Pictures of the antenna configuration of LOFAR(left) and MWA(right). *credit*: (left) Astron[http://www.rug.nl] and (right) Natasha Hurley-Walker[http://www.mwatelescope.org].

However, there remain some challenging problems to detect the 21 cm signal. In particular, foreground removal is a big issue for extracting the 21 cm signal from the total signal (21 cm signal+foreground+thermal noise) [66, 67, 128]. Here, foreground includes Galactic diffuse synchrotron emission, emission from supernova remnant, diffuse free-free emission from our galaxy and extragalactic foregrounds such as radio galaxies. We show the simulated 21 cm signal, foreground and thermal noise with LOFAR in Fig.1.7. Since foreground is an 5-6 orders of magnitude greater than the 21 cm signal, we need to remove foreground appropriately. In order to remove foreground, some methods such as a polynomial fitting, correlated component analysis(CCA), Wp smoothing and GMCA are suggested as algorithms to remove foreground [17]. On the other hand, some approaches try to avoid foreground instead of removal. In this point of view, they measure the 2D(transverse and line-of-sight components in Fourier space)-21 cm power spectrum in the region *the EoR*

window which is free from effect of foreground[100, 74, 75, 30]. Here we show a schematic image of the EoR window in Fig.1.8. The two methods, foreground removal and foreground avoidance, for the recovery of the spacial 21 cm power spectrum are complementary to each other. For the current observation noise levels, foreground avoidance recovers large k scales well and foreground removal recovers small k scales well. As for SKA-level noise, foreground removal can work well both at large k and small k[16]. As well as development of instruments, algorithms for foreground removal and avoidance is going to be improved. Thus, we expect that the 21 cm signal is detectable near future.

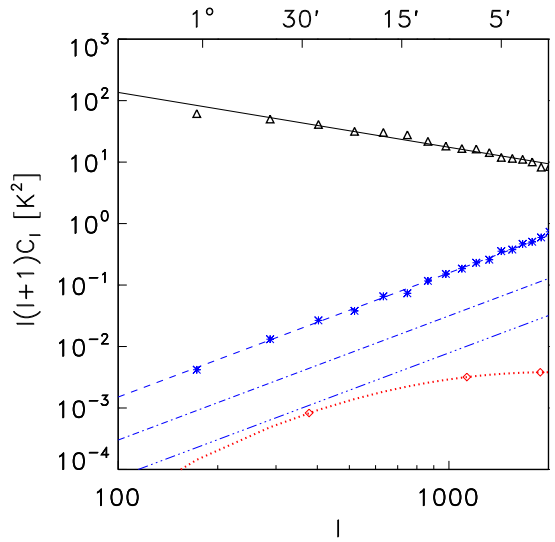

Figure 1.7: Angular power spectra of the simulated EoR signal(dotted redline), simulated foreground(solid black line) and three levels of simulated noise for LOFAR. The dashed line is noise for single beam line with one year of integration time, the dash-dotted line is noise for five beams with one year of integration time and the dashed-dotted-dotted line represents noise with five beams after four years of integration time. This figure is taken from [66].

1.4 Outline of this Thesis

In this Thesis, we studied the cosmological 21 cm line signal which is a powerful tool to know the state of the IGM at the Dark Ages and the EoR. It is important to extract the information on the IGM from the 21 cm signal. Some ongoing telescopes such as MWA and LOFAR have already started observation to detect the cosmological 21 cm signal. Future observations like HERA and SKA, planned to start observation in 2020s, are expected to reveal the evolution of the Universe through the Dark Ages and the EoR to present. The 21 cm cosmology fascinates us because it opens up a new window for the high-z Universe.

Considering the above benefits, we investigated statistical methods to extract the information on both the thermal and ionization histories of the IGM by using the cosmological 21 cm signal in preparation for detection of the cosmological 21 cm signal statistically.

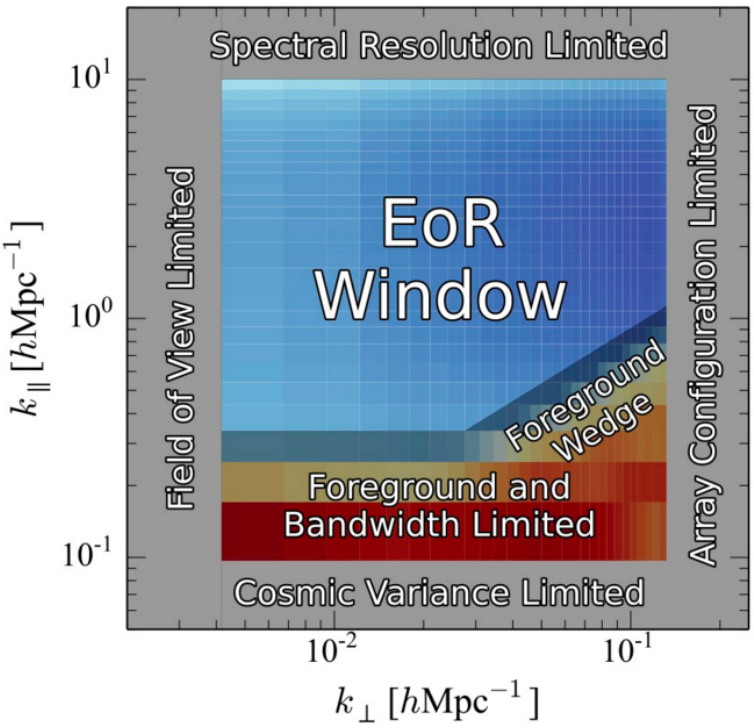

Figure 1.8: EoR window. Larger $k_\perp$ is limited by the array configuration (spacial resolution) and smaller $k_\perp$ is limited by the Field of View(FoV). Large $k_\parallel$ is limited by the spectral resolution and smaller $k_\parallel$ is limited by foreground and the bandwidth. This figure is taken from [74].

First, we proposed a one-point statistics, such as the variance and skewness, as an indicator to approach the thermal history of the IGM. We focused on the variance and skewness of the spin temperature because the thermal information on the IGM is included in the spin temperature. Consequently, we calculated one point statistics values and discussed how these statistical values would give the information. We also estimated the signal to noise ratio of skewness assuming MWA, LOFAR and SKA.

Second, we calculated the bispectrum of the brightness temperature. Since astrophysical processes are expected to introduce a non-gaussianity on distribution of the brightness temperature field, we introduced the 21 cm bispectrum as a method to probe a non-gaussianity in the brightness temperature field. We also investigate the property of 21 cm bispectrum and the difference between the 21 cm power spectrum and the bispectrum.

Finally, as the application of the 21 cm bispectrum, we performed the Fisher forecast for the EoR model parameters by using the 21 cm bispectrum. In particular, we estimate how we can put constraints on the EoR model parameters with MWA and LOFAR telescopes. We also compare the constraints obtained by the 21 cm power spectrum with the one obtained by the 21 cm bispectrum.

This Thesis is organized as follows. In Chapter 2, we briefly review the knowledge of the cosmology to understand structure formation in the Universe. In this chapter, we start from the Friedmann equations and summarize the evolution of the matter fluctuations based on the linear perturbation theory, nonlinear structure formation, the Press-Schechter mass function and the condition to form first luminous objects in a dark matter halo.

In Chapter 3, we briefly summarize the EoR model and introduce current constraints on the EoR. In Chapter 4, we summarize the fundamental physics related to the 21 cm line. Since various astrophysical processes affect the 21 cm line, we briefly introduce each process.

Our main results are presented in Chapter 5, 6 and 7. In Chapter 5, we introduce the one-point statistics for the 21 cm brightness temperature field and then, we discuss how useful these statistical values are to analyze 21 cm signal.

In Chapter 6, we suggest the 21 cm bispectrum as a method to probe the statistical nature of the 21 cm brightness temperature field. We investigate the scale dependence, redshift dependence of the 21 cm bispectrum and the components of the 21 cm bispectrum.

In Chapter 7, we apply the Fisher analysis to the EoR model parameters by using the 21 cm bispectrum and estimate the expected error of the parameters obtained by MWA and LOFAR observations.

Finally, we summarize the conclusion and future works in Chapter 8.

Chapter 2

Basic knowledge of cosmology

In this chapter, we first give a review of basic knowledge of cosmology which is required to understand this Thesis. First of all, we derive the Friedmann Universe based on the general theory of relativity (GR). Second, we give a description of the structure formation in the Universe based on the linear perturbation theory and introduce statistical values such as a two-point correlation function and the power spectrum to analyze the density fluctuations field. Finally, we briefly describe the basics of the nonlinear structure formation with a spherical collapse model, the Press-Schecther formalism and the Zel'dovich approximation. This chapter is based on [27, 84].

2.1 Friedmann Universe

A picture of the modern Universe relies on *the cosmological principle*. The cosmological principle is that the distribution of matter in the Universe is isotropic and homogeneous. This means that the Universe has no special point and direction. However, we know that there are stars, galaxies and galaxy clusters in the Universe. It is well-known that the Universe is inhomogeneous observationally at the scales less than $\sim 100h\mathrm{Mpc}^{-1}$. On the other hand, the distribution of matter in the Universe is almost all homogeneous and isotropic at larger scales than $\sim 100h\mathrm{Mpc}^{-1}$. We can derive the geometry of the Universe from the GR under homogeneous and isotropic distributions of matter with the Friedmann-Robertson-Walker(FRW) metric [eq.(2.1)].

$$ds^2 = g_{\mu\nu}dx^\mu dx^\nu = dt^2 - a^2(t)\left[\frac{dr^2}{1-kr^2} + r^2(d^2\theta^2 + \sin^2\theta d\phi^2)\right], \tag{2.1}$$

where $g_{\mu\nu}$ is the metric tensor. $a(t)$ denotes the scale factor which relates to redshift such as $1 + z = 1/a(t)$. (r, θ, ϕ) expresses comoving coordinate system. k is a curvature of the Universe. In the case of $k > (<)0$, the Universe is opened (closed) and the Universe is flat in the case of $k = 0$.

Next, we consider the time evolution of the scale factor $a(t)$. This describes the expansion history of the Universe. We can follow the evolution of the scale factor based on Einstein equation shown in eq.(2.2).

$$R_{\mu\nu} - \frac{1}{2}g_{\mu\nu}R + \Lambda g_{\mu\nu} = \frac{8\pi G}{c^4}T_{\mu\nu}, \tag{2.2}$$

where $R_{\mu\nu}$ is the Einstein Ricci tensor and R is the Ricci scalar. They are expressed by the FRW metric and its derivatives. Λ is the cosmological constant. $T_{\mu\nu}$ is the energy momentum tensor. Under the assumption of homogeneous and isotropic Universe, the energy momentum tensor can be described in the form of the perfect fluid such as

$$T_{\mu\nu} = (\rho + p)u_\mu u_\nu + p g_{\mu\nu}, \tag{2.3}$$

where u_μ is the four velocity of the fluid, ρ and p are the mass density and the pressure at the rest frame, respectively. Substituting this energy momentum tensor for eq.(2.2), we can get following equations.

$$\left(\frac{\dot{a}}{a}\right)^2 \equiv H^2(t) = \frac{8\pi G}{3c^2}\rho - \frac{kc^2}{a^2} + \frac{c^2\Lambda}{3} \tag{2.4}$$

$$\frac{\ddot{a}}{a} = -\frac{4\pi G}{3c^2}(\rho + 3p) + \frac{c^2\Lambda}{3} \tag{2.5}$$

Here, $H(t)$ is the *Hubble parameter* which is an expanding rate of the Universe. Eq.(2.4) represents the time evolution of the scale factor. This equation is called the *Friedmann equation*. On the other hand, Eq.(2.5) represents the spacial components. Combing with eq.(2.4), eq.(2.5) becomes

$$\dot{\rho} + 3\frac{\dot{a}}{a}(\rho + p) = 0. \tag{2.6}$$

These two equations (eqs.(2.4) and (2.6)) describe the time evolution of the scale factor and the entropy conservation in isotropic and homogeneous Universe, respectively.

2.2 Evolution of matter fluctuations

As far, we introduced the Friedmann equation which describes the isotropic and homogeneous Universe. At the early Universe, the homogeneity is almost satisfied and only slight inhomogeneity is present. However, no structure cannot be formed if the Universe would be perfect isotropic and homogeneous. We require slight anisotropies and inhomogeneities to form structures in the present Universe. These slight anisotropies and inhomogeneities are amplified through the gravitational instability. In this section, we consider the evolution of the matter fluctuations based on the linear perturbation theory.

2.2.1 Linear perturbation theory

Since the matter fluctuations behave as the perfect fluid, we can follow the time evolution of the density fluctuations by using three fluid equations. (i) The Euler equation which describes the motion of the fluid by relating with the velocity field $\mathbf{v}$, the pressure field p, the density field ρ and the gravitational potential ϕ. (ii) The continuum equation which represents the conservation law. (iii) The Poisson equation which describes how the gravitational potential is generated by the density field. These three equations are written by eq.(2.7)-eq.(2.8).

$$\frac{\partial \mathbf{v}}{\partial t} + (\mathbf{v}\cdot\nabla)\mathbf{v} = -\frac{\nabla p}{\rho} - \nabla\phi \quad : \text{Euler equation} \tag{2.7}$$

$$\frac{\partial \rho}{\partial t} + \nabla\cdot(\rho\mathbf{v}) = 0 \quad : \text{Continuum equation} \tag{2.8}$$

$$\Delta\phi = 4\pi G\rho \quad : \text{Poisson equation} \tag{2.9}$$

Note that these equations are described under the physical scale coordinate system. Therefore, we have to rewrite these equations in the form of comoving values to apply to the expanding Universe.

A physical scale $\mathbf{r}$ is related to comoving scale $\mathbf{x}$ with the scale factor such as $\mathbf{r} = a\mathbf{x}$. We define the comoving velocity field as $\mathbf{u} \equiv a\dot{\mathbf{x}}$. Then, the physical velocity can be written by

$$\mathbf{v} = \dot{\mathbf{r}} = \dot{a}\mathbf{x} + a\dot{\mathbf{x}} = H\mathbf{r} + \mathbf{u}. \tag{2.10}$$

Next we introduce the gravitational potential under the comoving coordinate system $\Phi \equiv \phi + a\ddot{a}|\mathbf{x}|^2/2$. We also introduce the density fluctuations $\delta(\mathbf{x},t)$ and the pressure fluctuations $\delta p(\mathbf{x},t)$ as follows:

$$\delta(\mathbf{x},t) = \frac{\rho(\mathbf{x},t) - \bar{\rho}(t)}{\bar{\rho}(t)} \tag{2.11}$$

$$\delta p(\mathbf{x},t) = p(\mathbf{x},t) - \bar{p}(t) \tag{2.12}$$

Here, $\bar{\rho}$ is the isotropic and homogeneous component of ρ, and $\bar{p}(t)$ is the component of p in the Friedmann Universe. With these fluctuations, fluid equations can be rewritten by

$$\frac{\partial \mathbf{u}}{\partial t} + H\mathbf{u} + \frac{1}{a}(\mathbf{u}\cdot\nabla)\mathbf{u} = -\frac{\nabla(\delta p)}{a\bar{\rho}(1+\delta)} - \frac{1}{a}\nabla\Phi \quad : \text{Euler equation} \tag{2.13}$$

$$\frac{\partial \delta}{\partial t} + \frac{1}{a}\nabla\cdot\big[(1+\delta)\mathbf{u}\big] = 0 \quad : \text{Continuum equation} \tag{2.14}$$

$$\Delta\Phi = 4\pi G a^2\bar{\rho}\delta \quad : \text{Poisson equation} \tag{2.15}$$

These three equations describe the evolution of the density fluctuations under the gravitational potential and govern the structure formation in the expanding Universe.

2.2.2 Jeans instability

In the case that each fluctuation δ, δp and $\mathbf{u}$ is too small, we can regard the terms higher than second order of these quantities as negligible. As the result, we can obtain the linearized Euler and continuum equations as follows:

$$\frac{\partial \mathbf{u}}{\partial t} + H\mathbf{u} + \frac{\nabla(\delta p)}{a\bar{\rho}} + \frac{1}{a}\nabla\Phi = 0 \tag{2.16}$$

$$\frac{\partial \delta}{\partial t} + \frac{1}{a}\nabla \cdot \mathbf{u} = 0. \tag{2.17}$$

Combined with eq.(2.15), we can get following equation

$$\frac{\partial^2 \delta}{\partial t^2} + 2H\frac{\partial \delta}{\partial t} - \left[4\pi G\bar{\rho}\delta + \frac{\Delta(\delta p)}{a^2\bar{\rho}}\right] = 0. \tag{2.18}$$

Here, we assume that the equation of state can be written in the form of $p = p(\rho, S)$, where S represents the entropy in the fluid. Under the linear approximation, the pressure perturbation can be written by

$$\delta p = \left(\frac{\partial p}{\partial \rho}\right)_S \bar{\rho}\delta + \left(\frac{\partial p}{\partial S}\right)_\rho \delta S. \tag{2.19}$$

The coefficient of the first term in eq.(2.19) corresponds to square of the sound speed of the fluid,

$$c_s^2 = \left(\frac{\partial p}{\partial \rho}\right)_S. \tag{2.20}$$

If we can ignore the entropy perturbation, the evolution equation of the density perturbation can be rewritten by

$$\frac{\partial^2 \delta}{\partial t^2} + 2H\frac{\partial \delta}{\partial t} - \left[4\pi G\bar{\rho}\delta + \frac{c_s^2\Delta\delta}{a^2}\right] = 0 \tag{2.21}$$

In the Fourier space, eq.(2.21) becomes

$$\frac{\partial^2 \tilde{\delta}}{\partial t^2} + 2H\frac{\partial \tilde{\delta}}{\partial t} - \left[4\pi G\bar{\rho} - \frac{c_s^2 k^2}{a^2}\right]\tilde{\delta} = 0. \tag{2.22}$$

Here $\tilde{\delta}$ is the matter fluctuation in the Fourier space. From this equation, we can see that each Fourier mode evolves independently and different Fourier modes are not mixed with each other. This is a typical property of the linear perturbation theory.

Eq.(2.22) can be regarded as an equation of motion for $\tilde{\delta}$. Then, we evaluate the behavior of the solution without solving this equation . The first term of eq.(2.22) represents an acceleration of $\tilde{\delta}$, the second term denotes the friction by the expanding Universe in proportion to the velocity of $\tilde{\delta}$. The third term expresses the potential power depending on $\tilde{\delta}$. Therefore, eq.(2.22) is equivalent to a one-dimensional equation of the motion in the potential $V(\tilde{\delta}) = -(4\pi G\bar{\rho} - \frac{c_s^2 k^2}{a^2})\tilde{\delta}/2$ with the friction force. If the $(4\pi G\bar{\rho} - \frac{c_s^2 k^2}{a^2})$ is negative, $\tilde{\delta}$ oscillates decreasingly and cannot grow. This phenomenon occurs if the sound speed is sufficiently large. Then, the density fluctuations cannot grow because the gravitational contraction is inhibited by the pressure. On the other hand, if the $(4\pi G\bar{\rho} - \frac{c_s^2 k^2}{a^2})$ is positive, the density fluctuations can grow because the gravitational contraction

overcomes the pressure. The wave number which distinguishes these situations is called the *Jeans wave number*. The Jeans wave number is represented by

$$k_J = \frac{a\sqrt{4\pi G\bar{\rho}}}{c_s}, \tag{2.23}$$

or, expressed in the form of the wavelength. This wavelength is called the *Jeans length* and written by

$$\lambda_J \equiv \frac{2\pi a}{k_J} = c_s\sqrt{\frac{\pi}{G\bar{\rho}}} \tag{2.24}$$

In the case that a wavelength of the density fluctuation is larger than the Jeans length, the density fluctuation can grow and begin the structure formation, whereas it cannot grow in the opposite case. We can define the *Jeans mass* by considering the mean mass density $\bar{\rho}$ which is included in a sphere with the Jeans radius. The Jeans mass can be represented by

$$M_J = \frac{4\pi\bar{\rho}}{3}\left(\frac{\lambda_J}{2}\right)^3 = \frac{\pi^{5/2}}{6}\frac{c_s^3}{\sqrt{G^3\bar{\rho}}} \tag{2.25}$$

The Jeans mass gives a criterion of mass above which the structure formation can start.

2.2.3 Growth of the density fluctuations by the gravitational instability

We here focus on the scales larger than the Jeans length and on the density fluctuations of non-relativistic matter. In this case, the evolution of the density fluctuations in the Fourier space is given by

$$\frac{\partial^2\tilde{\delta}}{\partial t^2} + 2H\frac{\partial\tilde{\delta}}{\partial t} - 4\pi G\bar{\rho}\tilde{\delta} = 0 \tag{2.26}$$

Eq.(2.26) has two independent solutions as follows:

$$D_+(t) \propto H(a)\int_0^a \frac{da}{a^3H^3} \tag{2.27}$$

$$D_-(t) \propto H(a) \tag{2.28}$$

The former mode expresses the growth mode and the latter is the decaying mode, respectively. We ignore the decaying mode because this mode cannot contribute to the structure formation in the Universe. Therefore, we only focus on the growing mode. We call this growth mode solution the *linear growth factor*. Hereafter we denote $D(a)$ instead of $D_+(a)$. The linear growth factor is described by

$$D(a) = \frac{5}{2}a\Omega_m\int_0^1 \frac{dx}{(\Omega_m/x + \Omega_\Lambda x^2 + 1 - \Omega_m - \Omega_\Lambda)^{3/2}} \tag{2.29}$$

Here, we choose a normalized parameter which satisfies $D \to 0$ when $a \to 0$. We can express the evolution of density fluctuations with the linear growth factor as follows:

$$\delta(\mathbf{x}, t) = D(t)\delta_0(\mathbf{x}), \tag{2.30}$$

where δ_0 is the present density fluctuations.

2.2.4 Statistical property of the density fluctuations

The fundamental observable value of the Universe is the density fluctuations. However, we cannot predict the values of the density fluctuations at each point theoretically although we can determine the density fluctuations at each point observationally. Instead of a prediction for the density fluctuations at each point, the cosmological model can predict the nature of the density fluctuations statistically. Therefore, we need a method to extract the statistical information from the observable values to compare with theory.

Here, we introduce a *two-point correlation function* at certain two points. The two-point correlation function connects the theoretical predictions with observations. The two-point correlation function is defined by

$$\langle \delta(\mathbf{x})\delta(\mathbf{x}^{'})\rangle \equiv \xi(\mathbf{x} - \mathbf{x}^{'}). \tag{2.31}$$

For the gaussian random field, the two-point correlation function can describe the statistical property of the field perfectly. In the Fourier space, the two point correlation function is expressed by

$$\langle \tilde{\delta}(\mathbf{k})\tilde{\delta}(\mathbf{k}^{'})\rangle = (2\pi)^3\delta_D(\mathbf{k} + \mathbf{k}^{'})P(k) \tag{2.32}$$

Here, we defined

$$P(k) = \int d^3x e^{-i\mathbf{k}\cdot\mathbf{x}}\xi(|\mathbf{x}|)$$

This $P(k)$ is called the *power spectrum*. There is a Fourier relation between the two-point correlation function and the power spectrum. Note that the power spectrum does not depend on directions under the isotropic Universe.

The power spectrum $P(k)$ is can be expressed by the transfer function $T(k, t)$, the linear growth factor $D(a)$ and the initial power spectrum $P_{ini}(k)$ as follows;

$$P(k, t) = \frac{T^2(k, t)D^2(t)}{D^2(t_{\rm ini})}P_{\rm ini}(k). \tag{2.33}$$

From eq.(2.33), we can see that this form shows that the power for each mode is in proportion to the initial power and independent on other modes. The initial power spectrum is predicted by inflation theories. Generally, they predict the initial power spectrum in the form of power law for wavenumber;

$$P_{\rm ini}(k) = Ak^n \tag{2.34}$$

A is an amplitude of the initial power spectrum. n_s is the spectral index. Most of inflation models predict $n_s \sim 1$. $n_s = 1$ case is called the *Harrison Zel$^{'}$dovich spectrum*.

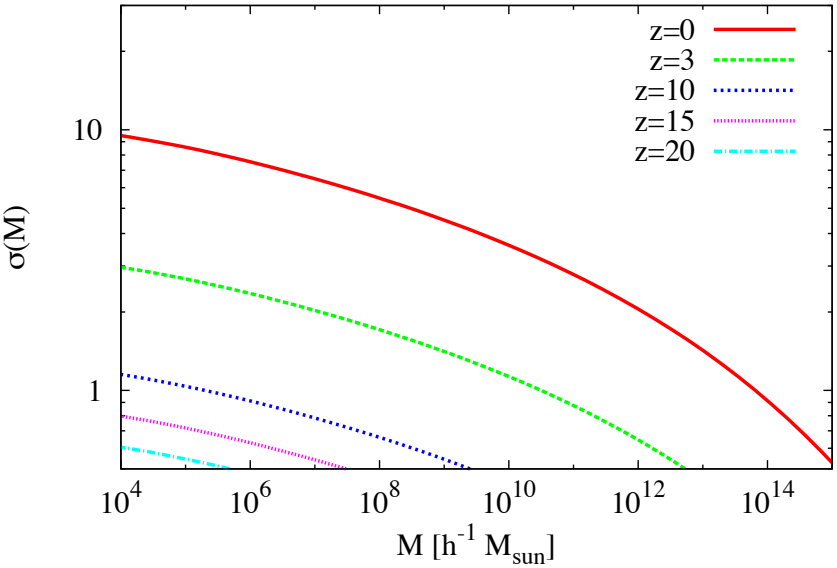

Figure 2.1: Variance of the density fluctuations as function of mass for various redshifts.

The transfer function $T(k,t)$ describes how the initial power spectrum of each mode evolves inside the Hubble scale.

As a next step, we focus on a normalization of the power spectrum. We use the variance of the density fluctuations averaged over a sphere with a radius $R = 8h^{-1}\mathrm{Mpc}^{-1}$ to determine a normalization factor of the power spectrum. The density fluctuations averaged over a sphere with a radius R are given by

$$\sigma^2(R) = \sigma^2(M) \equiv \left\langle \left(\frac{\delta M}{M} \right)^2 \right\rangle = \int \frac{k^2 dk}{2\pi^2} W^2(kR) P(k) \tag{2.35}$$

$W(kR)$ is a window function. $W(kR)$ can extract information on the scales $k \lesssim 1/R$. The top-hat type of the window function can be described by

$$W(kR) = \frac{3}{(kR)^3}[\sin(kR) - kR\cos(kR)] \tag{2.36}$$

We show the variance of the density fluctuations as function of the mass in Fig.2.1.

2.3 Nonlinear structure formation

So far, we see the structure formation based on the linear perturbation theory. However, we can use the linear perturbation theory only in the case of $\delta \ll 1$. For the density fluctuations with $\delta > 1$, we cannot use the linear perturbation theory. We call this regime the

nonlinear regime. An analytic evaluation of the nonlinear regime is more difficult than that of the linear regime. In this chapter, we introduce a method to treat the nonlinear regime such as the spherical collapse model, the Press-Schechter formalism and the Zel′dovich approximation.

2.3.1 Spherical collapse model

We here introduce a *spherical collapse model* as a simple model to describe the structure formation in the nonlinear regime. Let us consider spherical matter distribution around a certain point. In this situation, it is a simple one-dimension problem to study the evolution of matter by the gravitational force. The equation of the motion for the matter distributed inside a sphere with a radius R is written by

$$\frac{d^2R}{dt^2} = -\frac{GM}{R^2}, \tag{2.37}$$

where M is the mass inside a sphere. The solution of this equation is expressed with a parameter θ,

$$R = (GM)^{1/3}A^2(1-\cos\theta) \tag{2.38}$$

$$t = \frac{A^3}{\sqrt{GM}}(\theta - \sin\theta) \tag{2.39}$$

A is an integral constant. The mass density is $\rho = 3M/4\pi R^3$. The mean mass density $\bar{\rho}$ is given by $\bar{\rho} = 1/6\pi G t^2$ in the Einstein-de-Sitter. Then, the density fluctuation inside sphere becomes

$$\delta(t) = \frac{\rho}{\bar{\rho}} - 1 = \frac{9GMt^2}{2R^3} - 1 = \frac{9}{2}\frac{(\theta-\sin\theta)^2}{(1-\cos\theta)^3} - 1 \tag{2.40}$$

R reaches a maximum at $\theta = \pi$. At this point, R and t become

$$R_{turn} = 2(GM)^{1/3}A^2 \tag{2.41}$$

$$t_{turn} = \pi A^3. \tag{2.42}$$

At this point, the matter density fluctuations become δ_{turn}=$9\pi^2/16 - 1 \sim 4.55$. After R reaches a maximum, radius turns to decrease with time and it becomes 0 (the collapse point) at $t_{coll} = 2t_{turn} = 2\pi A^3$ ($\theta = 2\pi$). At the collapse point, mass density fluctuations become infinity. The duration from t_{turn} to t_{coll} is called the *free fall time*. The free fall time $t_{\rm ff}$ is given by

$$t_{\rm ff} = t_{coll} - t_{turn} = \pi A^3 = \frac{\pi}{2}\sqrt{\frac{R_{turn}^3}{2GM}} = \sqrt{\frac{3\pi}{32G\rho_{turn}}} \tag{2.43}$$

The free fall time gives a characteristic time scale that takes objects to collapse under the gravitational force.

If δ is sufficiently small, we should be able to describe the evolution of δ in the context of the linear perturbation theory even if δ is obtained by the spherical collapse model.

Applying the linear perturbation theory to the matter density fluctuations at $t = t_{turn}, t_{coll}$ with the spherical collapse model, we can obtain the fluctuations at $t = t_{turn}, t_{coll}$

$$\delta_L(t_{turn}) = \frac{3(6\pi)^{2/3}}{20} \sim 1.06 \tag{2.44}$$

$$\delta_L(t_{coll}) = \frac{3(12\pi)^{2/3}}{20} \sim 1.69. \tag{2.45}$$

The matter density becomes infinity at $\delta_L \sim 1.69$ which is evolved by the linear perturbation theory.

2.3.2 Virial equilibrium

In the previous section, we considered a spherical collapse model. In this model, the matter density diverge at a collapse point. However, this never happens actually. Instead of this, the collapsed objects begin to form at that point. Here, we introduce the virial theorem which can be realized under a system bound by the gravitational forces. According to the virial theorem, the potential energy U is related to the kinetic energy K in the form of $U + 2K = 0$ once virialized state is realized.

Within a context of the spherical collapse model, it is supposed that the virialized state is realized when the density fluctuations reach δ_{coll}. At the virialized state, it is known that the density fluctuation becomes $\delta_{coll} \sim 177$, and then objects begin to collapse. At high density regions, the collapsed objects can easily form. In such regions, the dark matter and galaxies are concentrated within a spherical region. This structure is called a halo.

We here introduce the *virial radius* r_{vir} and the *virial temperature* T_{vir} as values defined at the virialized state. At high z, these are written by [5],

$$r_{vir} = 0.784\left(\frac{M}{10^8 h^{-1} M_\odot}\right)^{1/3}\left[\frac{\Omega_m}{\Omega_m^z}\frac{\Delta_c}{18\pi^2}\right]^{-1/3} \times \left(\frac{1+z}{10}\right)^{-1} h^{-1}[\mathrm{kpc}]. \tag{2.46}$$

$$T_{vir} = 1.32 \times 10^4\left(\frac{\mu}{0.6}\right)\left(\frac{M}{10^8 h^{-1} M_\odot}\right)^{2/3} \times \left[\frac{\Omega_m}{\Omega_m^z}\frac{\Delta_c}{18\pi^2}\right]^{1/3}\left(\frac{1+z}{10}\right)[\mathrm{K}]. \tag{2.47}$$

Here, $\mathrm{M}_\odot$ is a solar mass and M is a collapsed mass of a halo at redshift z. Δ_c is given by $\Delta_c = 18\pi^2 + 82d - 39d^2$, $d = \Omega_m^z - 1$ at redshift z with $\Omega_m^z = \Omega_m(1+z)^3/(\Omega_m(1+z)^3 + \Omega_\Lambda)$.

2.3.3 Zel'dovich Approximation

We introduce the Zel'dovich approximation which gives the nonlinear evolution of fluctuations approximately. We start initial matter distribution which is considered to be homogeneous. If the initial Lagrangian coordinate of the particle is described by $\mathbf{q}$, then the Eulerian coordinate of the particle at t is given by

$$\mathbf{x} = \mathbf{q} + \mathbf{p}(\mathbf{q}, t), \tag{2.48}$$

where $\mathbf{p}(\mathbf{q}, t)$ is displace vector. Here, we consider mass density $\rho(\mathbf{x}, t)$ at time t and that at initial time t_i. Since the matter distribution is regarded to be homogeneous at initial time, matter density at initial time, $\bar{\rho}(t)$, is independent on time. Then, mass conservation law requires $\rho(\mathbf{x}, t)d^3x = \bar{\rho}(t)d^3q$. This leads

$$\delta(\mathbf{x}, t) = \frac{\rho(\mathbf{x}, t)}{\bar{\rho}(t)} - 1 \simeq= -\mathrm{tr}\left(\frac{\partial \mathbf{p}}{\partial \mathbf{q}}\right) = -\nabla_q \cdot \mathbf{p}. \tag{2.49}$$

Here, $\nabla_p = \partial/\partial\mathbf{q}$ is a gradient in the Lagrangian coordinate and $\delta(\mathbf{x}, t)$ is density fluctuation. If the density fluctuations are sufficiently small, this solution should consistent with that obtained by the linear perturbation theory. We determine $\mathbf{p}$ as it gives a growth solution obtained by the linear perturbation theory and extrapolate this $\mathbf{p}$ to nonlinear regime. Compared eq.(2.49) with eq.(2.30), we can determine $\mathbf{p}$ as follows:

$$\mathbf{p}(\mathbf{q}, t) = D(t)\nabla_q \phi_0(\mathbf{q}), \tag{2.50}$$

where $\phi_0(\mathbf{q})$ is the time independent potential in the Lagrangian coordinate and it satisfies with Laplace equation $\Delta_{\mathbf{q}}\phi_0(\mathbf{q}) = -\delta_0(\mathbf{q})$.

Finally, the motion of particle is given by

$$\mathbf{x} = \mathbf{q} + \mathbf{p}(\mathbf{q}, t) = \mathbf{q} + D(t)\nabla_q \phi_0(\mathbf{q}). \tag{2.51}$$

Although this equation holds while the density fluctuations are small, we extrapolate the motion described by this equation into nonlinear regime in the Zel'dovich approximation.

2.4 Press-Schechter formalism

So far, we introduced a structure formation model based on the linear perturbation theory and the Zel'dovich approximation. In this section, we estimate how many haloes form for a certain mass based on the Press-Schechter formalism[103]. In the Press-Schechter formalism, we combine the linear perturbation theory with the nonlinear theory.

One of the important points for the Press-Schechter theory is that initial density fluctuations are assumed to follow in the gaussian distribution. This assumption is reasonable because many inflation models predict this nature. In the gaussian type of distribution, the probability distribution function is given by

$$P(\delta)d\delta = \frac{1}{\sqrt{2\pi\sigma^2}} \exp\left(-\frac{\delta^2}{2\sigma^2}\right) \tag{2.52}$$

Here, $\sigma = \langle\delta^2\rangle$ is the variance of the density fluctuations. According to the linear perturbation theory, the time evolution of the density fluctuations is written by $\delta \propto \delta_{ini}D(t)$. Hence, the gaussian distribution keeps its shape with the time evolution.

Let us consider a sphere with a radius R and density $\bar{\rho}$. Inside this sphere, the mass M is given by $M = 4\pi R^3\bar{\rho}/3$. Next, we take the density fluctuations averaged inside the

sphere. The density fluctuations δ_M averaged by the mass scale M inside the sphere also follow in the gaussian distribution statistically,

$$P(\delta_M)d\delta_M = \frac{1}{\sqrt{2\pi\sigma^2(M)}}\exp\left(-\frac{\delta_M^2}{2\sigma^2(M)}\right) \tag{2.53}$$

We here focus on a fraction of a certain region with the density fluctuation δ_M and its time evolution. When δ_M exceeds a critical density δ_c, the fraction is thought to be incorporated by an object with a mass M in the Press-Schechter formalism. We adopt $\delta_c = 1.69$ which corresponds to the density fluctuation at the collapsed point in the spherical collapse model. Then, the ratio of the fraction which is incorporated by an object more than mass M is given by

$$P_{>\delta_c}(M) = \int_{\delta_c}^{\infty} P(\delta_M)d\delta_M = \frac{1}{2}\mathrm{erfc}\left[\frac{\delta_c}{2\sigma^2(M)}\right] \tag{2.54}$$

By using this ratio, we can calculate the fraction incorporated by objects whose mass is ranged from M to $M + dM$. In other word, we can estimate a total amount of mass which ranges from M to $M + dM$ in a unit of comoving volume. This total amount is given by $\bar{\rho}P_{>\delta_c}(M) - \bar{\rho}P_{>\delta_c}(M + dM)$. Meanwhile, the total amount of mass also can be described by $n(M)MdM$, where $n(M)dM$ is the number density of objects whose mass range is from M to $M + dM$. There are, however, two problems here. First, the objects which are once incorporated into a larger object are not taken in account. This is called cloud-in-cloud problem. Secondly, the initial density fluctuations which have negative value are never incorporated into objects. If the structure formation proceeds, we can take a limit of $\sigma_M \to \infty$ because of $\delta \propto D(t)$. In this limit, eq.(2.54) approaches 1/2. This means that a half of mass existing in the Universe never contributes to the structure formation. This does not reflect the actual structure formation. In the Press-Schechter prescription, we avoid this cloud-in-cloud problem simply by multiplying a factor of 2. As the result, we can describe the total amount mass ranged from M to $M + dM$ by relating the probability distribution function with the number density of objects;

$$n(M)MdM = 2\left|\bar{\rho}P_{>\delta_c}(M) - \bar{\rho}P_{>\delta_c}(M + dM)\right| = 2\bar{\rho}\left|\frac{dP_{>\delta_c}}{d\sigma(M)}\right|\left|\frac{d\sigma(M)}{dM}\right|dM \tag{2.55}$$

By substituting eq.(2.54) for eq.(2.55), we can obtain

$$n(M) = \sqrt{\frac{2}{\pi}}\frac{\bar{\rho}}{M^2}\left|\frac{d\ln\sigma(M)}{d\ln M}\right|\frac{\delta_c}{\sigma(M)}\exp\left(-\frac{\delta_c^2}{2\sigma^2(M)}\right) \tag{2.56}$$

This mass number density is called *the Press-Schechter mass function*. In Fig.2.2, we plot the Press-Schechter mass function. Note that a factor of 2 is justified by the excursion set theory based on random walk model[12, 72].

2.5 Extended Press-Schechter formalism

In this section, we present the excursion set formalism which is also called the extended Press-Schechter(EPS) formalism[72]. The EPS formalism naturally explains a factor 2 introduced to solve cloud-in-cloud problem in the the Press-Schecther formalism.

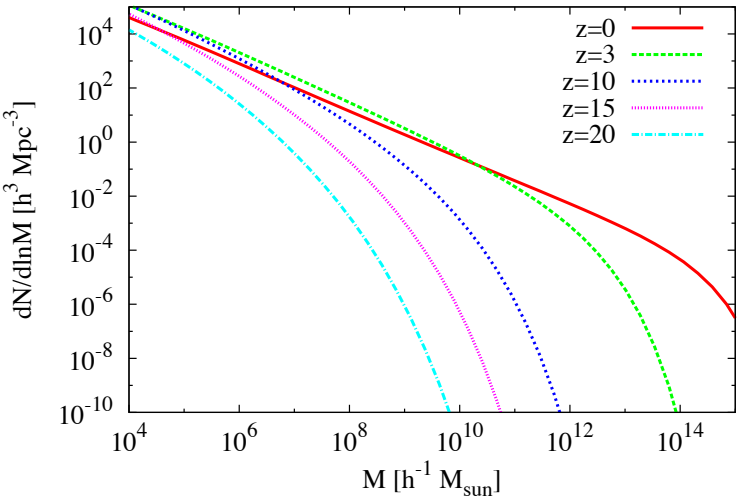

Figure 2.2: Press-Schechter mass function as a function of halo mass M for various redshifts. Since halos with smaller mass are easily formed, the number density of smaller mass halos is larger.

In the EPS formalism, we adopt $S \equiv \sigma^2(M)$ as mass variable. For the ΛCDM cosmology, S is a monotonically declining function of halo mass as shown in Fig.2.1, so that there is a clear one-to-one relation between S and M. First, we take density field $\delta(\mathbf{x})$. For each value of the filtering mass M, we consider density field $\delta(M, \mathbf{x})$ smoothed by scale M. This smoothed density field is also expressed by $\delta_S(\mathbf{x})$. The smoothed density field with sharp k-space filter is expressed by

$$\delta_S(\mathbf{x}) = \int d^3\mathbf{k}\tilde{W}_k(\mathbf{k}R)\delta_\mathbf{k}e^{i\mathbf{k}\cdot\mathbf{x}} = \int_{k<k_c} d^3\mathbf{k}\delta_\mathbf{k}e^{i\mathbf{k}\cdot\mathbf{x}} \tag{2.57}$$

where $\tilde{W}$ is a window function, $\delta_\mathbf{k}$ are Fourier modes of $\delta(\mathbf{x})$ and $k_c = 1/R$ is the size of the top-hat in k-space.

If we have $M \to \infty$, then $S \to 0$. Hence, each trajectory starts at $(S, \delta_S) = (0, 0)$. For sharp k-space smoothing filter, the trajectories wonder Markov random walk because changing S adds new and independent modes. We show a schematic representation of random walk in Fig.2.3.

We consider a given mass scale M_1, corresponding to S_1 as indicated by vertical solid line. According to the Press-Schechter(PS) ansatz, the mass elements whose trajectories are $\delta_S > \delta_c$ at S_1 reside in dark mater haloes with $M > M_1$. This means that neither trajectories A or B are in halo with $M > M_1$. However, according to the PS ansatz, mass element associated with trajectory B should be incorporated in halo with $M > M_3 > M_1$ because $\delta_S > \delta_c$ is satisfied over the interval $S_2 < S < S_3$. Clearly the PS ansatz is not self-consistent. This problem happens because it fails to account for the mass elements with trajectories such as trajectory B. In order to correct this problem, we consider the trajectory B' from (S_2, δ_c) to (S_1, Q_2). The trajectory B' is obtained by mirroring B for

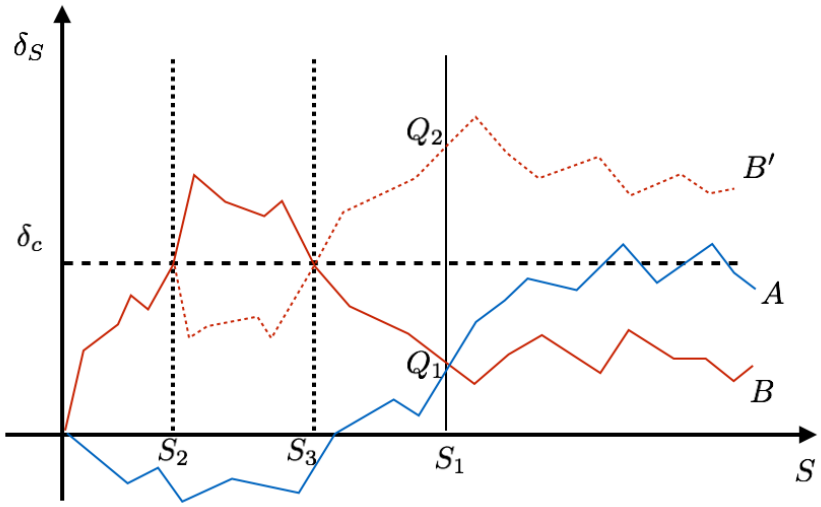

Figure 2.3: A schematic representation of random walk trajectories in (S, δ_s) space. Three trajectories correspond to three different mass elements in a Gaussian random field. The horizontal dashed line indicates the critical density for spherical collapse, $\delta_s = \delta_c$. Note that B' is obtained by mirroring trajectory B in the line $\delta_S = \delta_c$ for $S \geq S_2$.

$S \geq S_2$ in $\delta_S = \delta_c$. The fraction of mass in halos with $M \geq M_1$ is therefore given by twice as the fraction of trajectories crossing S_1 at $\delta_S > \delta_c$. This gives a natural explanation for the factor 2 in the original PS formalism.

Now, we study the fraction of trajectories that are above the threshold of fluctuation δ_c at some mass scale M_1 but are below this threshold for all mass scales larger than $M(S < S_1)$. This is equivalent to identifying the fraction of trajectories which have first upcrossing of $\delta_S = \delta_c$ at $S > S_1$ like trajectory A in Fig.2.3. In the Press-Schechter prescription, we associate these trajectories with the mass elements incorporated into mass $M < M_1$. Clearly, such trajectories have to satisfy with $(\delta_S(S_1) < \delta_c)$. These include trajectories such as B, which has the first upcrossing of the barrier at $S < S_1$ and we have to exclude these trajectories. In order to do this, we once again use mirror symmetry of B. The trajectories B and B' have equal probabilities. Indeed, all trajectories that pass through (S_1, Q_1) having $\delta_S > \delta_c$ for some $S < S_1$ have a mirror trajectory that passes thorough $(S, \delta_S) = (S_1, Q_2)$, where $Q_2 = Q_1 + 2(\delta_c - Q_1) = 2\delta_c - Q_1$. Thus, the fraction of trajectory with a first upcrossing at $S > S_1$ is simply given by

$$\begin{aligned} F(> S_1) &= \int_{-\infty}^{\delta_c} [P(\delta_S, S_1) - P(2\delta_c - \delta_S, S_1)] d\delta_S \\ &= \int_{-\infty}^{\delta_c} \frac{1}{\sqrt{2\pi}S} \left[\exp\left(-\frac{\delta_S^2}{2S}\right) - \exp\left(-\frac{(2\delta_c - \delta_S)^2}{2S}\right) \right] d\delta_S, \end{aligned} \tag{2.58}$$

where we have used that density fluctuations obey gaussian random field. As discussed above, the fraction given by eq.(2.58) is equal to the fraction $F(< M_1)$, of mass elements incorporated into halos with $M < M_1$. Each mass element in the Universe is expected to be in collapsed objects or not. Consequently, $F(> M) = 1 - F(< M)$. With this fact, we

can obtain the halo mass function as follows:

$$n(M,t)MdM = \bar{\rho}\frac{\partial F(>M)}{\partial M}dM = \bar{\rho}f_{FU}(S,\delta_c)\left|\frac{dS}{dM}\right|dM, \tag{2.59}$$

where

$$f_{FU}(S,\delta_c)dS = \frac{\partial F(>M)}{\partial S}dS = \frac{1}{\sqrt{2\pi}}\frac{\delta_c}{S^{3/2}}\exp\left[-\frac{\delta_c^2}{2S}\right]dS \tag{2.60}$$

is the fraction of trajectories that have their first upcrossing through the threshold in the interval $(S, S+dS)$. Simply, substituting eq.(2.60) into eq.(2.59) yields the PS mass function without having a factor of 2. The cumulative mass fraction in halos above some mass M is given by integrating eq.(2.60) from S=0,

$$P(>M,t) = P(<S,Q) = \mathrm{erfc}\left[\frac{\delta_c(t)}{\sqrt{2}\sigma(M)}\right]. \tag{2.61}$$

Other advantage of the excursion set approach is that it allows us to examine how halos relate to one another and evolve over time. We take a spherical region of mass M_2 at t_2, corresponding to a mass variance $S_2 = \sigma^2(M_2)$, with linear overdensity $\delta_2 \equiv \delta_c(t_2) = \delta_c/D(t_2)$. We now are interested in the fraction of M_2 that was in collapsed objects of a certain mass at an earlier time $t_1(t_1 < t_2)$. In this case, we can adopt the excursion set approach. We calculate the probability for a random walk originating at $(S,\delta_S) = (S_2,\delta_2)$ to execute a first upcrossing of the barrier $\delta_S = \delta_1 \equiv \delta_c(t_1)$ at $S = S_1$, corresponding to mass scale M_1. These trajectories represent that haloes at t_1 in the mass range$(M_1, M_1 + dM_1)$ have merged to form larger haloes M_2 at $t_2(> t_1)$. This is exactly the same problem as before except for a translation of the origin in the (S,δ_S) plane. Hence the probability we want is given by

$$f_{FU}(S_1,\delta_1|S_2,\delta_2)dS_1 = \frac{1}{\sqrt{2\pi}}\frac{\delta_1-\delta_2}{(S_1-S_2)^{3/2}}\exp\left[-\frac{(\delta_1-\delta_2)^2}{2(S_1-S_2)}\right]dS_1, \tag{2.62}$$

which follows form eq.(2.61) upon replacing δ_c by $\delta_1 - \delta_2$ and S by $S_1 - S_2$. This yields the cumulative mass fraction which represents collapsed fraction ranged from M_1 to M_2

$$P(M_2 > M_1, t_1, t_2) = \mathrm{erfc}\left[\frac{(\delta_c(t_1)-\delta_c(t_2))}{\sqrt{2}[\sigma(M_1)-\sigma(M_2)]}\right]. \tag{2.63}$$

Later, we use this formalism to introduce an analytic model for the EoR.

2.6 Baryonic object formation inside a dark matter halo

In previous sections, we show that the Press-Schechter mass function gives the number density of halos for a certain mass. Once objects realize virial equilibrium and make a dark matter halo, baryonic objects such as star and galaxy begin to form inside the dark matter halo. In this section, we investigate a condition for the formation of the baryonic objects inside a dark matter. We focus on a cooling process of the gas inside the dark matter halo. If the baryonic gas remains hot, the radiative pressure prevents the gas from contracting

by the gravitational force, and then no baryonic objects form. Thus, we need to consider the cooling process of the gas to relieve the radiation energy to realize formation of the baryonic objects.

2.6.1 Cooling of gas and the gravitational collapse

One of the important things for formation of the baryonic inside a halo is the gravitational collapse of the gas. Since the gravitational force is in proportion to inverse square of a radius, the gravitational force becomes larger as the gravitational contraction proceeds. However, the radiative pressure by the gas itself prevents the gas from contracting by the gravitational force. Consequently, we need to consider balance between the gravitational force and the radiative pressure.

Let us consider the gas cloud which has mass M and a radius R. The potential energy of the gas E_G is expressed by

$$E_G = -a\frac{GM^2}{R} \tag{2.64}$$

Here, a is a coefficient with a factor of 1, which is determined by the distribution of the gas. Meanwhile, the energy of the pressure E_p is written by

$$E_P = bR^3\bar{P} \tag{2.65}$$

$\bar{P}$ is the mean pressure and b is a coefficient with a factor of 1 determined by the shape of the gas. The variation of the potential energy due to the contraction of the gas is re-written by

$$\Delta E_G \propto R^{-1} \propto \bar{\rho}^{1/3} \tag{2.66}$$

$\bar{\rho}$ is the mean density.

In the case that the gas contracts adiabatically, the pressure P is in proportion to the mass density such as $P \propto \rho^\gamma$ with an adiabatic index γ. Therefore, the variation of the pressure energy is given by

$$\Delta E_P \propto R^3\bar{\rho}^\gamma \propto \bar{\rho}^{\gamma-1} \tag{2.67}$$

If we consider a monoatomic molecule or ionized gas, γ is given by 5/3. This leads to $\Delta E_P/\Delta E_G \propto \bar{\rho}^{1/3} > 1$. Thus, the variation of the pressure energy is larger than that of the potential energy, and then the gravitational contraction is prevented by the gas pressure because a gradient of the pressure exceeds the gravitational force immediately. Consequently, in order to form the baryonic objects, the gas has to be cooled efficiently to suppress the pressure.

2.6.2 Process of the gas cooling

An atomic excitation, the free-free emission and other radiation are considered as radiative cooling process. The radiation due to physical interaction among particles removes the energy from the gas and the gas can be cooled. For example, the gas emits photon according to an excitation which is caused by collision between two particles constituting of the gas. At this case, the cooling rate is in proportion to the square of the number density of the

gas n^2 because of two-body reaction. Then, the cooling rate $|\dot{E}_{\rm cool}|$ per unit volume per unit time can be expressed by

$$\left|\dot{E}_{\rm cool}\right| = n^2\Lambda(T) \tag{2.68}$$

Here, $\Lambda(T)$ is called the cooling function which is determined by quantum mechanical process.

Let us consider a time scale that the thermal energy $E_k = 3nk_BT/2$ is lost due to the radiative cooling. This time scale is called *the cooling time* and given by

$$t_{\rm cool} = \frac{E_k}{\left|\dot{E}_{\rm cool}\right|} = \frac{3}{2}\frac{k_{\rm B}T}{n\Lambda(T)} \tag{2.69}$$

The condition whether the objects form or not is determined by the balance between the free fall time and the cooling time as follows.

○ $t_{\rm ff} > t_{\rm cool}$

In the case that the free fall time is longer than the cooling time, the pressure of the gas decreases first. Then, it is possible to occur the gravitational contraction by overcoming the gas pressure. Therefore, the gas cloud is divided and star formation proceeds.

○ $t_{\rm ff} < t_{\rm cool}$

On the other hand, if the cooling time is longer than the free fall time, the cooling process is not efficient. As the result, the gravitational contraction is prevented by the pressure gradient of the gas because the gas pressure is higher than the gravitational force. Therefore, star formation does not proceed in a halo.

Chapter 3

From the Dark Ages to the EoR

In previous section, we briefly introduced the structure formation in the Universe based on ΛCDM model. After a dark matter halo begins to form, formation of first stars starts inside a dark matter halo. As the result of this, first luminous objects play an important role on thermal history of the IGM. We call this epoch the Cosmic Dawn ($z \sim 30$). As the structure formation in the Universe proceeds, the IGM is ionized by ionizing photons emitted by star-forming galaxies and the EoR begins in the Universe ($z \sim 15$). In this chapter, we first introduce formation and evolution of the first luminous objects. Next, we summarize the EoR from both observational and theoretical aspects.

3.1 First luminous objects

3.1.1 First stars

After dark matter halos formed, first stars begin to form inside a dark matter halo. The mass corresponding to the virial temperature $T_{\rm vir} \sim 10^4$[K] (Atomic cooling becomes effective above this temperature) is $10^8 M_\odot$. Below $T_{\rm vir} \sim 10^4$[K], atomic transition is not effective because collisions among hydrogen atoms do not carry sufficient energy to excite the atoms, and then hydrogen atoms emit no radiation via de-excite. Since the first gas cloud has a virial temperature $T_{\rm vir} \lesssim 10^4$[K], we require alternative coolant, which can work at low temperature, for cooling and fragmentation of the gas. Hydrogen molecules can work as coolant to satisfy this requirement. As shown in Fig.3.1, molecular cooling becomes effective at $M \sim 10^6 M_\odot$ with 3σ fluctuations at $z \sim 25 - 30$. Thus, the mass of host halo for first stars is expected to be $M \sim 10^6 M_\odot$.

Hydrogen molecules can form through rare chemical reactions in which free electrons act as catalysts as follows:

$$\mathrm{H} + e^- \rightarrow \mathrm{H}^- + \gamma \tag{3.1}$$

$$\mathrm{H}^- + \mathrm{H} \rightarrow \mathrm{H}_2 + \mathrm{e}^-. \tag{3.2}$$

After the cosmological recombination, H_2 abundance in the Universe is negligible. However, there are sufficient free electrons to catalyze H_2 inside the first gas clouds. Consequently, the minimum temperature achievable by H_2 cooling is ~ 200 [K] because the energy spacing

of the two rotational levels of molecule is ~ 512[K](the limit is somewhat smaller than that nominal value because of the high-velocity tail of the Maxwell-Boltzmann distribution). At this temperature, the number density of hydrogen gas is $n_H \sim 10^4 cm^{-3}$.

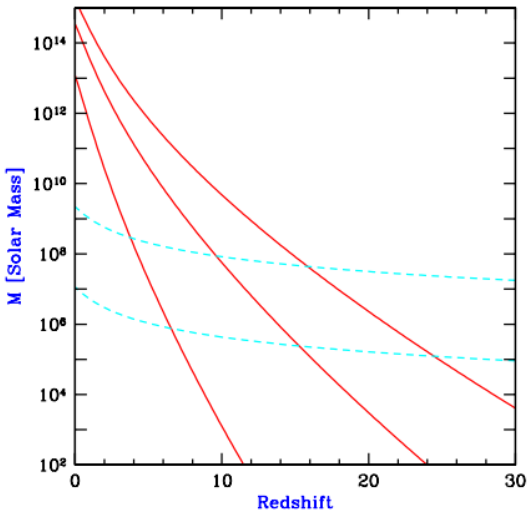

Figure 3.1: This figure shows characteristic properties of collapsed halo mass. The solid lines show mass corresponding to $1\sigma, 2\sigma, 3\sigma$ fluctuations (from left to right) and the dashed lines show mass which corresponds to minimum virial temperature required for efficient cooling, atomic cooling(top curve) and molecular cooling(bottom curve). Molecular cooling becomes effective for $M \sim 10^6 M_\odot$with 3σ fluctuation at $z \sim 24$. Above this mass scale, first stars begin to form via molecular cooling. This figure is taken from [5].

Further collapse requires enough large mass for the gas cloud to overcome gas pressure. In other words, the clump mass beyond the local Jeans mass is required to collapse. At $T \sim 200$K (or $\mathrm{n_H} \sim 10^4 \mathrm{cm}^{-3}$), the local Jeans mass is

$$M_J \sim 700 \left(\frac{T}{200\mathrm{K}}\right)^{3/2} \left(\frac{\mathrm{n_H}}{10^4 \mathrm{cm}^{-3}}\right)^{-1/2} M_\odot. \tag{3.3}$$

Inside core of this gas cloud, protostar begins to form with $M \sim 10^{-2} M_\odot$ and gets mass from the gas cloud around the core. As the result of accumulation of mass, the primordial star forms. We refer this metal-free primordial star which is formed by hydrogen atoms as *Population III (PopIII)*, whereas we call star with low metallicity *Population II (PopII)*. In Fig.3.2, we show evolution of gas distribution around protostar.

We next consider accretion of the gas onto protostar as process to get mass. The initial mass of protostar is similar for the primordial and present stars. However, accretion process which determines final stellar mass is expected to be rather different. The accretion rate is described as

$$\frac{dM}{dt} = \phi \frac{M}{t_{\mathrm{ff}}}, \tag{3.4}$$

where ϕ is dimensionless parameter which depends on the properties of medium and is

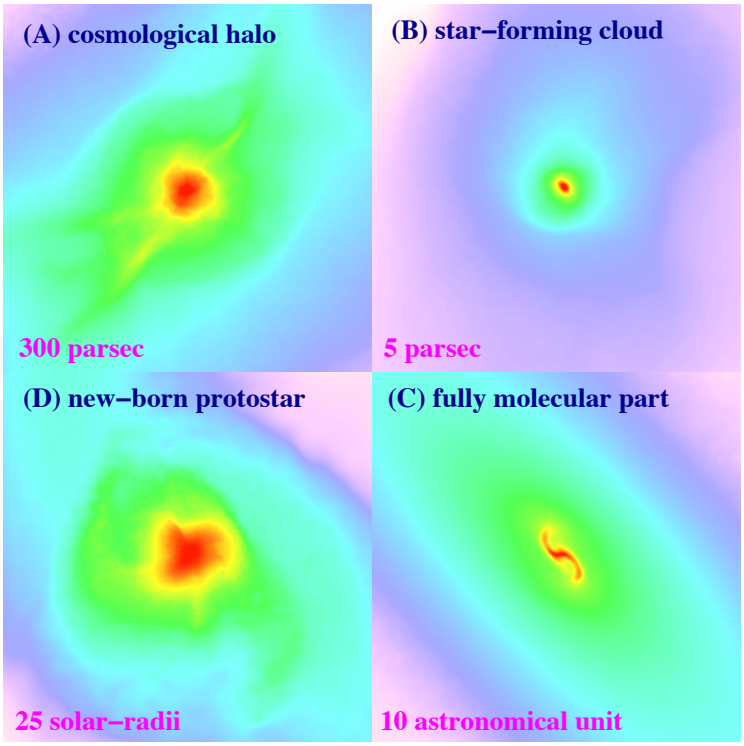

Figure 3.2: Projected gas distribution around protostar from a numerical simulation. (A) gas distribution around the cosmological halo. (B) star-forming cloud. (C) the central part of fully molecular core. (D) the final protostar. This figure is taken from [143].

expected to be $\phi \sim 1$. M is mass of the protostar. For self-gravitating clump, mass can approximate $M \sim M_J \sim c_s^3/\sqrt{G^3\rho}$. Thus, the accretion rate can be expressed by

$$\frac{dM}{dt} \sim \frac{c_s^3}{G} \propto T^{3/2}. \tag{3.5}$$

In a present-day star formation, heavy metal elements cool the gas to temperature as low as $T \sim 10$[K], whereas the primordial gas is cooled as low as $T \sim 200 - 300$[K] via hydrogen molecular cooling. This indicates that the accretion rate of the primordial gas is two orders of magnitude higher than that of present-day gas and the first stars can be much more massive than present-day stars. If we can ignore radiative feedback, first stars are expected to be $M \sim 10^2 - 10^3 M_\odot$ by accumulation of mass from the gas cloud. However, we expect that radiative feedback from protostar affects evolution of accretion. Thus, we need to take radiative feedback into account to estimate final mass of first stars. One of the examples of radiative feedback is photodissociation of H_2. As protostar heats up, it produces UV radiation which photodissociates H_2. As the result of photodissociation of H_2, cooling turns off and this leads to increases of radiative pressure. Thus, accretion rate decreases and protostar cannot get much mass from the gas cloud. Other radiative feedback is photoevaporation of the accretion disk. Ionizing photons emitted by protostar heat the disk around protostar, and then the gas is evaporated from disk. Thus, the accretion of the gas stops and protostar cannot accumulate mass. Recent studies show that final mass of first star varies from $10M_\odot$ to $10^3 M_\odot$ according depending on the properties of radiative feedback (such as different gas accretion rate and different protostellar evolution) and host

halo mass [61, 58].

So far, we have described formation of first stars starting from initial condition that gas is nearly neutral. This initial condition is of course proper for first star formation in a halo. But this initial condition is changed after first stars formed. Since first stars produce a large amount of ionizing photons, HII regions are generated around and within host dark matter halos. At this HII regions, ionized gas would collapse and first stars begin to form. As well as ionizing photon by first stars, powerful blast waves generated by explosion of stars would ionize nearby the gas. This initial condition starting from ionized gas results in different scenario for formation of first stars. These first stars starting from ionized gas are referred as *Population III.2*, whereas classical population III stars are referred as Population III.1. Because the initial gas in PopIII.2 is highly ionized and high temperature, large fraction of H_2 and HD gas can contribute to cooling process. HD cooling can cool gas temperature lower than H_2 cooling since J=1→0 energy transition in HD corresponds to temperature of ~ 130[K] which is about 4 times smaller than that of H_2. Therefore, mass of PopIII.2 stars are likely to be smaller than that of PopIII.1 (recall $M_J \propto T^{2/3}$).

3.1.2 The end states of PopIII stars

In previous subsection, we considered formation and evolution of first stars. In this subsection, we consider end state of PopIII stars. It is important to consider the end state of PopIII stars because objects formed after death of PopIII stars affect environment in the Universe. The expected fate of PopIII stars are expected to be determined by their stellar mass. Here, we list the fate of PopIII stars below.

- $M < 8 - 10M_\odot$; stars end their lives as white dwarfs, just as present-day low-mass stars do. Although they can produce light elements during their asymptotic giant branch phases, they do it with much longer timescales that the $<$ 1Gyr Hubble time at $z > 6$. Thus, their fates are unimportant to understand history of the early Universe.

- $M \sim 10{-}40M_\odot$; stars undergo Type II supernovae with low metallicity and they leave neutron star behind supernovae. These supernovae are responsible for the enrichment of heavy elements in the Universe during the Cosmic Dawn.

- $M \sim 40 - 100M_\odot$; blackholes forms after stars directly collapse without producing supernova and hence without enrichment of metals around blackholes.

- $M \sim 100 - 140M_\odot$; the enormous core following helium burning heats up rapidly, leading to the production of electron-positron pairs as a result of collisions between energetic gamma-ray photons and atomic nuclei. This production of electron-positron pairs reduces thermal pressure inside star's core because a part of energy is used to generate rest mass of the pairs. As the result, the star can contract due to low gas pressure. The core is compressed and heated up due to contraction of the star, thereby increasing energy absorbed by electron-positron pair creation. This instability creates mass-ejecting pulsations with supernova. The entire hydrogen envelope of the star is ejected, relieving the instability and allowing the reminder of stellar evolution to proceed as for a low-mass star, and the iron core eventually collapses to blackhole.

- $M \sim 140 - 260 M_{\odot}$; stars are likely to explode as pair-instability supernovae. This pair-instability is described in the case of $100 - 140 M_{\odot}$. Since the pressure drops off due to energy investment into rest mass energy of electron-positron pairs, star collapses partially and then explosion blows up the star without leaving remnant. The energy of pair-instability supernova can reach around 10^{53} ergs which is two order of magnitude larger than kinetic energy of typical supernova. Further, the light curves of pair-instability supernova is quite different from typical supernova. It is expected to be highly extended, with peak luminosity at around one year after occurring.

- $M > 260 M_{\odot}$; the helium cores directly collapse to blackholes. Above this mass scale, PopIII stars do not enrich metallicity around stars because stars themselves are swallowed up into the blackholes.

3.1.3 Gamma-ray bursts

Gamma-ray bursts(GRBs) are one of the bright flushes with extremely energetic explosion that is observed in distant galaxies(some GRBs are discovered at $z > 9$). One of properties of GRBs is afterglow. Initially GRBs are brightest at short wavelengths and fade away at longer wavelength, starting in X-ray band and shifting to UV band , optical band and finally IR and radio band. We notice that some long duration GRBs are accompanied by core-collapse supernova. This indicates that long duration GRBs are associated with death of massive stars. Although it is unknown whether PopIII stars produce long duration GRBs, if they can do, the GRBs might be detectable and can be used as probe of cosmic gas at high redshift.

3.2 Epoch of Reionization

The observation of the CMB indicates that neutral hydrogen atoms formed after recombination and the Universe was full of the neutral hydrogen atoms. However, observations of early galaxies, QSO spectra and gamma-ray bursts as well as the CMB indicate transition of the atomic state in the Universe. Neutral hydrogen atom is back to its constituent protons and electrons by ionizing photons from galaxies. This process is know as *reionization*. In this section, first of all, we introduce current observational constraint on the EoR. Next, we discuss physics of the EoR. In particular, we focus on formation and evolution of HII regions (or ionized bubbles) during the EoR. This section is based on [46]

3.2.1 Observational constraint on the EoR

Thanks to improvement of instruments, we can impose constraint on the EoR model from observations. In this section, we briefly summarize such current constraints.

Gunn-Peterson trough

We first show constraint on the IGM at late stage of the EoR with observation of QSO spectra. The QSO spectra is a measurement to probe the IGM and it is sensitive to neutral

hydrogen column density. The UV lines which have shorter wavelength than that of Lyα photon(=1216Å) in the rest frame are absorbed by neutral hydrogen atom. The lines bluewards of Lyα emission line are not seen in the spectra of QSO and produce absorption trough known as Gunn-Peterson trough. This trough appears in bluewards of Lyα emission line in the spectra of distant QSO.

The Lyα optical depth, which expresses the strength of absorption (see chapter 4.3), is given by

$$\tau_\alpha = 4.9 \times 10^5 \left(\frac{\Omega_m h^2}{0.13}\right)^{-1/2} \left(\frac{\Omega_b h^2}{0.02}\right) \left(\frac{1+z}{7}\right)^{3/2} \left(\frac{n_{\rm HI}}{n_{\rm H}}\right). \tag{3.6}$$

Since the transmission of photons is expressed by $e^{-\tau_\alpha}$, the Lyα features are shown with mild absorption if $\tau_\alpha \lesssim 1$. In order to satisfy this condition, the number density of neutral hydrogen atoms is required in order of 10^{-4}. Thus, the fact that we can observe the Lyα emission line means that the Universe is highly ionized and remaining neutral hydrogen atoms are sufficiently small. We show the spectra of high redshift QSO in Figs.3.3 and 3.4. From the observation of spectra of high redshift QSO, we can know the epoch when cosmological reionization finishes.

LAE galaxy

Next, we introduce another observation to constrain the EoR based on Lyα emitter galaxies(LAEs). The LAEs are young, star-forming galaxies which emit strong Lyα photons. One of the weak points of method to observe QSO spectra for constraint of the EoR history is that the transmission of Lyα photons is easily saturated because the optical depth of Lyα photon is too sensitive to column density of neutral hydrogen atoms. Thus, even if small amount of neutral hydrogen atoms exists, we cannot observe Lyα emission line. This means that we cannot apply the method based on observation of QSO spectra to higher redshift where fraction of neutral hydrogen atoms is higher than $\sim 10^{-4}$. On the other hand, the method to observe luminosity function(LF) of LAEs is not limited by fraction of neutral hydrogen atoms. Since the amplitude of luminosity function of LAEs depends on neutral hydrogen fraction, we can constrain neutral hydrogen fraction by comparing observed Lyα LF with simulation results[82]. We can also constrain that by comparing observed Lyα transmission relating to LF density with theoretical studies[71]. However, the method based on LF of LAEs suffers from substantial atmospheric absorption and strong night sky lines in the IR bands. Furthermore, it is also challenging problem to find sample of high redshift galaxies. However, this method can provide us with information on state of the IGM higher redshift than that obtained by QSO spectra. We show the Lyα LF and constraint on fraction of neutral hydrogen atoms obtained by the Lyα luminosity function in Fig.3.5.

CMB polarization

The CMB polarization power spectrum provides important information on the EoR independent on QSO spectra and LAEs observations. If the CMB photons are scattered later due to free electrons origin in reionization(Thomson scattering) and incident radiation has a quadrupole moment, large scale E-mode pattern of linear polarization emerges on CMB photons. This large scale E-mode pattern is not caused on the last scattering surface. In

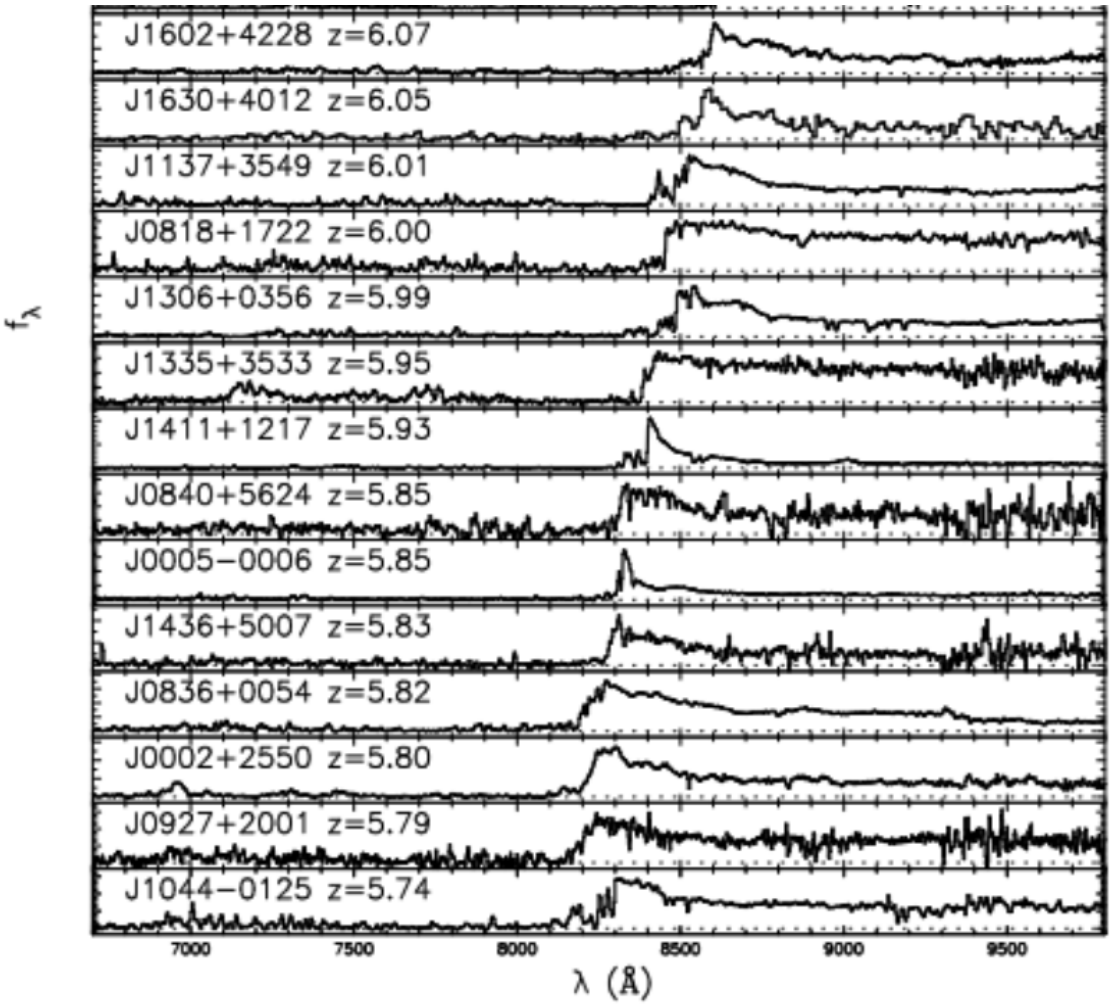

Figure 3.3: Spectra for high redshift SDSS quasars at z=5.74-6.07. Clearly, we can see the Gunn-Peterson trough bluewards of the Lyα emission line at high redshift. This indicates that the Universe is highly neutral. On the other hand, at lower redshift, we can observe absorption lines bluewards of the Lyα line with less absorption since the amount of neutral hydrogen atoms is small. This figure is taken from[34].

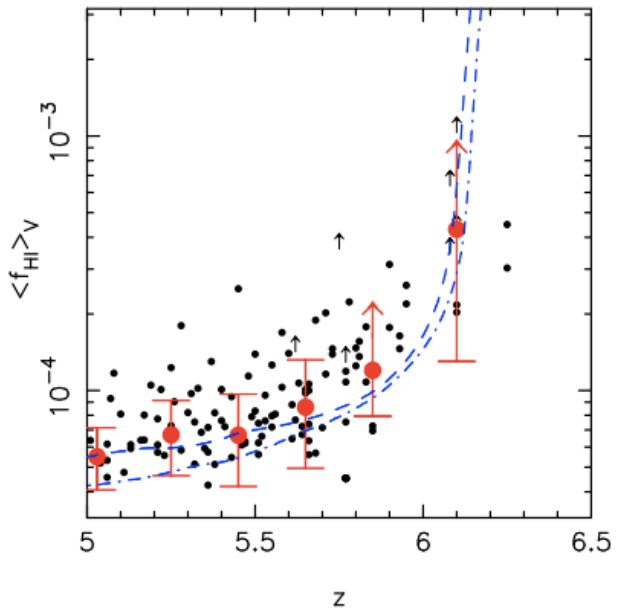

Figure 3.4: This figure shows constraint on the fraction of neutral hydrogen atoms as function of redshift obtained by QSO spectra. This figure is taken from[34].

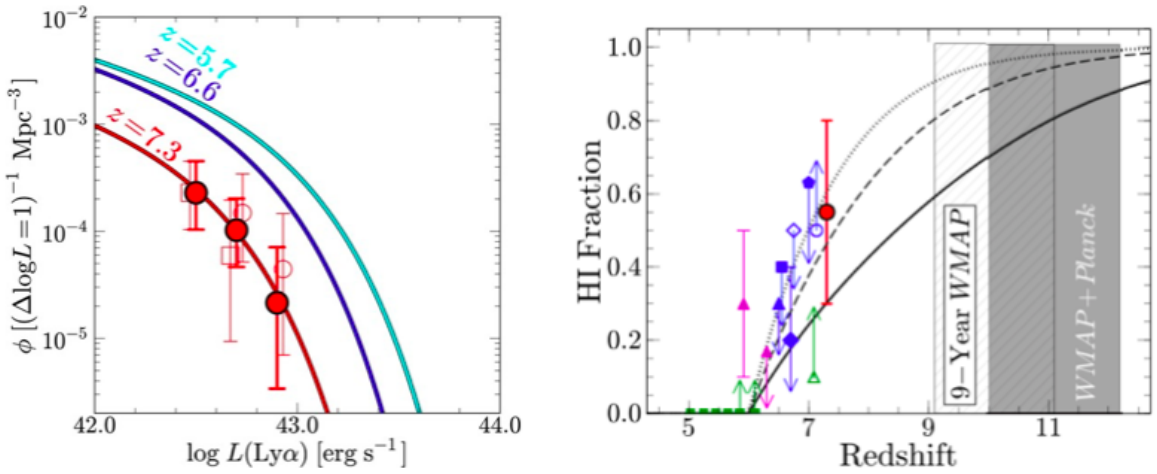

Figure 3.5: (*Left*) The luminosity function of LAEs for z=5.7, 6,6, 7.3. (*Right*) The evolution of neutral hydrogen fraction obtained by observations of the Lyα luminosity function. These figures are taken from [71].

Fig.3.6, we show the CMB E-mode angular power spectrum obtained by Planck. One can deduce the optical depth to Thomson scattering from the CMB E-mode polarization power spectrum. Thomson scattering optical depth is given by

$$\tau_T = \int_0^{z_{dec}} \sigma_T n_e \frac{cH_0^{-1} dz}{(1+z)\sqrt{\Omega_m (1+z)^3 + \Omega_\Lambda}}, \tag{3.7}$$

Here, z_{dec} is the redshift when the CMB photons decouple from baryons, σ_T is Thomson scattering cross section and n_e is the number density of electrons. Given a model for n_e, this optical depth could be turned into measurement of global reionization history. Based on instantaneous reionization model, we can measure $\tau_T = 0.067 \pm 0.023$ and $z_{re} = 8.9^{+2.5}_{-2.0}$(reionization redshift) by Planck result[98, 99].

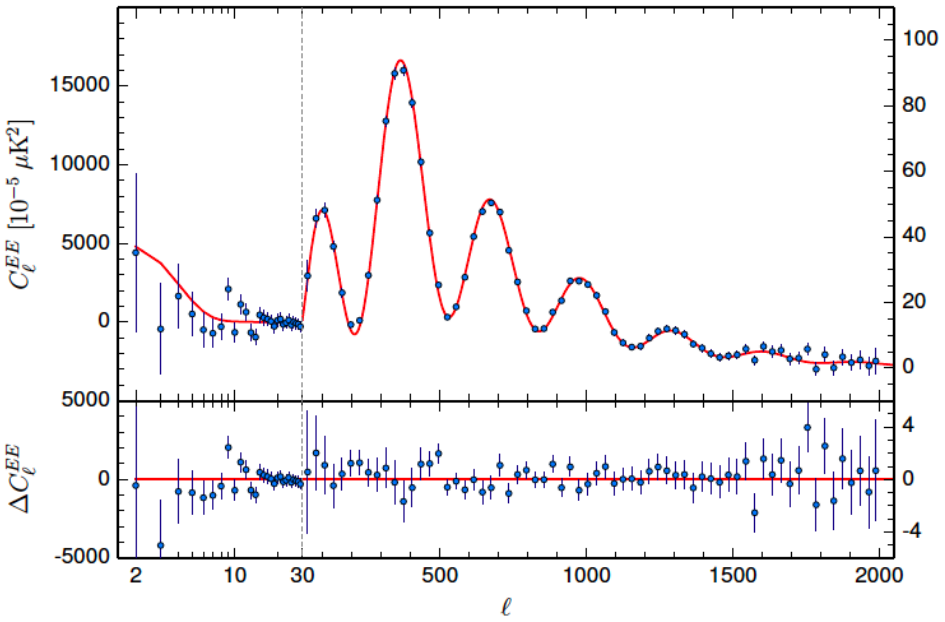

Figure 3.6: CMB E-mode polarization power spectrum as function of multipole l obtained by Planck. Solid line expresses theoretical one and points show data. We can see bump at low l, which is caused by Thomson scattering due to the EoR. This figure is taken from [99].

3.2.2 Basic physics of the EoR

In previous subsection, we summarized observational evidences for the EoR. Here, we describe basic physics of reionization process to discuss important aspects of the EoR. We first consider evolution of local ionized fraction of neutral hydrogen atoms $x_{\rm HII}$. It is governed by following equation.

$$\frac{dx_{\rm HII}}{dt} = k_{col}(T)(1 - x_{\rm HII})n_e - \alpha(T)x_{\rm HII}n_e + k_{ph}(1 - x_{\rm HII}), \tag{3.8}$$

where k_{col} is the collisional ionization coefficient, n_e is the number density of electrons and $\alpha(T)$ is recombination coefficient. k_{ph} is the photoionization rate expressed by

$$k_{ph} = \int d\Omega \int_{\nu_{\rm L}}^{\infty} \frac{I_\nu}{h\nu} \sigma_\nu d\nu, \tag{3.9}$$

where I_ν is the local specific intensity, $\sigma_\nu \sim 6.3 \times 10^{-18} (\nu/\nu_L)^{-3} {\rm cm}^{-2}$ is the ionization cross-section[132] and ν_L is the Lyman limit frequency. The first term in RHS of eq.(3.11) expresses collision ionization, the second term expresses recombination and the third term shows photoionization.

The photoionization process is tightly coupled to energy equation. The energy equation is given by

$$\frac{du}{dt} = \frac{\Gamma - \Lambda}{\rho}, \tag{3.10}$$

where u is internal energy of the gas per unit mass, Γ is the heating rate per unit volume and Λ is the cooling rate per volume. Both heating rate and cooling rate include following radiative processes; photo-heating, adiabatic heating(cooling), collisional ionization cooling, recombination cooling, collisional excitation cooling, Bremsstrahlung cooling and Compton heating(cooling). Photo-heating rate can be expressed by

$$\Gamma_{\rm ph} = n_{\rm HI} \int d\Omega \int_{\nu_L}^{\infty} \frac{I_\nu}{h\nu} (h\nu - h\nu_L) \sigma_\nu d\nu. \tag{3.11}$$

Ionized gas can be heated up to $10,000 - 20,000$[K] and pressure of the gas increases. This heating prevents the gas from collapsing gravitationally and small structures are smoothed by the pressure(photo-evaporation).

Here, we roughly evaluate key physical quantities in the EoR environments.

Mean free path of ionizing photons

In homogeneous medium, the mean free path of ionizing photons is evaluated by

$$l = \frac{1}{\sigma_\nu n_{\rm HI}} \sim 2 \left(\frac{10}{1+z} \right)^2 \left(\frac{\nu}{\nu_L} \right)^3 {\rm cMpc}. \tag{3.12}$$

Since width of ionization front is around the mean free path, ionization front becomes sharp in the case of UV radiation. On the other hand, the mean free path of X-ray photon ($E \gtrsim 1$keV) is ~ 1cGpc and this provides most uniform ionization field.

Recombination time

Another important quantity is the recombination time. In the ionized gas, temperature is kept around $T \sim 10^4$K. For this ionized gas, the recombination time at the average density of the Universe is evaluated by

$$t_{\rm rec} = \frac{1}{\alpha(T) n_{\rm H}} \sim 240 \left(\frac{10}{1+z} \right)^3 {\rm Myr}. \tag{3.13}$$

At high redshift($1 + z > 10$), the recombination time of dense structure(such as minihalos and filaments) is much shorter time of $\sim$ 10Myr and these structures act as photon sinks until photo-evaporation becomes effective.

Next we consider the ionization processes. The important processes for ionization is escape of the ionizing photons from galaxies and radiative feedback by galaxies. We briefly introduce these two processes.

Escape of the ionizing photons

In order to understand ionization history, it is important to estimate the number of ionizing photons escaping from galaxies. It is useful to divide this quantity into the star formation rate(SFR) and escape fraction f_{esc}. Although observational estimate of escape fraction is difficult because of strong absorption by the IGM, some observations provide constraint on escape fraction at $z \sim 3$[124, 65]. These observations suggest that $f_{esc} \sim 0.04 - 0.3$. A few observational studies provide tentative result of escape fraction at higher redshift ($z \sim 5-8$) based on simple model that stellar sources are main contributor to reionization. Theoretically, we can estimate f_{esc} by running numerical simulations including ionizing continuum radiative transfer and the dynamics of the gas[50, 136, 140, 138]. Although results do not converge since they do not use similar modeling nor resolution, these simulations show that escape fraction decreases with the mass of host halo and increases with redshift.

Feedback on primordial galaxies

Another important aspect of ionizing process is radiative feedback such as radiative pressure, photo-heating, photo-evaporation of the gas in galaxies and of accreting gas[64, 137, 57]. These radiative process affect not only star formation rate but also escape fraction. Further, photo-dissociation destroys hydrogen molecules which are responsible to cooling process at the early Universe. Thus, this radiative feedback also affects star formation rate. It is important to treat radiative feedback adequately for evaluating the amount of ionizing photons from galaxies.

3.3 Analytic model for the EoR

Process of hydrogen reionization has different stages shown in Fig.3.7. Initial phase of reionization is *pre-overlap* stage in which individual ionizing sources emit ionizing photons and ionize their surroundings. The first galaxies at high redshift form in high-density regions. At such regions, the recombination rate is also high. Thus, the ionizing photons escaping from galaxies must pass through such high-density regions. Once pre-overlap phase starts, the ionization fronts propagate to low-density regions. During this stage, the IGM is separated by two phases. The first one is highly ionized regions separated from neutral regions due to the ionization fronts and the other is high-density, neutral regions.

Since first luminous objects are highly clustered, the pre-overlap phase easily enters next phase called *overlap* phase of reionization. At this phase, two or more HII regions surrounding each individual galaxies begin to overlap and these galaxies are common in the overlap bubble. Thus, each point in this common ionized bubble has common boundary which is exposed to common ionizing photons from each galaxy. Because each galaxy

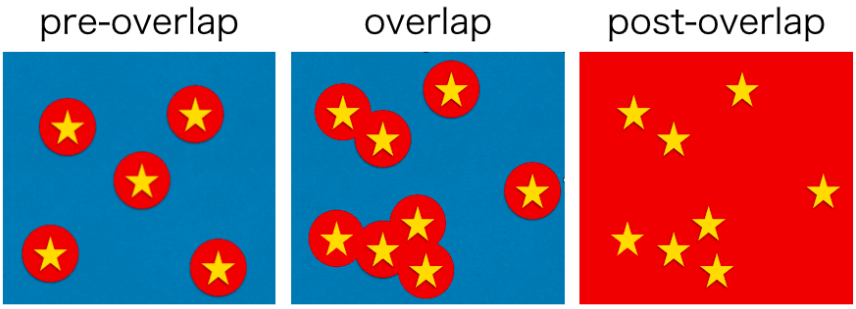

Figure 3.7: Phases of reionization. (*left*) pre-overlap phase: In this phase, galaxies are separated from others and isolated HII regions grow around sources. (*middle*) overlap phase: In this phase, two or more ionized bubbles begin to intersect rapidly. However, the regions which have a highly recombination rate enough to prevent themselves from being ionized remain neutral. (*right*) post-overlap phase: As HII regions grow sufficiently, neutral regions are forced to be ionized gradually.

inside overlap ionized bubble can contribute to reionization, HII regions grows rapidly during overlap phase. This allows highly ionized regions to expand into IGM where once cannot be ionized due to high recombination rate enough to keep neutral state. During this phase, ionizing photons can travel in the IGM without absorption because many parts of the gas are highly ionized and this makes inhomogeneous structure of the Universe. On the other hand, some regions remain neutral pockets of the IGM due to extremely high recombination rate. These neutral regions absorb any ionizing photons and prevent the HII regions from continuing to grow. Eventually, ionized regions become much larger and they provide neutral regions with so large amount of ionizing photons that these regions are gradually ionized. This final stage is called *post-overlap* phase.

As we saw in sec 3.2.2, we need to understand each astrophysical process related to the ionization and recombination in order to calculate reionization process accurately. In particular, the post-overlap stage of reionization needs to solve complex physics of ionizing sources and sinks of ionizing photons. Some previous works study how HII region evolves by means of booth analytic and numerical methods[41, 42, 112]. However, reionization proceeds straightforward until post-overlap phase. It requires simple physics, that is, to count photons contributing to ionization. Thus, an analytic model can give physical insight into morphology of reionization. In this section, we introduce analytic model for the EoR to get physical insight into evolution of ionization history.

3.3.1 Propagation of ionization fronts

We begin to discuss how a single, isolated galaxy ionizes regions around itself. The formation of HII regions or ionized bubble by ionizing photons escaping from galaxies is fundamental process that drives reionization. Although the assumption that galaxies are isolated is realized only at early stage of reionization, we consider this condition for simplicity.

Let us consider a spherical ionized volume V, which is separated from neutral region. If we can ignore recombination of hydrogen atoms, each hydrogen atom in the IGM is ionized only once. At this situation, the proper ionized volume V_p is determined by

$$\bar{n}_H V_p = Q_{ion}, \tag{3.14}$$

where $\bar{n}_H$ is the mean number density of hydrogen atoms and Q_{ion} is total number of ionizing photons produced by a single source.

In order to estimate Q_{ion} roughly, we introduce a parameter called *ionizing efficiency* ζ,

$$\zeta = f_* f_{\rm esc} N_{ion}, \tag{3.15}$$

where f_* is a fraction of baryons incorporated into stars, $f_{\rm esc}$ is escape fraction from galaxies into the IGM and N_{ion} is the number of ionizing photons per baryon inside star. Typically, N_{ion} is$\sim$ 4000 for Pop II stars suggested by present Initial Mass Function (IMF).

If we can neglect recombinations, the maximum comoving radius of HII region is roughly estimated by

$$r_{\rm max} = \left(\frac{3}{4\pi}\frac{Q_{ion}}{\bar{n}_{\rm H}^0}\right)^{1/3} = \left(\frac{3}{4\pi}\frac{\zeta}{\bar{n}_{\rm H}^0}\frac{\Omega_b}{\Omega_m}\frac{M}{m_p}\right)^{1/3} \tag{3.16}$$

$$= 680\left(\frac{\zeta}{40}\frac{M}{10^8 M_\odot}\right)^{1/3}[\rm kpc], \tag{3.17}$$

where $\bar{n}_{\rm H}^0 = 2.1\times10^{-7}[\rm cm^{-3}]$ is the present number density of hydrogen atoms and M is mass of a halo. Here we used $f_* = 0.1$ and $f_{\rm esc} = 0.08$ as fiducial values in the case of Pop II star.

However, recombinations actually cannot be ignored because high density region of the IGM exists. Hence this simple estimation should be improved. Bengt Strömgren studied the same problem for the hot star surrounded by Inter Stellar Medium(ISM). In the case of steady ionizing sources without effect of the expanding Universe, steady-state volume termed a *Strömgren sphere* is reached. Inside a Strömgren sphere, recombination is balanced with ionization:

$$\alpha_B \bar{n}_{\rm H}^2 V_p = \frac{dQ_{ion}}{dt}. \tag{3.18}$$

The left-hand-side term expresses recombination rate, α_B is the recombination coefficient. Here, we assume a case-B recombination rate. Case-B recombination is that a hydrogen atom recombines indirectly to the ground state and does not re-emit photons capable of ionizing neutral hydrogen atom.

Including non-steady ionizing sources, recombination and expansion of the Universe, we can write down the evolution of H II region as follows:

$$\bar{n}_{\rm H}\left(\frac{dV_p}{dt} - 3HV_p\right) = \frac{dQ_{ion}}{dt} - \alpha_B\langle n_{\rm H} n_e\rangle V_p. \tag{3.19}$$

We used that the mean density $\bar{n}_{\rm H}$ evolves $\bar{n}_{\rm H} \propto a^{-3}(t)$. The $\langle n_{\rm H} n_e\rangle$ is a volume average of the product of the number density of hydrogen atoms and that of electrons. The recombination rate is proportional to the square of the number density. Thus, inhomogeneities are going to play an important role in determining the evolution of HII region. We often

account for the IGM inhomogeneity by introducing a volume-averaged clumping factor C defined by

$$C = \frac{\langle n_e^2 \rangle}{\langle \bar{n}_e^2 \rangle} \tag{3.20}$$

Generally, a clumping factor depends on time. For homogeneous Universe, C=1.

Switching to the comoving volume V, eq.(3.19) becomes

$$\frac{dV}{dt} = \frac{1}{\bar{n}_{\rm H}^0}\frac{dQ_{ion}}{dt} - \alpha_B \frac{C}{a^3}\bar{n}_{\rm H}^0 V. \tag{3.21}$$

The solution for this equation is given by

$$V(t) = \int_{t_i}^{t} \frac{1}{\bar{n}_{\rm H}^0}\frac{dQ_{ion}}{dt} e^{F(t',t)dt'}. \tag{3.22}$$

Here, HII region around a source turns on $t = t_i$ and $F(t^{'}, t)$ is

$$F(t^{'}, t) = -\alpha_B \bar{n}_{\rm H}^0 \int_{t_i}^{t} \frac{C(t'')}{a^3(t'')} dt''. \tag{3.23}$$

Note that this comoving volume V is filled by the fully ionized gas. Instead of V, we can obtain the solution for the total number of ionized atoms N_i. N_i is related to V via $N_i = \bar{n}_{\rm H}^0 V$. This simple model is not accurate because this model considers only single sources. However it is useful for steady source where recombination is unimportant and it can help understand global ionization history in next subsection.

3.3.2 Global ionization history

Next step to understand reionization is to compute evolution of the average neutral hydrogen fraction (or average HII region fraction) in the Universe. First of all, we introduce a simple model which connects HII region to the number of ionizing photons emitted by galaxies. The efficiency parameter ζ is the number of ionizing photons impacting the IGM produced per baryon inside galaxies. By using this efficiency parameter, we can write down the average filling factor of ionized bubbles (*i.e*, the fraction of the volume of the Universe inside HII regions), $Q_{\rm HII}$, in the case without taking recombination into account:

$$Q_{\rm HII} = \zeta f_{\rm coll}. \tag{3.24}$$

$f_{\rm coll}$ is the collapse fraction which expresses the fraction of matter incorporated into halo[see sec 2.5]. $f_{\rm coll}$ depends on the threshold halo mass in which star formation can start, specified volume size and overdensity inside this volume. If we assume that only atomic cooling is effective as a cooling process in a halo during reionization, the minimum mass typically corresponds to a halo of virial temperature $T_{vir} = 10^4$[K][see eq.(2.47)]. Given the ionizing efficiency ζ and $f_{\rm coll}$, we can estimate the filling factor $Q_{\rm HII}$. Note that the eq.(3.24) assumes that ionizing photons are produced instantaneously.

Since we ignore recombination in eq.(3.24), we next improve this simple model by taking recombination into account. In order to do so, we treat each ionizing source as producing

an isolated bubble and assume that each bubble volume is added to give the total filtering factor. In fact, overlap of ionized regions becomes important after reionization proceeds sufficiently. However, this assumption remains good approximation until Q reaches unity even if two or more bubbles overlap because the total recombination rate is in proportion to the number of ionized volume independent of topology of HII regions.

With above discussion, we convert eq.(3.21), which describes the evolution of individual HII regions by ionizing photons emitted by a single isolated galaxies, to the equation which governs global evolution of $Q_{\rm HII}$ in the Universe as follows:

$$\frac{dQ_{\rm HII}}{dt} = \zeta \frac{df_{\rm coll}}{dt} - \alpha(T)\frac{C}{a^3}\bar{n}_{\rm H}^0 Q_{\rm HII}. \tag{3.25}$$

$\alpha(T)$ is the recombination rate depending on temperature. As with the discussion about ionization by a single galaxy, this equation has a solution such as

$$Q_{\rm HII}(t) = \int_0^t \zeta \frac{df_{\rm coll}}{dt'} e^{F(t',t)} dt' \tag{3.26}$$

where $F(t',t)$ is given by eq.(3.23).

Although this solution has a simple form, it includes some uncertain parameters. We need to know properties such as the star formation efficiency and the escape fraction of ionizing photons from galaxies into the IGM to determine Ionizing efficiency ζ and also to solve the time evolution of a clumping factor C, which depends on morphology of the ionization field.

We show that time evolution of $Q_{\rm HII}$ in the case of C=0, 1, 10, 30 in Fig.3.8. Note that if $C \sim 1$, then effect of recombination is unimportant. However, if $C \gtrsim 10$, recombination affects the evolution of $Q_{\rm HII}$ and delays reionization.

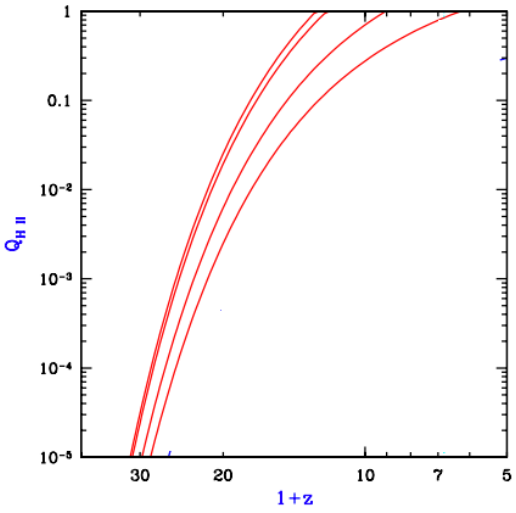

Figure 3.8: Evolution of $Q_{\rm HII}$ as function of redshift solved by semi-numerical method. This figure is taken from [5]. Each curve corresponds $Q_{\rm HII}$ for C=0, 1, 10, 30 from left to right.

3.3.3 The morphology of reionization

Obviously, morphology of the ionization field depends on distribution of galaxies which drive reionization. Given physics of ionizing sources and sinks of ionizing photons in the IGM, it seem that we can determine the morphology of the ionization field and its evolution. Recent numerical simulations suggest that reionization proceeds from high density regions to low density regions on large scale[123]. This is called *inside-out* reionization. On the other hand, on sufficiently small scale, reionization proceeds from low-density region to high-density region since high-density blobs remain neutral state partially due to its high recombination rate. This model is called *outside-in* reionization [93].

In [41, 42], they developed an analytic formalism to study morphology of ionized regions based on inside-out model. In this analytic model, they associate ionized regions with density fluctuations and use the excursion set theory formalism(see sec 2.5) to model size distribution of ionized regions. We consider condition that neutral region can be ionized. We assume that a galaxy with mass m_{gal} can ionize the gas with mass of $m_{ion} = \zeta m_{gal}$. ζ is ionizing efficiency. Under this assumption, we count the number of ionizing photons and that of neutral hydrogen atoms inside some specified regions. If the former exceeds the latter, the regions can be ionized. We put condition for the region to be ionized by $\zeta f_{coll} \geq 1$, where f_{coll} is the fraction of halos mass collapsed above m_{min}. If the regions satisfy with this condition, this region is regarded as being fully ionized. In the extended Press-Schechter theory(see sec2.5), f_{coll} is given by

$$f_{coll} = \mathrm{erfc}\left[\frac{\delta_c(z) - \delta_m}{\sqrt{[\sigma^2_{\min} - \sigma^2(m)]}}\right], \tag{3.27}$$

where δ_m is matter overdensity at the regions., $\sigma^2(m)$ is the variance of density fluctuations on smoothed scale m, $\sigma^2_{min} = \sigma^2(m_{min})$, and $\delta_c(z)$ is the critical density for collapse. We generally set mass corresponding to $T_{\rm vir} = 10^4$K as m_{min}. This is because atomic cooling becomes effective at this virial temperature.

The condition $\zeta\delta_m \geq 1$can be rewritten by

$$\delta_m \geq \delta_x(m, z) = \delta_c(z) - \sqrt{K}(\zeta)[\sigma^2_{min} - \sigma^2(m)]^{1/2}, \tag{3.28}$$

where $K(\zeta) = \mathrm{erf}^{-1}(1 - \zeta^{-1})$. We see that regions with sufficiently large overdensities will be able to "self-ionize". This condition is used in 21cmFAST to judge whether regions can be ionized or not(see sec4.6.1).

According to [41, 42], the barrier δ_x is well approximated by a linear function of $\sigma^2(m)$ such as $\delta_x \sim B(m, z) = B_0 + B_1\sigma^2(m)$, where B_0 and B_1 are fitting constant. This linear barrier is reasonable approximation to the true barrier for $\sigma^2(m)$ that are not too large.

With this barrier B, the mass function of HII regions can be given by an analogy with the Press-Schecther prescription as follows;

$$m\frac{dn}{dm} = \sqrt{\frac{2}{\pi}}\frac{\bar{\rho}}{m}\left|\frac{d\log\sigma}{d\log m}\right|\frac{B_0}{\sigma(m)}\exp\left[-\frac{B^2(m, z)}{2\sigma^2(m)},\right] \tag{3.29}$$

where $\bar{\rho}$ is the mean density of the Universe. This is the comoving number density of HII regions with mass in the range$(m, m + dm)$. We show the HII region size distribution as

function of comoving R for z=18, 16, 14, 13, 12 in Fig.3.9. We have normalized each curve by $\bar{Q}$ defined by

$$\bar{Q} = \int dm \frac{dn}{dm} V(m), \tag{3.30}$$

where, $V(m)$ is the comoving volume of a bubble of mass m.

When reionization does not proceed, the regions are small, with characteristic sizes $\lesssim 0.5$Mpc. However, the sizes rapidly increase as reionization proceeds and the typical size of bubbles become several megaparsecs. We also can see that the number of small bubbles decrease and that of large bubbles increase as reionization proceeds.

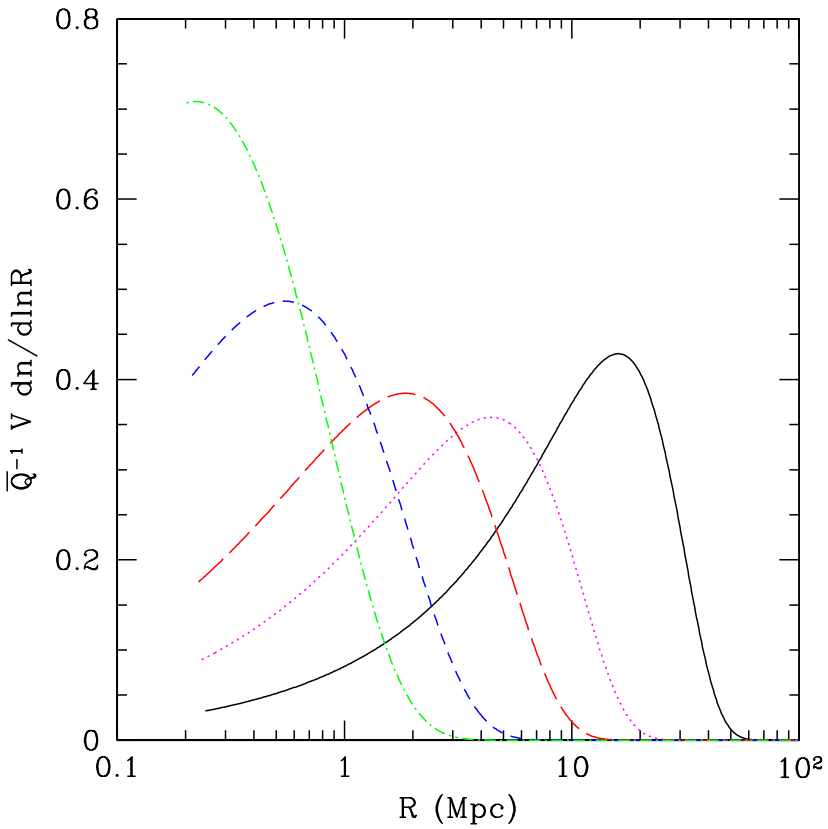

Figure 3.9: HII bubble size distribution as function of R (comoving size). From left to right, these lines correspond to z=18, 16, 14, 13, 12, respectively. This figure is taken from[41].

Chapter 4

Basic physics of the cosmological 21 cm line

A promising tool to measure the epoch through the Dark Ages to cosmic reionization is the 21 cm line due to the hyperfine structure of a neutral hydrogen. A hydrogen atom in the triplet state undergoes the spin-flip transition with emission which has a wavelength of 21 cm in the rest frame (Fig.4.1). This transition per atom occurs with a rate of $2.9 \times 10^{-15}\mathrm{s}^{-1}$. This weak transition enables us to access the IGM during the Dark Ages and the EoR because the effective optical depth of the IGM to the 21 cm line is relatively small compared with that of the IGM to Lyα photons. The rare transition rate seems to make us difficult to observe this transition. However, the column density of hydrogen atoms in the IGM is sufficiently large. As the result, we can observe this transition in the Universe. This is why the 21 cm emission is powerful tool to observe the Universe through the Dark Ages to the EoR. In this section, we study basic physics of the 21 cm line based on [43, 106, 46].

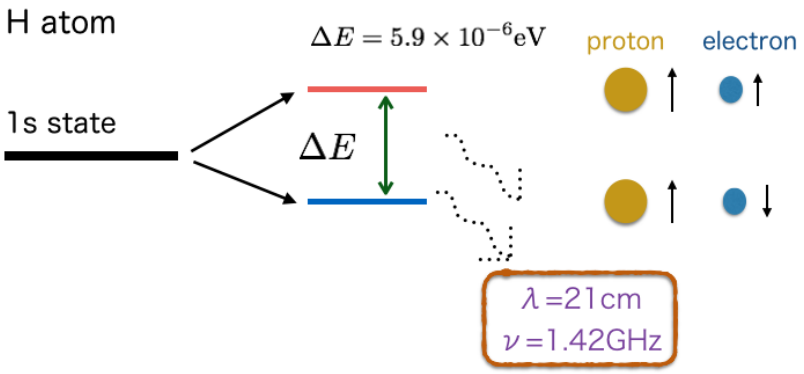

Figure 4.1: Hyperfine structure of a neutral hydrogen atom. The 21 cm line emission arises from the hyperfine splitting of the 1S ground state due to the interaction of the magnetic moments between the proton and the electron.

4.1 Radiative transfer

In this section, we introduce a radiative transfer equation to describe the propagation of the radiation in the IGM based on [111]. The radiative transfer equation for an infinitesimal distance ds is written by

$$\frac{dI_\nu}{ds} = -\alpha_\nu I_\nu + j_\nu. \tag{4.1}$$

Here, the subscript ν denotes frequency. I_ν is the intensity of the incident light and α_ν is an absorption coefficient. The incident light passing through the IGM is absorbed and the intensity of the incident light decreases by $\alpha_\nu I_\nu$. j_ν is the emission coefficient j_ν[erg cm^{-3} s^{-1} ster^{-1}Hz^{-1}]. Here, we define a new parameter called the *optical depth*, which is related to the absorption coefficient such as $d\tau_\nu \equiv \alpha_\nu ds$. We also define the *source function* as $S_\nu \equiv j_\nu/\alpha_\nu$. Then, eq.(4.1) is re-written by

$$\frac{dI_\nu}{d\tau_\nu} = -I_\nu + S_\nu. \tag{4.2}$$

The source function is expressed by the Planck function under the thermal equilibrium state.

$$S_\nu = B_\nu = \frac{2h\nu^3/c^2}{\exp(h\nu/k_{\rm B}T) - 1}. \tag{4.3}$$

In this case, the solution of eq.(4.2) is given by

$$\begin{aligned} I_\nu &= I_\nu(0)\exp(-\tau_\nu) + B_\nu \int_0^{\tau_\nu} \exp[-(\tau_\nu - \tau_\nu^{'})]d\tau_\nu^{'} \\ &= I_\nu(0)\exp(-\tau_\nu) + B_\nu[1 - \exp(-\tau_\nu)]. \end{aligned} \tag{4.4}$$

The physical meaning of this equation is following one. The first term expresses the extinct incident light absorbed by the IGM with the optical depth τ_ν and the second term shows extinct emission from the source as shown in Fig.4.2. Note that we can obtain this solution only in the case that the source function does not include the intensity I_ν. If we have to take the scattering account into, the source function includes I_ν, we cannot obtain a simple solution such as eq.(4.4).

Since we are interested in the 21 cm line radio emission, we can use the Rayleigh-Jeans approximation. By using the Rayleigh-Jeans approximation, I_ν, $I_\nu(0)$ and B_ν can be given by $I_\nu = 2k_{\rm B}T_{\rm b}\nu^2/c^2$, $I_\nu(0) = 2k_{\rm B}T_R(\nu)\nu^2/c^2$ and $B_\nu = 2k_{\rm B}T_{ex}\nu^2/c^2$, respectively. T_b, T_{ex} and T_R are called *the brightness temperature*, *the excitation temperature* and *the brightness temperature* of the radio background source, respectively. The brightness temperature is used instead of the intensity with the Rayleigh-Jeans approximation. The excitation temperature is defined by a ratio of the number density of electrons between the two energy states as follows:

$$\frac{n_2}{n_1} = \frac{g_2}{g_1}\exp\left(-\frac{h\nu}{k_{\rm B}T_{ex}}\right). \tag{4.5}$$

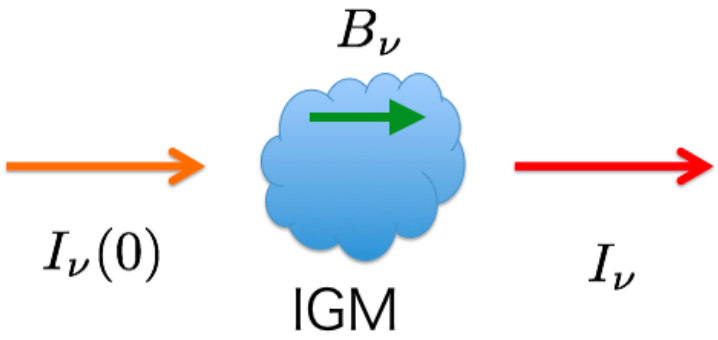

Figure 4.2: A schematic figure of the radiative transfer.

Here, n_1 and n_2 are the number density of the energy state for state 1 and state 2 respectively, g_1 and g_2 are the statistical degree of freedom for each state. Eq.(4.4) can be re-written in the form of temperature as

$$T_{\rm b} = T_R(\nu)\exp(-\tau_\nu) + T_{ex}[1-\exp(-\tau_\nu)] \tag{4.6}$$

In the case of the 21 cm line emission, the spin temperature is known as the excitation temperature and the CMB temperature is regarded as T_R. The spin temperature is defined by the ratio between the triplet and the singlet.

$$\begin{aligned} \frac{n_1}{n_0} &= \frac{g_1}{g_0}\exp\left(-\frac{h\nu_{21}}{k_{\rm B}T_{\rm S}}\right) \\ &= 3\exp\left(-\frac{T_*}{T_{\rm S}}\right) \end{aligned} \tag{4.7}$$

n_1 and n_0 are the number density of electrons for the triplet and the singlet respectively. g_1 and g_0 are the statistical degree of freedom for each state and g_1/g_0 becomes 3 for the case of a neutral hydrogen atom. $\nu_{21} = 1420$MHz corresponding to the frequency of the emission with $\lambda = 21$cm in the rest frame. $h\nu_{21}/k_B \equiv T_* = 0.068$K.

Thus, eq.(4.6) becomes

$$T_{\rm b} = T_\gamma(\nu)\exp(-\tau_\nu) + T_S[1-\exp(-\tau_\nu)], \tag{4.8}$$

where T_γ is the CMB temperature. In order to calculate the brightness temperature, we need to consider the $T_{\rm S}$ and τ_ν in detail. Thus, we investigate these following two sections.

4.2 Spin temperature

The spin temperature of neutral hydrogen atom is determined by following three interactions:

(1) Absorption of the CMB photons

(2) Collisions with other hydrogen atoms and free electrons

(3) Resonant scattering of Lyα photons

Here, we let C_{10} and P_{10} be the de-excitation rates from collisions and the UV scattering, respectively. We also let C_{01} and P_{01} be the excitation rates. We consider the equilibrium state between the excitation and the de-excitation as follows;

$$n_1(C_{10} + P_{10} + A_{10} + B_{10}I_{\rm CMB}) = n_0(C_{01} + P_{01} + B_{01}I_{\rm CMB}), \tag{4.9}$$

where A_{10}, B_{01} and B_{10} are the Einstein coefficients. A_{10} coefficient denotes a spontaneous emission. B_{01} and B_{10} are the appropriate Einstein coefficients. $I_{\rm CMB}$ is the energy flux of the CMB photon. The first and second terms in left-hand-side express the transition from the triplet to the singlet due to collision and UV scattering respectively, third and fourth terms in left-hand-side express the transition from triplet to the singlet due to the spontaneous emission and stimulated emission due to the CMB photons, respectively. Conversely, first and second terms in right-hand-side mean the transition from the singlet to the triplet by the collisions and UV scattering, respectively. Third term in right-hand-side expresses the stimulated transition from the singlet to the triplet cause by the absorption of the CMB photons.

There are following relations among the Einstein coefficients;

$$A_{10} = \frac{2h\nu_{21}^3}{c^2}B_{10} \tag{4.10}$$

$$B_{01} = 3B_{10}. \tag{4.11}$$

With Rayleigh-Jeans approximation, CMB intensity is expressed by the form of the CMB temperature $T_\gamma = 2.73(1+z)$,

$$I_{\rm CMB} = \frac{2\nu_{21}^2}{c^2}k_{\rm B}T_\gamma. \tag{4.12}$$

The excitation and de-excitation rates due to collision satisfy

$$\frac{C_{01}}{C_{10}} = \frac{g_1}{g_0}\exp\left(-\frac{T_*}{T_{\rm K}}\right) \sim 3\exp\left(1-\frac{T_*}{T_{\rm K}}\right), \tag{4.13}$$

where $T_{\rm K}$ is the kinetic temperature and generally $T_{\rm K} \gg T_* = 0.082{\rm mK}$. Here, we also define the color temperature of the UV radiation field T_C analogous to the kinetic temperature:

$$\frac{P_{01}}{P_{10}} \equiv 3\left(1-\frac{T_*}{T_{\rm c}}\right). \tag{4.14}$$

Now, we rewrite eq.(4.7) with eq.(4.9)-eq.(4.14).

$$3\left(1-\frac{T_*}{T_{\rm S}}\right) = \frac{3(1-T_*/T_{\rm K})C_{10} + 3(1-T_*/T_{\rm C})P_{10} + 3A_{10}T_\gamma/T_*}{C_{10} + P_{10} + A_{10}(1+T_\gamma/T_*)} \tag{4.15}$$

$\Longrightarrow$

$$\frac{T_*}{T_{\rm S}} = \frac{(C_{10}+P_{10})+A_{10}(1+T_\gamma/T_*)-(1-T_*/T_{\rm K})C_{10}-(1-T_*/T_{\rm C})P_{10}-A_{10}T_\gamma/T_*}{(C_{10}+P_{10})+A_{10}(1+T_\gamma/T_*)}$$
$$= \frac{A_{10}+C_{10}T_*/T_{\rm K}+P_{10}T_*/T_{\rm C}}{(C_{10}+P_{10})+A_{10}+A_{10}T_\gamma/T_*} \tag{4.16}$$

Then, the inverse of $T_{\rm S}$ becomes

$$T_{\rm S}^{-1} = \frac{T_\gamma^{-1}+\frac{C_{10}T_*}{A_{10}T_\gamma}T_{\rm K}^{-1}+\frac{P_{10}T_*}{A_{10}T_\gamma}T_{\rm C}^{-1}}{(C_{10}+P_{10})T_*/(A_{10}T_\gamma)+1+T_*/T_\gamma}. \tag{4.17}$$

Here, we define the coupling coefficients for collisions and UV scattering, x_c, x_α as follows;

$$x_c \equiv \frac{C_{10}T_*}{A_{10}T_\gamma} \tag{4.18}$$

$$x_\alpha \equiv \frac{P_{10}T_*}{A_{10}T_\gamma}, \tag{4.19}$$

Finally, we can obtain

$$T_{\rm S}^{-1} = \frac{T_\gamma^{-1}+x_cT_{\rm K}^{-1}+x_\alpha T_{\rm C}^{-1}}{1+x_c+x_\alpha} \tag{4.20}$$

Note that we ignore T_*/T_γ because of $T_*/T_\gamma \ll 1$. This formula of the spin temperature is well used to consider the 21 cm line. Each term in numerator denotes interaction with the CMB photon, collision with other hydrogen atoms and UV scattering. In order to determine the spin temperature, we need to know x_α and x_c. We see them in following subsections.

4.2.1 Collisional coupling

First, we consider the collisional excitation by scattering between hydrogen atoms and other particles. The scattering in the early Universe occurs in the dense gas. Main processes of collision are

(1) H-H collisions

(2) H-e collisions

(3) H-p collisions

The coupling coefficient for species i (H-H, H-e, H-p) is given by

$$x_c^i \equiv \frac{C_{10}^i T_*}{A_{10}T_\gamma} = \frac{n_i\kappa_{10}^i}{A_{10}}\frac{T_*}{T_\gamma}, \tag{4.21}$$

where κ^i_{10}[with units of $\mathrm{cm^3 s^{-1}}$] is a rate coefficient (as function of temperature) which describes how often collisions occur. These values are calculated by [147, 43, 44, 45]. We show κ^i for each collision in Fig.4.3. From Fig.4.3, we can see that the rate coefficients for H-e and H-p collisions change gradually as temperature increases. On the other hand, that for H-H collisions changes drastically at around $T \sim 10$K. This is because a hydrogen atom is unable to move violently due to its heavy mass at low temperature. Thus, the cross section is small at less than $\sim$ 10K. During the Cosmic Dawn, neutral hydrogen atom is dominant component. Therefore, the scattering among hydrogen atoms becomes dominant. Once the EoR begins, the number of electrons increases and this leads the scattering between hydrogen atoms and electrons.

With the rate coefficients, the total collisional coefficient can be given by

$$x_c = x_c^{\mathrm{HH}} + x_c^{\mathrm{eH}} + x_c^{\mathrm{pH}} = \frac{T_*}{A_{10} T_\gamma} \left[\kappa_{10}^{\mathrm{HH}}(T_{\mathrm{K}}) n_{\mathrm{H}} + \kappa_{10}^{\mathrm{eH}}(T_{\mathrm{K}}) n_{\mathrm{e}} + \kappa_{10}^{\mathrm{pH}}(T_{\mathrm{K}}) n_{\mathrm{p}} \right], \tag{4.22}$$

where $n_{\mathrm{H}}, n_e, n_{\mathrm{p}}$ are the number density of hydrogen atoms, electrons and protons respectively.

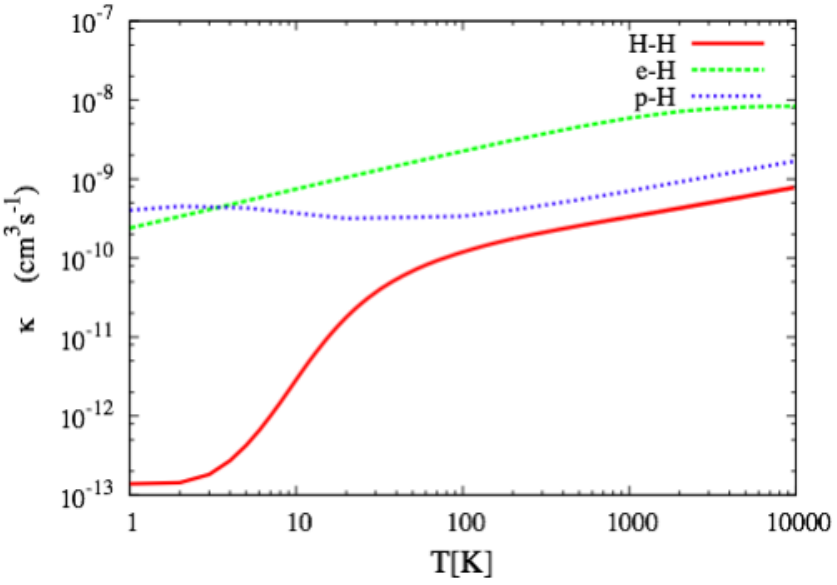

Figure 4.3: Rate coefficients as a function of temperature for each collision, H-H collisions(solid line), H-e collisions(dashed line), H-p collisions(dotted line) [147, 43, 44, 45].

4.2.2 Wouthuysen-Field effect

Once first stars form, the resonant scattering of Lyα photons emitted by them provides a second channel for coupling. This process is known as *the Wouthuysen Field effect* [139]. We illustrate this effect in Fig.4.4. We show the hyperfine structure of hydrogen in Fig.4.4. A hydrogen atom in the singlet state ${}_0S_{1/2}$ is excited to 2P hyperfine state by absorption of Lyα photons (Δ F=0,1 transition is allowed but F=0$\rightarrow$ 0 is inaccessible by the selection

rule. Here F is total angular momentum). The selection rule allows 2P hyperfine levels to slip to ${}_1S_{1/2}$ by re-emission of Lyα photon. Thus, this hydrogen atom can change its hyperfine energy state through the absorption and re-emission of Lyα photons.

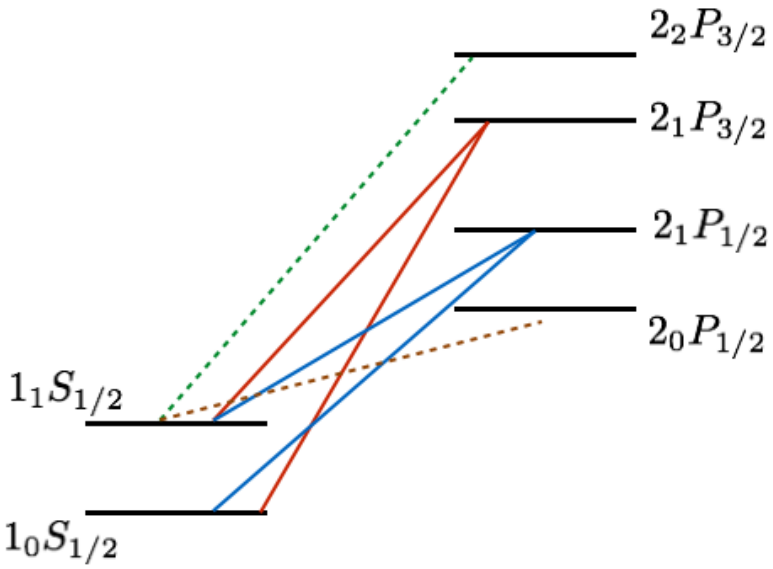

Figure 4.4: Hyperfine structure of the hydrogen atom. We show the transition between S states and P states related to Wouthuysen-Field (WF) effect. Solid lines show the process allowed by the selection rule and spin flip can occur in this process. While dashed lines are allowed, these processes do not contribute to spin flip.

We start to consider physics of the WF effect. We can write the coupling coefficient of the WF effect as

$$x_\alpha = \frac{4P_\alpha}{27A_{10}}\frac{T_*}{T_\gamma}, \tag{4.23}$$

where, P_α is the scattering rate of Lyα photons and there is a relation between the scattering coefficient of UV photons and that of Lyα photons shown in eq.(4.19) such as

$$P_{10} = \frac{4P_\alpha}{27}. \tag{4.24}$$

This relation comes from atomic physics of the hyperfine lines[85].

The rate at which Lyα photons scatter from a hydrogen atom is given by

$$P_\alpha = 4\pi\chi_\alpha \int d\nu J_\nu(\nu)\phi_\alpha(\nu) \tag{4.25}$$

where, $\chi_\alpha \equiv (\pi e^2/m_e c)f_\alpha, f_\alpha = 0.4162$ is the oscillation strength of Lyα transition and $\phi_\alpha(\nu)$ is the line profile for Lyα absorption. Combined with these two physical values, we can define the local absorption cross section $\sigma_\nu = \chi_\alpha\phi_\alpha(\nu)$, and $J_\nu(\nu)$ is the angle averaged specific intensity of the background radiation field.

Making use of this expression, we can express the coupling coefficient as

$$x_\alpha = \frac{16\pi^2 T_* e^2 f_\alpha}{27 A_{10} T_\gamma m_e c} S_\alpha J_\alpha, \tag{4.26}$$

where J_α is the specific flux evaluated at Lyα frequency. We introduce a correction factor $S_\alpha \equiv \int dx \phi_\alpha(x) J_\nu(x)/J_\infty$, which takes the variation at line center account into, with J_∞ being flux away from the line center. We often rewrite eq.(4.26) such as $x_\alpha = S_\alpha J_\alpha / J_\alpha^C$ where $J_\alpha^C = 1.165 \times 10^{-10}[(1+z)/20][\mathrm{cm^2 s^{-1} Hz^{-1} sr^{-1}}]$. The fitting formula for S_α is given by [59]. We give details description of J_α in section 4.6.3.

The above physics couples the spin temperature via the color temperature defined at eq.(4.14), which is a measure of the shape of the radiation field as function of frequency in neighborhood of the Lyα line defined by

$$\frac{h}{k_\mathrm{B} T_\mathrm{C}} = -\frac{d \log n_\nu}{d\nu} \tag{4.27}$$

Here, $n_\nu = c^2 J_\nu / 2\nu^2$. Obviously, the color temperature is function of frequency.

Note that some arguments show $T_\mathrm{C} \sim T_\mathrm{K}$. Because the optical depth to Lyα scattering is very large in the most case of our interests, the large amount of Lyα photons is brought to the radiation field by the Lyα scattering. These photons lead the gas into the local equilibrium near the line center.

4.3 Optical depth

In previous section, we discussed the spin temperature which is one of the key values to determine the brightness temperature. Here, we discuss the optical depth which is another key value. Let us consider the amount of the energy emitted in volume dV, solid angle $d\Omega$, frequency $d\nu$, time dt. The total amount of the energy is given by $j_\nu dV d\Omega d\nu dt$. Alternatively, this also can be expressed by $(h\nu/4\pi)\phi(\nu) n_1 A_{10} dV d\Omega d\nu dt$ since each atom can contribute to an energy $h\nu$ distributed over 4π solid angle for each radiation. Here, $\phi(\nu)$ is the line profile which describes deviation of infinitely sharpness between two energy level and this satisfies $\int_0^\infty \phi(\nu) d\nu = 1$.

With these two expressions of total amount energy, we can obtain

$$j_\nu = \frac{h\nu}{4\pi} n_1 A_{10} \phi(\nu) \tag{4.28}$$

Similarly, we can obtain the absorption coefficient.

$$\alpha_\nu = \frac{h\nu}{4\pi} n_0 B_{01} \phi(\nu) \tag{4.29}$$

Note that we do not include the stimulated emission in eq.(4.28). We have to take it into account. It is convenient to treat stimulated emission as a negative absorption. Thus, the absorption coefficient is modified by including the effect of stimulated emission as follows;

$$\alpha_\nu = \frac{h\nu}{4\pi} \phi(\nu)(n_0 B_{01} - n_1 B_{10}) \tag{4.30}$$

Consequently, we can rewrite the radiative transfer equation eq.(4.1) with eq.(4.28) and eq.(4.30);

$$dI_\nu = \frac{h\nu}{4\pi}A_{10}n_1\phi(\nu)ds - \frac{I_\nu}{4\pi}(n_0B_{01} - n_1B_{10})h\nu\phi(\nu)ds \tag{4.31}$$

The first term expresses the spontaneous emission from the triplet to the singlet. The second term expresses the excitation from the singlet to the triplet by absorbing CMB photons and stimulated emission as negative absorption.

The absorption coefficient eq.(4.30) can be rewritten by using eq.(4.7), eq.(4.10) and eq.(4.11);

$$\begin{aligned}
\alpha_\nu &= \frac{n_0}{4\pi}\left[B_{01} - 3\exp\left(-\frac{T_*}{T_{\rm S}}\right)\right]h\nu\cdot\phi(\nu) \\
&= \frac{3n_0B_{10}}{4\pi}\left[1-\exp\left(-\frac{T_*}{T_{\rm S}}\right)\right]h\nu\cdot\phi(\nu) \\
&= \frac{3c^2A_{10}}{8\pi\nu_{21}^2}\left[1-\exp\left(-\frac{T_*}{T_{\rm S}}\right)\right]n_0\cdot\phi(\nu)
\end{aligned} \tag{4.32}$$

The optical depth is defined by $d\tau_\nu \equiv \alpha_\nu ds$,

$$\tau_\nu = \frac{3c^2A_{10}}{8\pi\nu_{21}^2}\int ds\left[1-\exp\left(-\frac{T_*}{k_{\rm B}T_{\rm S}}\right)\right]n_0\cdot\phi(\nu) \tag{4.33}$$

Remember that the ratio between the singlet and triplet states is 1:3, n_0 becomes $n_{\rm HI}/4$, where $n_{\rm HI}$ is the number density of neutral hydrogen atoms. With these conditions, we can obtain optical depth as follows;

$$\tau_\nu = \frac{3c^2A_{10}}{32\pi\nu_{21}^2}\int ds\left[1-\exp\left(-\frac{T_*}{T_{\rm S}}\right)\right]n_{\rm HI}\cdot\phi(\nu) \tag{4.34}$$

$$\sim \frac{3c^2A_{10}}{32\pi\nu_{21}^2}\left(\frac{h\nu_{21}}{k_BT_{\rm S}}\right)N_{\rm HI}\phi(\nu) \tag{4.35}$$

Here, we used the $T_* \ll T_{\rm S}$. $N_{\rm HI}$ is the column density of neutral hydrogen atoms, $N_{\rm HI} = n_{\rm HI}s = x_{\rm HI}n_{\rm H}s$. $x_{\rm HI}$ is the fraction of neutral hydrogen atoms. In general, the line profile $\phi(\nu)$ includes the Doppler broadening, natural broadening and thermal broadening. We have to include the Hubble flow as an important effect on line profile of the IGM in the expanding Universe. The velocity broadening of a region s, ΔV, becomes $\Delta V \sim sH(z)$ so that $\phi(\nu) \sim c/[sH(z)\nu_{21}]$.

A more exact calculation yields an expression for the 21 cm optical depth of the IGM [106],

$$\tau_\nu = \frac{3hc^3A_{10}}{32\pi\nu_{21}^2T_{\rm S}}\frac{x_{\rm HI}n_{\rm HI}}{(1+z)(dv_\parallel/dr_\parallel)} \tag{4.36}$$

$$\sim 0.0092(1+\delta_b)(1+z)^{3/2}\frac{x_{\rm HI}}{T_{\rm S}}\left[\frac{H(z)/(1+z)}{dv_\parallel/dr_\parallel}\right] \tag{4.37}$$

Here, $dv_\parallel/dr_\parallel$ is the gradient of the proper velocity along line of sight including both Hubble flow and peculiar velocity of the IGM.

4.4 Brightness temperature

In this section, we derive the brightness temperature which is contrast between high-z clouds and the CMB. We regard the CMB temperature as radio background. In this case, T_R in eq.(4.6) becomes CMB temperature T_γ. Then, the brightness temperature for the 21 cm line is given by

$$\begin{aligned} \delta T_{\rm b}^{'}(\nu) &= T_{\rm b} - T_\gamma(z) && (4.38)\\ &= T_{\rm S}(1-\exp(-\tau_\nu)) + T_\gamma \exp(-\tau_\nu) - T_\gamma(z) && (4.39)\\ &= (T_{\rm S} - T_\gamma(z))[1-\exp(-\tau_\nu)] && (4.40) \end{aligned}$$

Here, $\delta T_{\rm b}^{'}(\nu)$ is measured in the rest frame of the gas cloud. Considering expansion of the Universe, the brightness temperature is given by

$$\begin{aligned} \delta T_{\rm b} &= \frac{\delta T_{\rm b}^{'}}{1+z}\\ &= \frac{(T_{\rm S} - T_\gamma(z))}{1+z}[1-\exp(-\tau_\nu)]\\ &\sim \frac{(T_{\rm S} - T_\gamma(z))}{1+z}\tau_\nu\\ &\sim 27 x_{\rm HI}(1+\delta_{\rm b})\left(1-\frac{T_\gamma(z)}{T_{\rm S}}\right)\left[\frac{H(z)/(1+z)}{dv_\parallel/dr_\parallel}\right]\left(\frac{1+z}{10}\frac{0.15}{\Omega_{\rm m}h^2}\right)^{1/2}\left(\frac{\Omega_{\rm b}h^2}{0.023}\right){\rm mK} \end{aligned} \quad (4.41)$$

In the second line, we used that the optical depth to the hyperfine transition is sufficiently small and substituted eq.(4.37) into eq.(4.41) in third line.

Note that δT_b saturates if $T_{\rm S} \gg T_\gamma$ and does not depend on the CMB temperature. Meanwhile, δT_b becomes negative if $T_{\rm S} < T_\gamma$. In the case of $\delta T_b > 0$, we observe the brightness temperature as a emission line for the CMB temperature. Conversely, we observe it as an absorption line for the CMB temperature if $\delta T_b < 0$. The brightness temperature depends on the fraction of neutral hydrogen, matter over-density, gradient of the proper velocity along line of sight and the spin temperature. The spin temperature is key quantity in the brightness temperature because it controls whether the brightness temperature becomes positive or negative. Although we saw the coupling coefficient of the spin temperature in section 4.2, we did not focus on the evolution of the spin temperature and of the neutral fraction. Thus, we investigate the evolution of the spin temperature and components which consist of the spin temperature, the kinetic temperature and the color temperature, to study the thermal history of the IGM. We also follow the global evolution of the ionization fraction in following sections.

4.5 Thermal and ionization history

As shown in previous section, the brightness temperature consists of the spin temperature, neutral hydrogen fraction and other cosmological values. Both spin temperature and neutral hydrogen fraction includes astrophysical information. We can extract these information

via the brightness temperature. In order to obtain the information via the brightness temperature, we need to know the behavior of the brightness temperature. Since the spin temperature and neutral hydrogen fraction play an important role on the brightness temperature, we need to know the behavior of them. The spin temperature consists of the kinetic temperature, the color temperature($T_{\rm C} \sim T_{\rm K}$) and the CMB temperature. Thus, we have to follow the evolution of the kinetic temperature and the CMB temperature. In this section, we introduce basic equations which govern both thermal and ionization histories.

First, we introduce a basic equation to govern the evolution of ionizing fraction $x_e(= 1 - x_{\rm HI})$. The evolution of ionized fraction is determined by the balance between the ionization and the recombination as follows:

$$\frac{dx_e(\mathbf{x}, z^{'})}{dz'} = \frac{dt}{dz'}\left[\Lambda_{\rm ion} - \alpha_{\rm A} C x_e^2 n_b f_{\rm H}\right] \ , \tag{4.42}$$

Λ_{ion} is an ionization rate per baryon, $\alpha_A \sim 4.2 \times 10^{-13}\ ({\rm T_K}/10^4{\rm K})^{-0.7}[{\rm cm^3 s^{-1}}]$ is a case-A recombination coefficient[95]. Here, the case-A recombination is that recombinations to the grand state occur directly. $C \equiv \langle n^2\rangle/\langle n\rangle^2$ is a clumping factor. $f_{\rm H}$ is the number of hydrogen atoms.

Next, we write down a basic equation to describe the evolution of the kinetic temperature $T_{\rm K}$. In order to calculate the evolution of the kinetic temperature, we must keep track of the inhomogeneous heating history of the IGM gas. The evolution of the kinetic temperature can be determined by an application of the first law of thermodynamics $dE = -pdV + dQ$ as follows:

$$\frac{dT_{\rm K}(\mathbf{x}, z^{'})}{dz^{'}} = \frac{2}{3k_{\rm B}(1+x_e)}\frac{dt}{dz^{'}}\sum \epsilon_p + \frac{2T_{\rm K}}{3n_b}\frac{dn_b}{dz^{'}} - \frac{T_{\rm K}}{1+x_e}\frac{dx_e}{dz^{'}}, \tag{4.43}$$

where $n_b = \bar{n}_{b,0}(1+z^{'})^3[1+\delta_{nl}(\mathbf{x}, z^{'})]$ is the total baryonic number density at $(\mathbf{x}, z^{'})$. $\epsilon_p(\mathbf{x}, z^{'})$ is the heating rate [erg$\cdot$s^{-1}] per baryon for certain process p. It is worth noting that we have to distinguish between z which we focus on and some arbitrary higher redshift $z^{'}$.

We show the evolution of the spin temperature and the kinetic temperature in Fig.4.5. We also show redshift evolution of the brightness temperature in Fig.4.6. We summarize physical pictures of the spin temperature and the brightness temperature as follows:

(i) **Collisional coupling**: $T_{\rm K} = T_{\rm S} < T_\gamma$

At high redshift, the IGM is dense, so the spin temperature couples the gas kinetic temperature by collisions. The gas temperature originally couples the CMB. After decoupling from the CMB, the gas cools adiabatically as $(1+z)^{-2}$, faster than the CMB temperature.

(ii)**Collisional decoupling**: $T_{\rm K} < T_{\rm S} < T_\gamma$

Even after the CMB temperature decouples from the kinetic temperature, the spin temperature keeps coupling to the kinetic temperature. However, as the Universe evolves, this coupling between the spin temperature and the kinetic temperature becomes weaker due to diffusion of the IGM which is caused by decrease of the collision rate by the expanding Universe. As the result, the spin temperature approaches the CMB temperature, and then

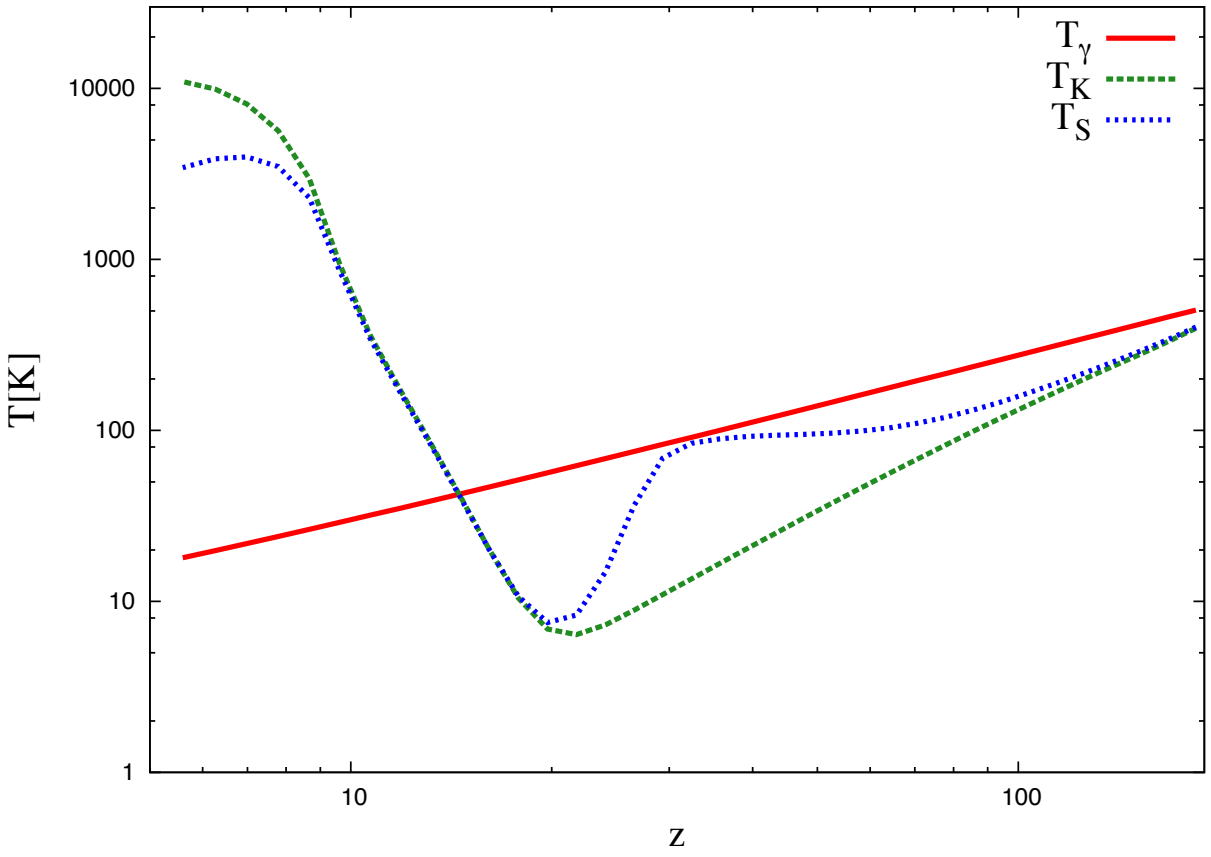

Figure 4.5: Thermal history for each temperature including Compton heating, the X-ray heating and the Lyα background. The CMB temperature (solid line), the spin temperature (dotted line) and the kinetic temperature(dashed line).

the spin temperature couples the CMB temperature.

(*iii*) **WF coupling**; $T_{\rm K} < T_{\rm S} < T_\gamma$

After first luminous objects form, the spin temperature of the gas couples the kinetic temperature strongly via the WF effect at $z \lesssim 30$. Since the Lyα coupling is more modest than heating the gas, the kinetic temperature keeps to decrease at this epoch. The brightness temperature becomes negative ($\delta T_b < 0$) because the spin temperature is lower than the CMB temperature. Therefore, we observe the brightness temperature as an absorption line at this epoch.

(*iv*) **X-ray heating**; $T_{\rm K} = T_{\rm S} < T_\gamma \longrightarrow T_{\rm K} = T_{\rm S} > T_\gamma$

Since the spin temperature couples the kinetic temperature strongly via the WF effect, the spin temperature evolves with the kinetic temperature. Once the spin temperature reaches minimum value, it starts to increase because of the X-ray heating at $z \sim 20$. As the X-ray heating proceeds sufficiently, the spin temperature becomes higher than the CMB temperature. Thus, the global brightness temperature changes its sign from $\delta T_b < 0$ to $\delta T_b > 0$. We can observe the brightness temperature as emission lines.

(*v*) **Reionization**; $T_{\rm K} = T_{\rm S} \gg T_\gamma$

After the X-ray heating proceeds sufficiently, the 21 cm signal is insensitive to the spin temperature because the brightness temperature is saturated when $T_{\rm S} \gg T_\gamma$ is satisfied. In this case, the brightness temperature is mainly controlled by neutral hydrogen fraction. As HII regions grow, the 21 cm signal decreases because the neutral hydrogen fraction becomes small and finally become zero shown in Fig.4.7. In Fig.4.7, we show the global evolution of ionization fraction (and neutral hydrogen fraction). When neutral hydrogen fraction becomes zero, the brightness temperature also becomes zero. Consequently, we cannot observe the brightness temperature.

4.6 21cmFAST

In our calculation for the spin temperature, the brightness temperature and ionization history, we use 21cmFAST which is a public code[88]. This code is based on a semi-numerical model of heating and reionization, and makes maps of matter density, velocity, the spin temperature, neutral fraction and the brightness temperature at the designated redshifts. In order to calculate the brightness temperature, we have to calculate ionization field $x_{\rm HII}$, the kinetic temperature $T_{\rm K}$ and Lyα background J_α (see sec 4.2-4.4). In this section, we introduce the method to calculate these values in the 21cmFAST.

4.6.1 Ionization field

Here, we introduce a prescription to calculate ionization field used in 21cmFAST. First, we describe the evolved density field. We generate same density and velocity initial conditions

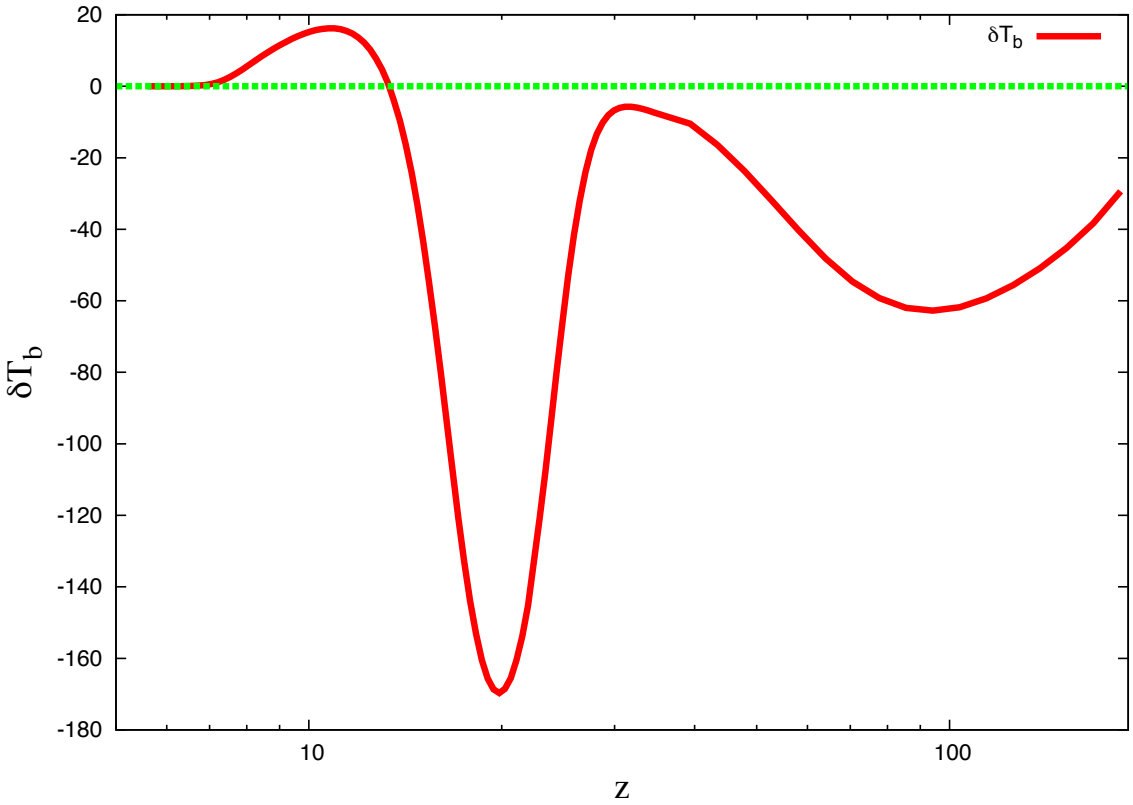

Figure 4.6: Time evolution of the brightness temperature. When the WF effect becomes effective, the brightness temperature makes a deep trough at $z \sim 20$. Thus we observe the brightness temperature as absorption lines against the CMB temperature. Once the X-ray heating proceeds sufficiently, the spin temperature becomes higher than the CMB temperature. Thus, we observe the brightness temperature as emission lines at $z \lesssim 13$. After this, the brightness temperature decreases due to the reionization and finally becomes zero when all hydrogen atoms are ionized.

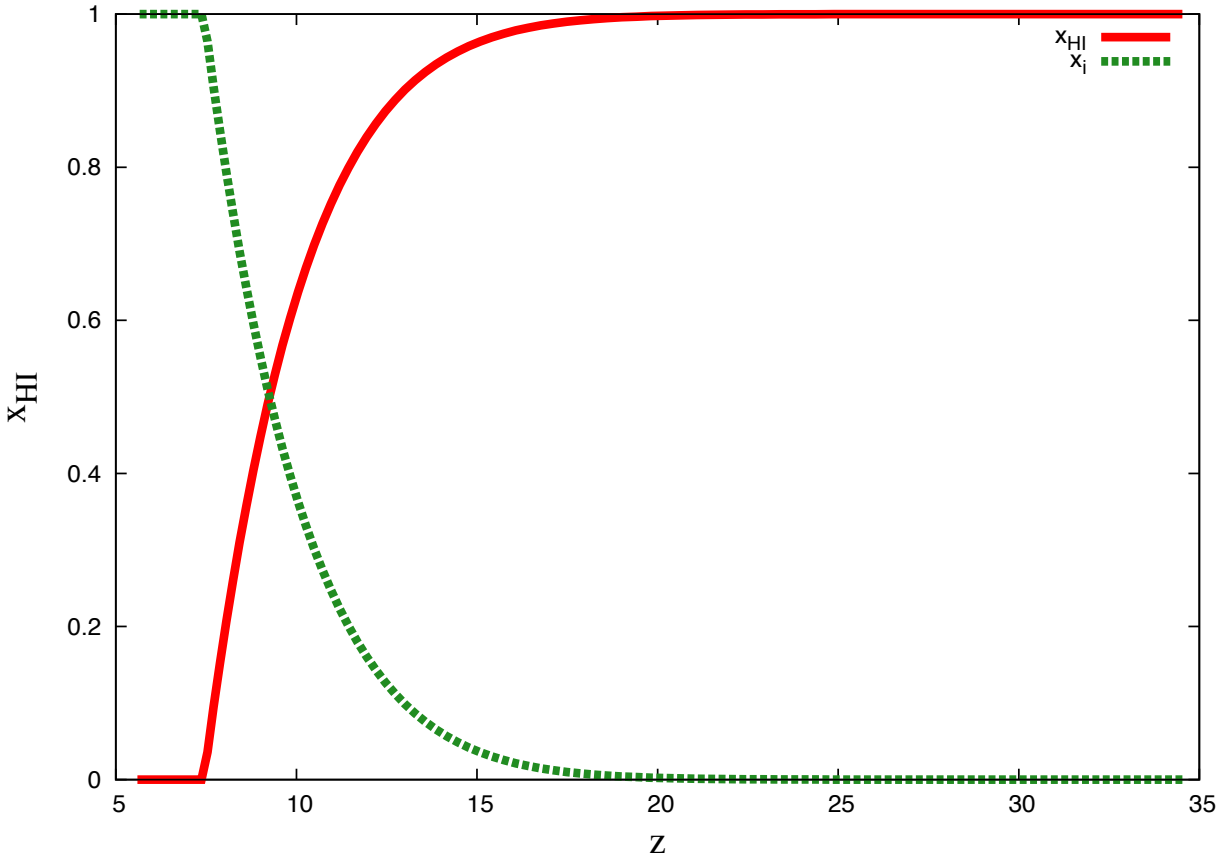

Figure 4.7: Time evolution of mean neutral hydrogen fraction $x_{\rm HI}$ (*solid line*) and ionization fraction $x_i (= 1 - x_{\rm HI})$ (*dashed line*).

with [127]. We then approximate gravitational collapse by moving each initial matter particle according to the Zel'dovich approximation(see sec 2.3.3). This approximation is computationally convenient because the displacement of particle is separable between spatial and time components. Consequently, we need to calculate spatial component only once for each simulation box. In 21cmFAST, we do not separate baryons and dark matter particles. Note that 21cmFAST does not resolve source halos. However, the power spectrum of density field obtained by 21cmFAST with the Zel'dovich approximation agrees with that obtained by numerical simulations at $k \lesssim 5\mathrm{Mpc}^{-1}$.

Next, we introduce a prescription for calculating ionization field. We use excursion-set approach to identify HII regions as discussed in sec 3.3.3. Again we briefly describe foundation of this approach here. The foundation of this approach requires that the number of ionizing photons inside a region should be larger than that of neutral hydrogen atoms. The radius R in the region starts from large one($R_{\rm max}$) and progresses to smaller one. Then, we flag fully ionized region if we meet the criteria $f_{\rm coll}(\mathbf{x}, z, R) \geq \zeta^{-1}$, where ζ is the ionizing efficiency parameter and $f_{\rm coll}$ is the collapse fraction smoothed on scale R based on the extended Press-Schechter theory(see sec2.5). This criteria is equivalent to eq.(3.28). If this criteria is not satisfied even if the radius reaches cell size $R_{\rm cell}$, we allow the regions to be partially ionized with ionization fraction $\zeta f_{\rm coll}(\mathbf{x}, z, R_{\rm cell})$. Here, $R_{\rm max}$ is a free parameter we can choose.

4.6.2 Kinetic temperature

In 21cmFAST, we have to solve eqs.(4.42) and (4.43) to follow the evolution of the kinetic temperature and local ionization fraction in the *neutral* IGM (i.e. outside of the ionized region discussed in 4.6.1.)

To speed up calculation, we use a following assumption. In the context of the linear perturbation theory, we can describe the density perturbation with the linear growth factor $D(z)$ such as $\delta_{nl}(\mathbf{x}, z^{'}) \approx \delta_{nl}(\mathbf{x}, z)D(z')/D(z)$. In general, we should follow the nonlinear evolution of each density fluctuation. However, the regime at very high redshift when the heating is important is expected to evolve with the linear or quasi-linear structure formation. Therefore, we assume that the density fluctuations can be described by the linear growth factor. Then eq.(4.43) and eq.(4.42) are re-written by

$$\frac{dx_e(\mathbf{x}, z^{'})}{dz'} = \frac{dt}{dz'}\Lambda_{\rm ion} - \frac{dt}{dz'}\alpha_{\rm A} C x_e^2 f_{\rm H}\bar{n}_{b,0}(1+z')^3\left[1+\delta_{nl}(\mathbf{x}, z^{'})\frac{D(z')}{D(z)}\right] , \tag{4.44}$$

$$\frac{dT_{\rm K}(\mathbf{x}, z^{'})}{dz'} = \frac{2}{3k_B(1+x_e)}\frac{dt}{dz'}\sum_p \epsilon_p + \frac{2T_{\rm K}}{1+z'} + \frac{2T_{\rm K}}{3}\frac{dD(z')/dz'}{D(z)/\delta_{nl}(\mathbf{x}, z^{'}) + D(z')} - \frac{T_{\rm K}}{1+x_e}\frac{dx_e}{dz'} . \tag{4.45}$$

The first term of eq.(4.45) is the energy injection through the heating process p (which includes X-ray photons and the heating via the Compton scattering of the CMB), the second term is due to the Hubble expansion, the third term corresponds to the adiabatic heating and cooling from the structure formation. The last term comes from ionization.

Next let us consider the each energy injection process.

Compton heating

At very high redshift, the CMB photons couple residual free electrons via the Compton scattering. As the result, $T_\gamma \sim T_{\rm K}$ is realized. However, the gas decouples from CMB photons according to the expansion of the Universe. After the decoupling, the gas evolves adiabatically such as $T_{\rm K}(z') = 2.73 \times (1+z_{\rm dec})[(1+z')/(1+z_{\rm dec})]^2$, where the decoupling redshift is approximately given by $z_{\rm dec} \approx 137(\Omega_b h^2/0.022)^{0.4} - 1$. In this case, the Compton heating contributes to eq.(4.45) in the form of

$$\frac{2}{3k_B(1+x_e)}\epsilon_{\rm comp} = \frac{x_e}{1+f_{\rm He}+x_e}\frac{8\sigma_{\rm T}u_\gamma}{3m_e c}(T_\gamma - T_{\rm K}) \ , \tag{4.46}$$

Here, u_γ is the energy density of the CMB, which is in proportion to T_γ^4, $f_{\rm He}$ is the number fraction of helium and $\sigma_{\rm T}$ is the Thomson cross-section given by

$$t_\gamma \equiv \frac{3m_{\rm e}c}{8\sigma_{\rm T}u_\gamma} \tag{4.47}$$

In the situation that there is no heating sources, the kinetic temperature evolves adiabatically in proportion to $(1+z)^2$.

X-ray heating

The most effective heating process to inject energy into IGM is X-ray heating[130, 18, 104, 146]. We expect that the star burst galaxies, SN remnant, mini-quasar and X-ray binary are candidates for the X-ray source. Since X-ray photon has the long mean free path, it is able to heat the IGM far from sources. The comoving mean free path of X-ray photon $\lambda_{\rm X}$ with energy E is given by [43]

$$\begin{aligned} E &\sim 2\left(\frac{1+z}{15}\right)^{1/2}\bar{x}_{\rm HI}^{1/3}{\rm keV} \\ \lambda_{\rm X} &\sim 4.9\bar{x}_{\rm HI}^{-1/3}\left(\frac{1+z}{15}\right)^{-2}\left(\frac{E}{300{\rm eV}}\right)^3{\rm Mpc}. \end{aligned} \tag{4.48}$$

Let us estimate the X-ray heating rate per particle by summing up contributions from X-ray sources which are located in a spheric shell around $(\mathbf{x}, z^{'})$. First, we assume that the number of sources emitting X-ray photons is in proportion to the collapsed fraction, f_{coll}. Under this assumption, the total X-ray emission rate per redshift interval from luminous sources located between $z^{''}$ and $z''+dz^{''}$ where $(z^{''} \geq z^{'})$ can be given by

$$\frac{d\dot{N}}{dz''} = \zeta_X f_* \Omega_b \rho_{\rm crit,0}(1+\delta_{\rm nl}^{R''})\frac{dV}{dz''}\frac{df_{\rm coll}}{dt} \ , \tag{4.49}$$

where $\zeta_{\rm X}$ is the X-ray heating efficiency, which gives the number of photons per solar mass in stars. Other remaining terms on RHS correspond to the star formation rate inside the spherical shell. f_* is the fraction of baryons converted to stars and $dV^{'}$ is the comoving volume element at $z^{''}$. The collapsed fraction f_{coll} is given by [6, 8] as

$$f_{\rm coll}(\mathbf{x}, z'', R'', S_{\rm min}) = \frac{\bar{f}_{\rm ST}}{\bar{f}_{\rm PS,nl}} {\rm erfc}\left[\frac{\delta_c - \delta_{nl}^{R''}}{\sqrt{2[S_{\rm min} - S^{R''}]}}\right] \ , \tag{4.50}$$

where $R^{''}$ is the comoving, null geodesic distance between $z^{'}$ and $z^{''}$, S_{min} and $S^{R^{''}}$ are the mass variance which corresponds to smallest halo mass scale and scale $R^{''}$, respectively. $\delta_{nl}^{R^{''}}$ is over density smoothed on $R^{''}$. $\bar{f}_{\rm ST}$ and $\bar{f}_{\rm PS,nl}$ are the mean collapsed fraction obtained by the Sheth-Tormen(ST) theory and the Press-Schecther(PS) theory respectively. Thus, $\frac{\bar{f}_{\rm ST}}{\bar{f}_{\rm PS,nl}}$ is a normalization factor to match the collapse fraction obtained by the PS theory to the ST theory, which is based on N-body simulation while the PS theory gives an analytic formula.

Next, we consider the arrival rate of X-ray photon with an assumption that the X-ray luminosity of sources is characterized with a power-law form, $L_e \propto (\nu/\nu_0)^{-\alpha}$. $h\nu_0$ is the pivot energy giving lowest energy of X-ray photon escaping into the IGM. Then, we can write the arrival rate of X-ray photon with frequency ν from sources located at between $z^{''}$ and $z^{''} + dz^{''}$ (the number of photons in [s$^{-1}\cdot$ Hz^{-1} at $(\mathbf{x}, z^{'})$]) as

$$\frac{d\phi_{\rm X}(\mathbf{x}, \nu, z', z'')}{dz''} = \frac{d\dot{N}_{\rm X}}{dz''} \alpha \nu_0^{-1} \left(\frac{\nu}{\nu_0}\right)^{-\alpha-1} \left(\frac{1+z''}{1+z'}\right)^{-\alpha-1} {\rm e}^{-\tau_{\rm X}} \ , \tag{4.51}$$

The last term expresses the IGM attenuation and the optical depth for X-ray photons $\tau_{\rm X}$ is

$$\tau_{\rm X}(\nu, z', z'') = \int_{z''}^{z'} d\hat{z} \frac{cdt}{d\hat{z}} \hat{x}_{\rm HI} f(\hat{z}) \bar{n}(\hat{z}) \tilde{\sigma}(z', \hat{\nu}) \ , \tag{4.52}$$

where $\tilde{\sigma}(z', \hat{\nu})$ is the photo-ionization cross section weighted over species, $\tilde{\sigma}(z', \hat{\nu}) \equiv f_{\rm H}(1 - \bar{x}_e)\sigma_{\rm H} + f_{\rm He}(1-\bar{x}_e)\sigma_{\rm HeI} + f_{\rm He}\bar{x}_e\sigma_{\rm HeII}$. This cross section is evaluated at $\hat{\nu} = \nu(1+\hat{z})/(1+z')$ and $\hat{x}_{HI}$ is a volume filling factor of neutral region. In practice, the abundance of HeII is neglected.

By using eq.(4.51) and eq.(4.52), we can finally obtain the X-ray heating rate per baryon ϵ_X by integrating over frequency and redshift as follows;

$$\begin{aligned} \epsilon_{\rm X}(\mathbf{x}, z^{'}) = & \int_{\nu_0}^{\infty} d\nu \sum_i (h\nu - E_i^{\rm th}) f_{\rm heat} f_i x_i \sigma_i \\ & \int_{z'}^{\infty} dz'' \frac{d\phi_{\rm X}/dz''}{4\pi r_p^2} \ , \end{aligned} \tag{4.53}$$

where, r_p is null geodesic separation between $z^{'}$ and $z^{''}$ and the frequency integral considers the sum over species i=HI,HeI and HeII. f_i is the number fraction of species i. The factor f_{heat} is defined as the fraction of the electron energy, $h\nu - E_i^{th}$, which is deposited as heating. The energy E_{th} is deposited into the ionization and excitation.

Roughly, we can estimate the energy injection via X-ray heating as follows:

$$\frac{2}{3} \frac{\epsilon_X}{k_{\rm B}(1+x_e)H(z)} \sim 10^3 f_X \left(\frac{f_*}{0.1}\frac{f_{X,h}}{0.2}\frac{df_{\rm coll}/dz}{0.01}\frac{1+z}{10}\right) [{\rm K}] \tag{4.54}$$

By analogy with eq.(4.53), we can also estimate the ionization rate per particle as

$$\Lambda_{\rm ion}(\mathbf{x},z) = \int_{\nu_0}^{\infty} d\nu \sum_i f_i x_i \sigma_i F_i \int_{z'}^{\infty} dz'' \frac{d\phi_{\rm X}/dz''}{4\pi r_p^2} \ , \tag{4.55}$$

$$F_i = \left(h\nu - E_i^{\rm th}\right)\left(\frac{f_{\rm ion,HI}}{E_{\rm HI}^{\rm th}} + \frac{f_{\rm ion,HeI}}{E_{\rm HeI}^{\rm th}} + \frac{f_{\rm ion,HeII}}{E_{\rm HeII}^{\rm th}}\right) + 1,$$

where $f_{ion,j}$, is the fraction of the electron energy used as secondary ionizations of species j.

Here we refer to Lyα heating. Although Lyα photons have enough energy to change spin flip state, the energy which injects into the IGM as heat through the scattering is sufficiently small compared with X-ray photons. Therefore, the heating by Lyα photons are negligible. The heating rate by Lyα photons are roughly estimated by

$$\frac{2}{3}\frac{\epsilon_\alpha}{k_{\rm B}(1+x_e)H(z)} \sim \frac{0.80}{T_{\rm K}}\frac{x_\alpha}{S_\alpha}\left(\frac{10}{1+z}\right). \tag{4.56}$$

Comparing eq.(4.56) with eq.(4.54), you can find that the X-ray heating rate is third or fourth order of magnitude larger than the Lyα heating rate.

4.6.3 Lyman-α background

Next, we consider the Lyα background which has two contributors. The first one is X-ray excitation of HI expressed by $J_{\alpha,X}$. In this process, Lyα photons are produced via a cascade with the rate at which photons redshifting out of the Lyα resonance[19]. This can be easily related to the X-ray heating rate as similar as eq.(4.53),

$$J_{\alpha,{\rm X}}(\mathbf{x},z) = \frac{cn_b}{4\pi H(z)\nu_\alpha}\int_{z'}^{\infty} dz'' \frac{d\phi_{\rm X}/dz''}{4\pi r_p^2} \int_{{\rm Max}[\nu_0,\nu_{\tau=1}]}^{\infty} d\nu \sum_i (h\nu - E_i^{\rm th})\frac{f_{\rm Ly\alpha}}{h\nu_\alpha} f_i x_i \sigma_i \ , \tag{4.57}$$

Here, $f_{Ly\alpha}$ is the fraction of the electron energy deposited into Lyα photons.

The another contributor of Lyα photons is direct star emission $J_{\alpha,*}$. In this case, Ly-n series photons from star cascade passing through the Lyα photons with a recycle fraction $f_{recycle}$[105]. Typically the maximum of n is $n_{max} \sim 23$. The Lyα background from direct stellar emission can be estimated analogously to the X-ray luminosity such as

$$\begin{aligned} J_{\alpha,*}(\mathbf{x},z) &= \sum_{n=2}^{n_{\rm max}} J_\alpha(n,\mathbf{x},z) \\ &= \sum_{n=2}^{n_{\rm max}} f_{\rm recycle}(n) \int_z^{z_{\rm max}(n)} dz' \frac{1}{4\pi}\frac{d\phi_*^e(\nu_n',\mathbf{x})/dz'}{4\pi r_p^2} \end{aligned} \tag{4.58}$$

Here,

$$\frac{d\phi_*^e(\nu_n', \mathbf{x})}{dz'} = \varepsilon(\nu_n') f_* \bar{n}_{\rm b,0} (1 + \bar{\delta}_{\rm nl}^{R''}) \frac{dV}{dz'} \frac{df_{\rm coll}}{dt} \ , \tag{4.59}$$

which expresses the arrival rate of stellar emission and $\epsilon(\nu)$ is the number of photons produced by stars [in Hz^{-1} per stellar baryon]. We use PopII and PopIII spectral models for $\epsilon(\nu)$ [7].

The total Lyα background is simply expressed as the sum of above components;

$$J_{\alpha,tot}(\mathbf{x}, z) = J_{\alpha,X}(\mathbf{x}, z) + J_{\alpha,*}(\mathbf{x}, z) \tag{4.60}$$

This total Lyα background affects the spin temperature through the contribution to the WF effect via the coupling coefficient eq.(4.26).

Chapter 5

21 cm power spectrum & one-point statistics

As we referred previously, the redshifted 21 cm line signal from neutral hydrogens is a promising tool to probe the Cosmic Dawn and the EoR. In particular, we often use the 21 cm power spectrum to extract information on the IGM through the Cosmic Dawn to the EoR. In this chapter, we introduce the 21 cm power spectrum and its time evolution. In addition, we give a physical interpretation of the time evolution of the power spectrum of the 21 cm brightness temperature fluctuations, which can be decomposed into dark matter density, the spin temperature and neutral fraction of hydrogen fluctuations. Further, we introduce the one-point statistics of the fluctuations, such as variance and skewness, as complement to the 21 cm power spectrum and study their properties. This chapter is based on [118].

5.1 Introduction

In this chapter, we analyze the 21 cm fluctuations based on the 21 cm power spectrum and one-point statistics. We investigate what we can learn from the signal by using a public code called 21 cmFAST [87, 88]. This code is based on a semi-analytic model of star/galaxy formation and reionization described by previous chapters. First, in order to find how physical processes are related to the observed 21 cm signal, we decompose the 21 cm power spectrum into three components composed by fluctuations of the matter density field, those of the neutral fraction and those of the spin temperature, and discuss the redshift evolution of the power spectrum.

Next, we further focus on the distributions, variance and skewness of the brightness temperature and three decomposed components, in order to understand the physical meaning of the behavior of the 21 cm power spectrum more deeply. Although there are several studies which discuss the one-point statistics of the brightness temperature [55, 134], most of such works have focused on the signal from the EoR, that is, $z \lesssim 10$, to investigate its dependence on the reionization process, and for the signal from $z \gtrsim 15$ the one-point statistics are not sufficiently discussed.

This chapter is organized as follows. In section 2, first we show the 21 cm power spectrum and the decomposition of it into each component and discuss the redshift dependence

of the power spectrum. In section 3, we investigate distribution and one-point statistics such as variance and skewness of the spin temperature which is a dominant component of the 21 cm power spectrum at higher redshift ($z \gtrsim 15$), and also we investigate its dependence on the X-ray heating efficiency. In section 4, based on the discussion about the one-point statistics of the spin temperature given in section 3, we investigate the one-point statistics of the observed brightness temperature. In section 5, we give a summary and conclusion.

Unless stated otherwise, we quote all quantities in comoving units. We employ the best fit values of the standard the cosmological parameters obtained in [70].

5.2 21 cm power spectrum

In this section, we introduce the 21 cm power spectrum and its decomposition into spectra of the matter density field, the neutral fraction and the spin temperature. In particular, we focus on the redshift evolution of the power spectra.

First, we define the 21 cm power spectrum, that is, the power spectrum of the brightness temperature fluctuations;

$$\langle \delta_{21}(\mathbf{k})\delta_{21}(\mathbf{k}^{'})\rangle = (2\pi)^3\delta(\mathbf{k}+\mathbf{k}^{'})P_{21}(\mathbf{k}), \tag{5.1}$$

where $\delta_{21}(\mathbf{k}) \equiv \delta T_b(\mathbf{k}) - \langle \delta T_b\rangle$ and $\langle \delta T_b\rangle$ is the mean brightness temperature obtained by the brightness temperature map. As we saw in Eq. (4.40), the fluctuations in the brightness temperature are contributed not only from the matte density field, but also from the fluctuations of the spin temperature and neutral fraction, aside from the gradient of peculiar velocity which we neglect here. We can rewrite Eq. (4.40) as,

$$\delta T_b(\mathbf{x}) = \overline{\delta T}_b(1+\delta_{x_{\rm H}}(\mathbf{x}))(1+\delta_m(\mathbf{x}))(1+\delta_\eta(\mathbf{x})), \tag{5.2}$$

where $\delta_{\rm H}$ and δ_η are defined by $x_{\rm H} = \overline{x}_{\rm H}(1+\delta_{\rm H})$ and $\eta = \overline{\eta}(1+\delta_\eta)$ with $\eta = 1 - T_\gamma/T_{\rm S}$. $\overline{x}_{\rm H}, \overline{\eta}$ are volume average of $x_{\rm H}, \eta$ and $\overline{\delta T_b}$ is the average brightness temperature evaluated as,

$$\overline{\delta T_b} = 27\overline{x_{\rm H}\eta}\left(\frac{1+z}{10}\right)^{1/2}\left(\frac{0.15}{\Omega_m h^2}\right)^{1/2}\left(\frac{\Omega_b h^2}{0.023}\right), \tag{5.3}$$

Here we characterize the contribution of the spin temperature T_s by a new variable $\eta = 1 - T_\gamma/T_{\rm S}$ [118]. By using this parameter, we can take into account a nonlinear relation between the spin and brightness temperatures linearly. The volume average of η is represented by $\overline{\eta}$. Note that when $\delta_{T_{\rm S}} \ll 1$, we have,

$$\delta_\eta \simeq \frac{T_\gamma/\bar{T}_{\rm S}}{1 - T_\gamma/\bar{T}_{\rm S}}\delta_{T_{\rm S}}. \tag{5.4}$$

and the power spectra of $\delta_m, \delta_{\rm H}$ and δ_η as,

$$\langle \delta_m(\mathbf{k})\delta_m(\mathbf{k}^{'})\rangle = (2\pi)^3\delta(\mathbf{k}+\mathbf{k}^{'})P_m(\mathbf{k}), \tag{5.5}$$
$$\langle \delta_{\rm H}(\mathbf{k})\delta_{\rm H}(\mathbf{k}^{'})\rangle = (2\pi)^3\delta(\mathbf{k}+\mathbf{k}^{'})P_{x_{\rm H}}(\mathbf{k}), \tag{5.6}$$
$$\langle \delta_\eta(\mathbf{k})\delta_\eta(\mathbf{k}^{'})\rangle = (2\pi)^3\delta(\mathbf{k}+\mathbf{k}^{'})P_\eta(\mathbf{k}), \tag{5.7}$$

Table 5.1: Resolution at 80 MHz ($z \sim 17$) (Dewdney et al 2013).

telescope	maximum baseline	spacial resolution	angle resolution
LOFAR	$\sim$ 1500 m	$\sim$ 13 Mpc	$\sim$ 4 arcmin
MWA	$\sim$ 750 m	$\sim$ 27 Mpc	$\sim$ 9 arcmin
SKA1	$\sim$ 2000 m	$\sim$ 10 Mpc	$\sim$ 3 arcmin
SKA2	$\sim$ 5000 m	$\sim$ 4 Mpc	$\sim$1 arcmin

The cross correlations such as $P_{x_{\rm H}\eta}$ are defined in a similar way. Then, from Eq.(4.40), we see that the power spectrum of the brightness temperature can be decomposed into a sum of the auto-correlations and cross-correlations:

$$P_{21} = (\overline{\delta T_b})^2[P_m + P_{x_{\rm H}} + P_\eta + P_{x_{\rm H}\eta} + P_{x_{\rm H}m} + P_{m\eta}], \tag{5.8}$$

where,

$$\overline{\delta T_b} = 27\overline{x_{\rm H}}\ \overline{\eta}[(1+z)/10]^{1/2}(0.15/\Omega_m h^2)^{1/2}(\Omega_b h^2/0.023).$$

We neglected higher-order terms and we have checked that the higher-order contributions are at most 30% of the total power spectrum at higher redshifts we are interested in here, and do not affect the qualitative feature of the redshift evolution. Therefore, the contribution can be safely neglected for the purpose of this article. However, for more precise quantitative discussion, such higher-order contributions have to be evaluated precisely. We plan to investigate the higher-order contribution and nonlinearity in the future.

To compute the power spectra, we use a 21 cmFAST [87, 88]. We performed simulations in a $(200{\rm Mpc})^3$ comoving box with 300^3 grids, which corresponds to 0.66 Mpc resolution or $\sim$ 3 arcmin at 80 MHz (z=17) (we show some telescope specifications in table.5.1), from $z = 200$ to $z = 8$ adopting the following parameter set, $(\zeta, \zeta_X, T_{\rm vir}, R_{\rm mfp}) = (31.5, 10^{56}/M_\odot, 10^4\ {\rm K}, 30\ {\rm Mpc})$. Here, ζ is the ionizing efficiency, ζ_X is the number of X-ray photons emitted by source per solar mass, $T_{\rm vir}$ is the minimum virial temperature of halos which produce ionizing photons, and $R_{\rm mfp}$ is the mean free path of ionizing photons through the IGM. In our calculation, we also ignore, for simplicity, the gradient of peculiar velocity whose contribution to the brightness temperature is relatively small (a few %) [47].

In Fig. 5.1, we plot the total and decomposed power spectra, $\Delta_{21} = k^3 P_{21}/2\pi^2$, $\Delta_i = k^3(\overline{\delta T_b})^2 P_i/2\pi^2$ with $i = x_{\rm H}, m$ and η, as functions of redshift for $k = 0.03, 0.13, 1.0\ {\rm Mpc}^{-1}$. We can see several characteristic peaks in the total power spectrum: three peaks for $k = 0.03, 0.13\ {\rm Mpc}^{-1}$ and two peaks for $k = 1.0{\rm Mpc}^{-1}$. These were already found in the previous works and it was suggested that they are, from high-z one to low-z one, induced by the WF effect, the X-ray heating and reionization, respectively [104]. Below we give a more detailed interpretation considering contributions from the fluctuations in neutral fraction, matter density and the spin temperature.

First, the fluctuation in neutral fraction appears when reionization begins but power spectrum, $(\overline{\delta T_b})^2 P_{x_{\rm H}}$, is subdominant at high redshifts ($z \gtrsim 15$). It becomes dominant as reionization proceeds and forms the low-z peak at $z \approx 10$. A dip at $z \approx 14$ corresponds to the redshift when the average spin temperature becomes equal to the CMB temperature so that the average brightness temperature, $\overline{\delta T_b}$, vanishes. This dip is also seen in the contribution of matter fluctuations, which is important at smaller scales.

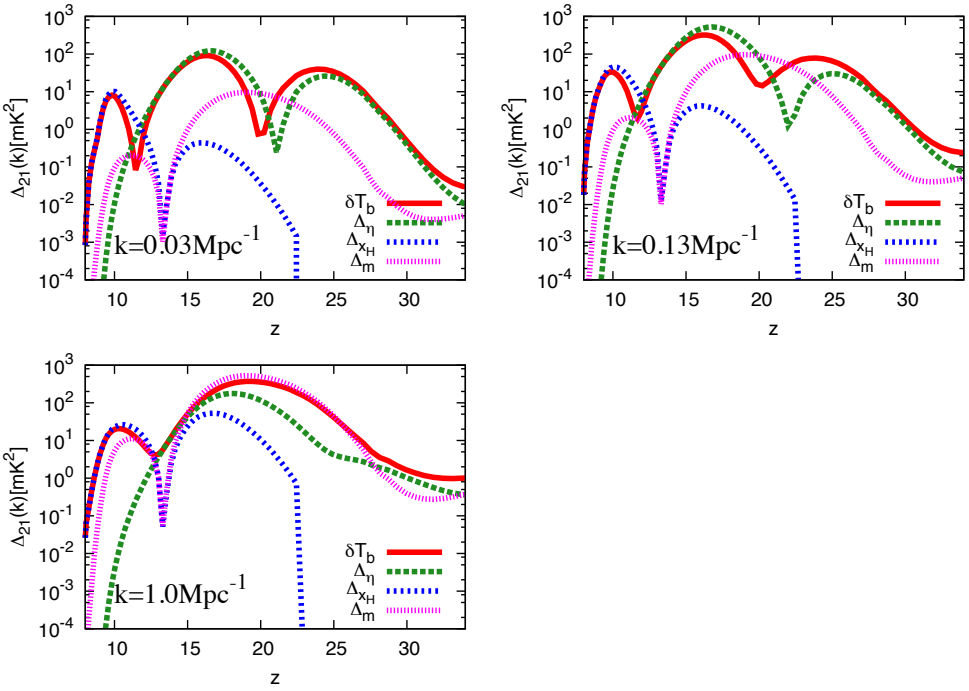

Figure 5.1: Total and decomposed 21 cm power spectra as functions of the redshift for $k = 0.03$ Mpc^{-1} (left top), 0.13 Mpc^{-1} (right top) and 1.0 Mpc^{-1} (left bottom).

On the other hand, the power spectrum contributed from the spin-temperature fluctuations is negligible at low redshifts ($z \lesssim 10$). This is because at these redshifts the spin temperature is much higher than the CMB temperature and the factor $\eta = 1 - T_\gamma/T_{\rm S}$ is almost unity independent of the value of $T_{\rm S}$. The spin-temperature fluctuations are important at higher redshifts ($z \gtrsim 13$) especially at larger scales and this contribution forms the two peaks at $z \approx 16$ and 24. However, there are slight deviations in the peak positions between the brightness temperature and the spin temperature due to the presence of matter fluctuations.

Thus, the low-z peak and the other two peaks are contributed from the neutral fraction and the spin temperature fluctuations, respectively, while the high-z peak at small scales cannot be seen due to the contribution from matter fluctuations. In other words, the evolution of the spin temperature, which reflects the formation rate and properties of the first-generation stars, can be directly probed by measuring the power spectrum of the brightness temperature at $z \gtrsim 15$. In the next section, we focus on the understanding of spin-temperature fluctuations at this epoch considering one-point statistics.

5.3 One-point statistics of the spin temperature

In this section, we study the probability distribution function (PDF) of the spin temperature and one-point statistics such as variance and skewness. In practice, we focus on $\eta = 1 - T_\gamma/T_{\rm S}$, rather than $T_{\rm S}$ itself, because it is linearly related to the brightness temperature. However, because η is a monotonic function of $T_{\rm S}$, physical interpretation

is relatively straightforward. Recently, one-point statistics of the brightness temperature during reionization was investigated assuming $T_{\rm S} \gg T_\gamma$ [8, 55, 134]. This condition is not valid in our context.

Obtained maps of η from 21 cmFAST for the redshifts $z = 28, 25, 22$, and 19 are shown in Fig. 5.2. From these maps, we evaluate the PDF and also the variance and skewness of η. The variance and skewness of a variable X are defined as,

$$\sigma^2 = \frac{1}{N}\sum_{i=1}^{N}\left[X - \overline{X}\right]^2 \tag{5.9}$$

$$\gamma = \frac{1}{N\sigma^3}\sum_{i=1}^{N}\left[X - \overline{X}\right]^3, \tag{5.10}$$

where N is the number of pixels of the maps. Note that the skewness is negative (positive) when the tail of the distribution relatively extends toward low (high) values of X.

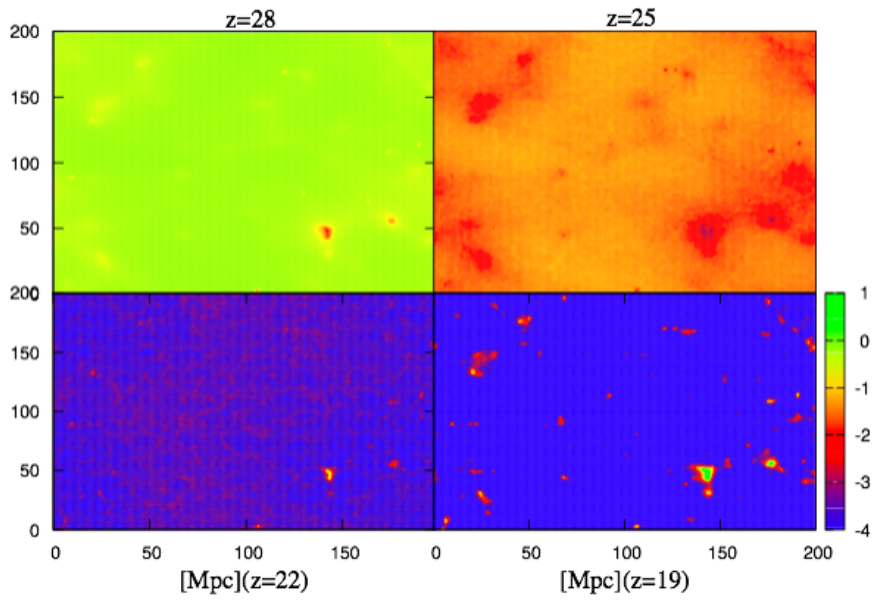

Figure 5.2: The map of $1 - T_\gamma/T_{\rm S}$ at $z = 28$ (left top), 25 (right top), 22 (left bottom), 19 (right bottom). We can see that the spatial averaged value of η decreases from $z = 28$ to 19. A spatial distribution of η can be also seen in each panel.

We plot the PDF of η for $z = 19 - 27$ in Fig.5.3. First of all, the average value of η decreases as redshift decreases because the spin temperature strongly couples the kinetic temperature, which decreases as $(1 + z)^2$ due to the adiabatic cooling of gas, via the WF effect at this epoch. Next, we see the shape of the PDF is also changing and, in particular, the direction of the longer tail changes at $z \approx 23$ (cyan dot-dashed line). This is also confirmed in the top of Fig. 5.4, where we plot the time evolution of the variance and skewness of the PDF. Actually, the sign of the skewness changes at the same redshift from negative to positive. Here it is important to note that the variance has a local minimum at

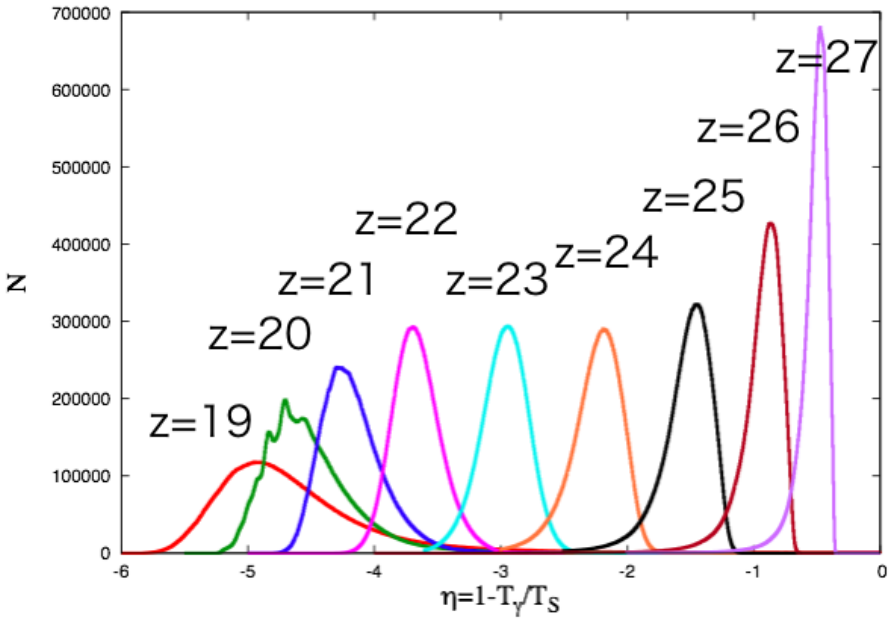

Figure 5.3: PDF of $1 - T_\gamma/T_{\rm S}$ for $z = 19 - 27$ obtained by the map of the spin temperature shown in Fig. 5.2.

almost the same timing. Because the variance is the integration of the power spectrum with respect to the wavenumber, this local minimum corresponds to the dip in the contribution of η in Fig. 5.1.

The above behavior can be understood by considering the X-ray heating of the gas. As we can see in Fig. 5.2, at higher redshifts ($z \gtrsim 25$) the spin temperature in the neighborhood of stars approaches to the kinetic temperature due to the WF effect and becomes lower than the average, and consequently its PDF has a tail toward lower temperature. Then, as the X-ray heating becomes effective, the spin temperature increases in the neighborhood of stars and the tail goes toward higher-value side. At the transition time, the tail becomes shortest and consequently the variance has a local minimum there.

The bottom of Fig. 5.4, the cross correlation between the matter and the spin temperature fluctuations, strongly supports the above interpretation. Here we evaluate the cross correlation from the cross power spectrum as

$$L_{m\eta} := \int \frac{d^3k}{(2\pi)^3} P_{m\eta}(k). \tag{5.11}$$

At higher redshifts ($z \gtrsim 23$), the correlation is negative, that is, high-density regions have lower spin temperature. This would be due to the WF effect. On the other hand, at lower redshifts ($z \lesssim 23$), as is expected from the interpretation that the X-ray heating is effective here, the correlation is positive. It is seen that the cross correlation changes the sign at the same redshift as the skewness.

Finally, we vary the number of X-ray photons emitted per solar mass, ζ_X [89], and see the one-point statistics again. We take $\zeta_X = 10^{55}\ M_\odot^{-1}, 10^{56}\ M_\odot^{-1}$ (fiducial value), and $10^{57}\ M_\odot^{-1}$, fixing the other parameters. The left top of Fig. 5.5 is the thermal history and

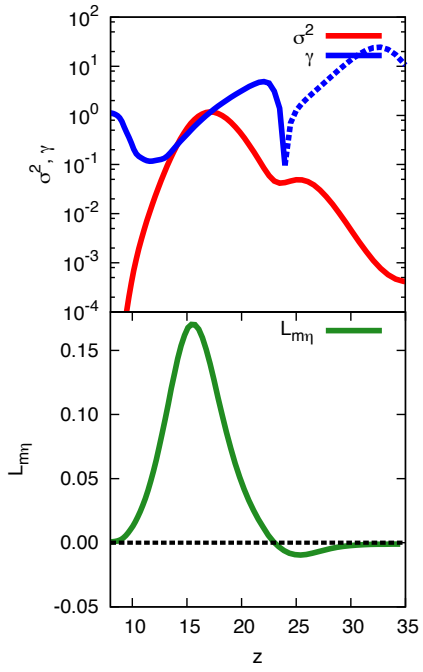

Figure 5.4: [top] Variance(red solid line) and skewness(blue line) of $1-T_\gamma/T_\mathrm{S}$ as functions of redshift. For the skewness, the dashed part corresponds to the negative skewness ($\gamma < 0$). [bottom] Cross correlation between δ_m and η as a function of redshift. Green dashed line corresponds to $L_{m\eta} = 0$.

we see that the spin temperature rises earlier for larger ζ_X. The other panels of Fig. 5.5 show the evolution of the variance and skewness of the PDF of η, and the cross correlation between matter and η fluctuations. As ζ_X increases, the critical redshift where the variance has a local minimum and the sign of the skewness and cross correlation changes increases. This is the expected behavior from our interpretation given in the previous section because the X-ray heating will become effective earlier for larger ζ_X. The power spectra of the brightness temperature contributed from the fluctuations in η are plotted in Fig. 5.6 and, as expected again, the dip appears earlier for larger ζ_X.

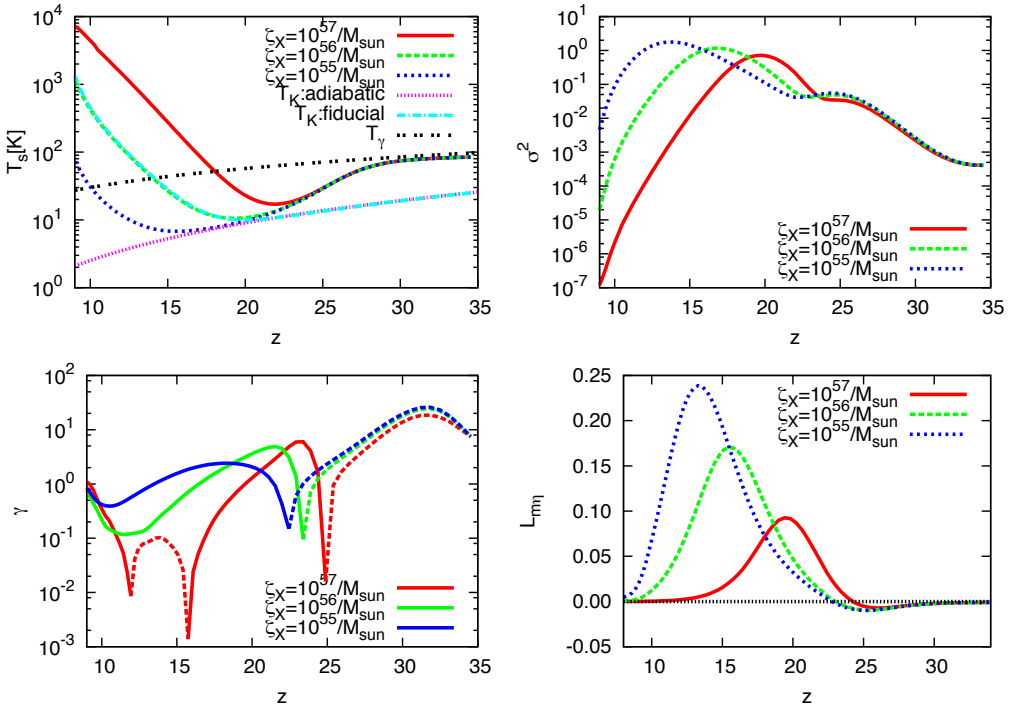

Figure 5.5: [left top] The evolution of the spin temperature for $\zeta_X = 10^{57}$ $M_\odot^{-1}$ (red), 10^{56} $M_\odot^{-1}$ (green) and 10^{55} $M_\odot^{-1}$ (blue). We also plot kinetic temperature in the absence of the X-ray heating (pink) and in the presence of the X-ray heating with $\zeta_X = 10^{56}$ $M_\odot^{-1}$ (light blue) and the CMB temperature (black). [right top and left bottom] Evolution of variance and skewness of the probability distribution function of $1-T_\gamma/T_S$ for $\zeta_X = 10^{57}$ $M_\odot^{-1}$ (red), 10^{56} $M_\odot^{-1}$ (green) and 10^{55} $M_\odot^{-1}$ (blue). [right bottom] Cross correlation between δ_m and δ_η for $\zeta_X = 10^{57}$ $M_\odot^{-1}$ (red), 10^{56} $M_\odot^{-1}$ (green) and 10^{55} $M_\odot^{-1}$ (blue).

In summary, the dip in the evolution of power spectrum contributed from the spin temperature fluctuations can be understood as the state that the X-ray heating is effective. The transition occurs at $z \approx 23$ for a fiducial set of model parameters and this depends on the effectiveness of the X-ray heating. Conversely, our interpretation implies that, if we detect a dip in the redshift dependence of the power spectrum at the relatively higher redshift, we could know the redshift when X-ray begins to become effective. Further, when we detect a peak, it would be possible to know whether the X-ray heating is effective at the redshift from the skewness. However, although the spin-temperature fluctuations are dominant at large scales, the contribution from matter fluctuations is not negligible and change the critical redshift as we see in the next section.

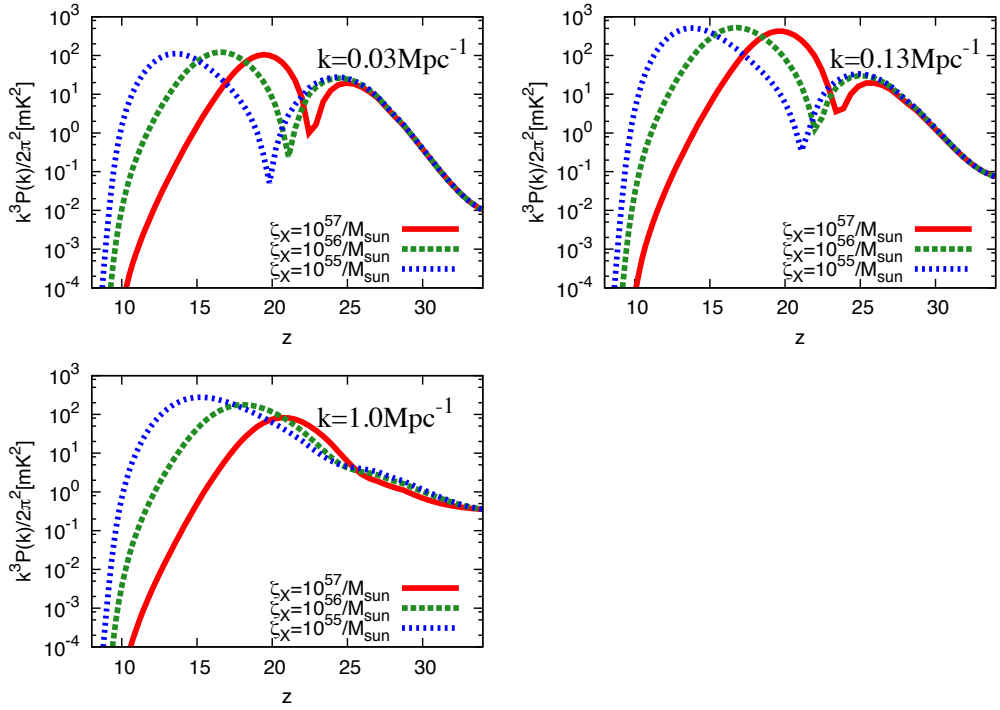

Figure 5.6: Power spectra of the brightness temperature contributed from the fluctuations in $1-T_\gamma/T_{\rm S}$ for $\zeta_X = 10^{57}\ M_\odot^{-1}$ (red), $10^{56}\ M_\odot^{-1}$ (green) and $10^{55}\ M_\odot^{-1}$ (blue) at three wave numbers as functions of redshift.

Here, it is important to note the difference between the redshift of the local minimum of the average spin temperature and the above critical redshift. The difference is due to the fact that the average spin temperature is a global property of the intergalactic gas while the skewness is largely affected by the behavior of a small fraction of gas near stars. Thus, the latter is more sensitive to the onset of the X-ray heating. If so, it is expected that the difference in the two redshifts depends on the spectrum of X-ray [36]. For example, if the X-ray spectrum is hard, the difference will become smaller because higher-energy X-rays have larger mean free path so that they tend to heat larger region around the source.

5.4 One-point statistics of the brightness temperature

In this section, we focus on the one point statistics of the brightness temperature. The variance and skewness of the brightness temperature are described by

$$\sigma_{\delta T_b} = (\overline{\delta T_b})^2[\sigma_{\delta_m} + \sigma_{\delta_\eta} + \sigma_{\delta_{x_{\rm H}}} + \langle\delta_m\delta_\eta\rangle + \langle\delta_m\delta_{x_{\rm H}}\rangle + \langle\delta_\eta\delta_{x_{\rm H}}\rangle + O(\delta^3)]. \tag{5.12}$$

$$\begin{aligned}\gamma_{\delta T_b} = (\overline{\delta T_b})^3[&\gamma_{\delta_m} + \gamma_{\delta_\eta} + \gamma_{\delta_{x_{\rm H}}} + \langle\delta_m\delta_\eta\delta_{\rm x_H}\rangle \\ &+ 3(\langle\delta_m^2\delta_\eta\rangle + \langle\delta_m^2\delta_{\rm x_H}\rangle + \langle\delta_\eta^2\delta_{\rm x_H}\rangle \\ &\quad + \langle\delta_m\delta_\eta^2\rangle + \langle\delta_m\delta_{\rm x_H}^2\rangle + \langle\delta_\eta\delta_{\rm x_H}^2\rangle) + O(\delta^4)]. \end{aligned} \tag{5.13}$$

Here, we notice that $\overline{\delta T_b}$ is slightly different from the average $\langle\delta T\rangle$ obtained by the brightness temperature map due to the contribution of higher-order terms. Although we focus on relatively high redshift, we find that $\delta_{\rm x_H}$ is important when we consider the skewness.

In Figs.5.7 and 5.8, we plot the variance and skewness of the brightness temperature with their components. Comparing the variance with skewness, we find that neutral-fraction fluctuation $\delta_{x_{\rm H}}$ is not negligible in skewness at $z \leq 20$, although it does not contribute to the total variance so much. As you can see Fig. 5.8, the change of sign in skewness for the brightness temperature is deviated from the one of η due to the contribution of matter fluctuations, which have always negative skewness. Nonetheless, the skewness is still a good indicator to study the epoch when the X-ray heating becomes effective. We note here that the nonlinear terms in skewness is the same order as the linear terms but qualitative behavior does not change whether we include nonlinear terms or not.

5.5 Discussion

In this chapter, we gave a physical interpretation of the evolution of the power spectrum of the 21 cm brightness temperature during the Cosmic Dawn and the EoR using a public code, 21 cmFAST. With a fixed wave number, the power spectrum has three peaks as a function of redshift. First, we decomposed the power spectrum into those contributed from the fluctuations in dark matter density, the spin temperature and neutral fraction and found that the peak with the lowest redshift is mostly contributed from the neutral fraction, while the other two peaks are contributed from the dark matter density and the spin temperature fluctuations. Further, it was found that a dip between two peaks with higher redshifts is induced by the neutral fraction. Then, to understand the physical meaning of the dip, we investigated the one-point function of the spin temperature distribution. We found that the redshift of the dip is critical in a sense that the skewness of the one-point function and the correlation coefficient between the spin temperature and dark matter distribution change their signs and that the variance also has a dip. From this fact, it was implied that the dip in the power spectrum of the brightness temperature contributed from the spin temperature is a signature of the onset of the X-ray heating of the gas. This interpretation was justified by seeing the behavior when varying the model parameter corresponding to the X-ray heating.

Due to the contribution of dark matter density, the redshift of the dip in the power spectrum contributed from the spin temperature is slightly different from that in the full power spectrum. However, the dip will still be a good indicator of the onset of the X-ray heating. Further, based on the cosmological perturbation theory, we can theoretically estimate the skewness of the brightness temperature contributed from the dark matter fluctuations in the standard cosmological model. Therefore, in principle, we can extract

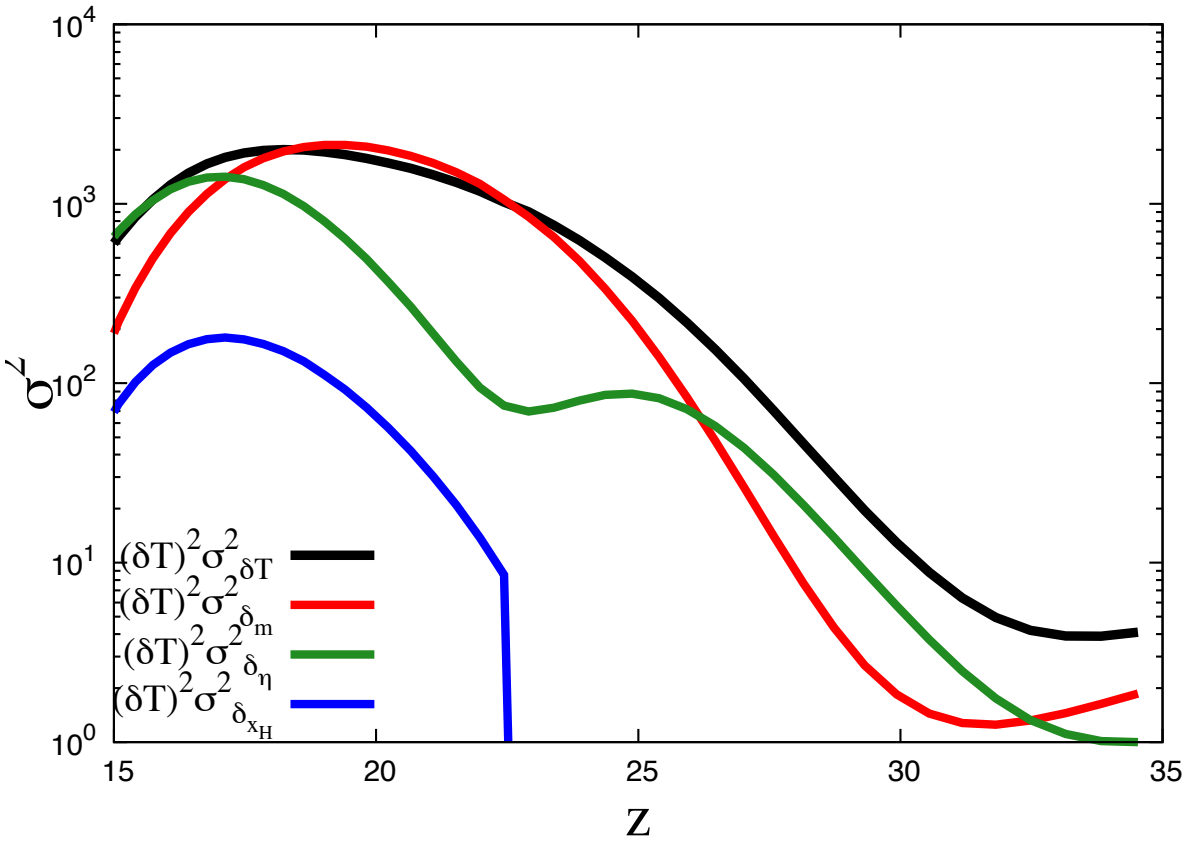

Figure 5.7: The variance of the brightness temperature(black), of δ_m(red), of δ_η(green), of δ_{x_H}(blue). All quantities are multiplied $(\overline{\delta T_b})^2$.

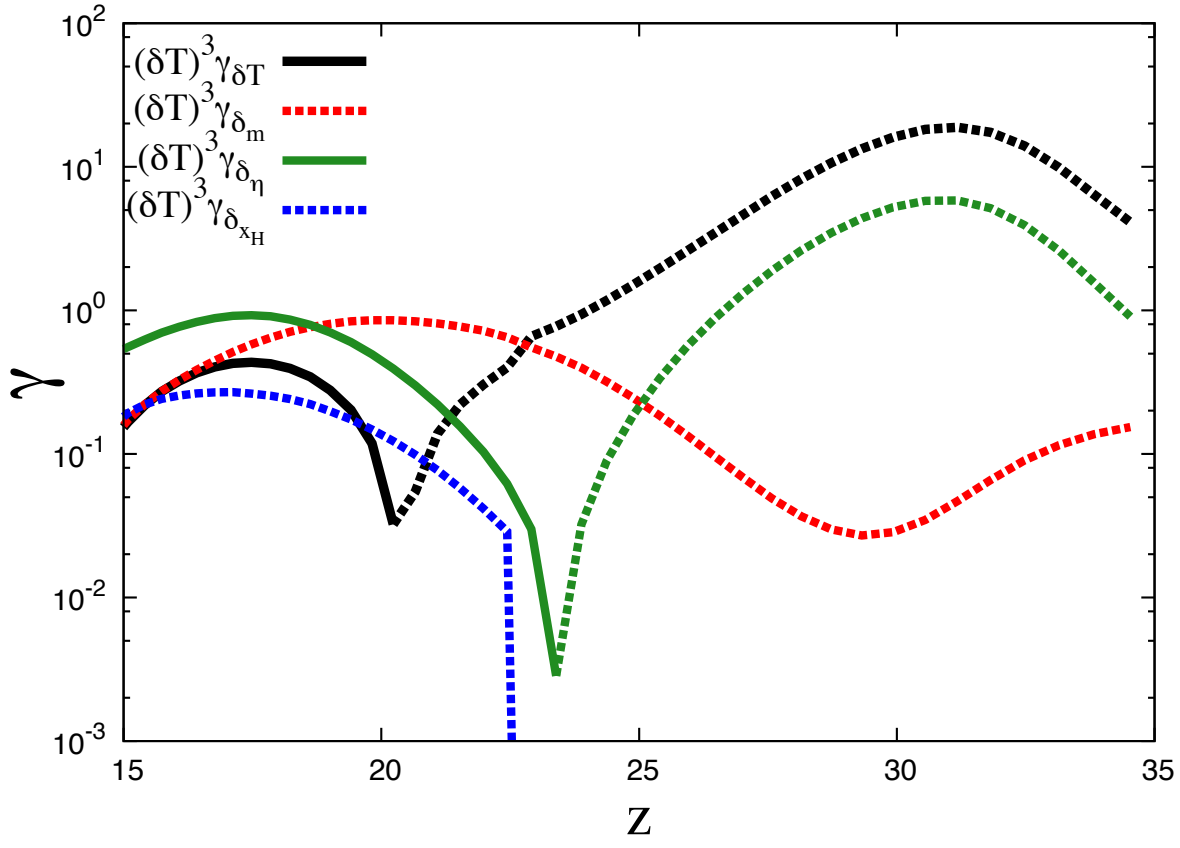

Figure 5.8: The skewness of the brightness temperature(black), of δ_m(red), of δ_η(green), of δ_{x_H}(blue). Dashed part corresponds to negative value and solid part corresponds to positive value. All quantities are multiplied $(\overline{\delta T_b})^3$.

the dark matter contribution and directly measure the skewness of the contribution from the spin temperature. Moreover, the scale dependence of the bispectrum, which has a close relation to the skewness, of the brightness temperature would help us to extract the information about the spin temperature from the observed brightness temperature. The bispectrum is also deeply related to the nonlinear terms [73] in the power spectrum which we neglected in this chapter. Because the fluctuations in the spin temperature are of order $\sim O(0.1)$ and are deviated from Gaussian distribution, the nonlinear terms are potentially important. In particular, we found that the linear and nonlinear terms are comparable when we evaluate the skewness. Further, the bispectrum and higher-order statistics would be very useful to extract physical information from 21 cm signal [97, 23, 25], as mentioned above. These topics will be presented next.

The detectability of variance and skewness was discussed in [55, 66, 134]. Following [134], the signal-to-noise ratio, S/N, of skewness can be roughly estimated by

$$S/N \sim \sqrt{\frac{\gamma^2\sigma^3}{\sigma_{\rm noise}^6/N_{\rm pix}}}, \tag{5.14}$$

where we have neglected the contribution from kurtosis. Here, $N_{\rm pix}$ is the number of pixels and we set $N_{\rm pix} = 300^3$ and $\sigma_{\rm noise}$ is the instrumental noise on the brightness temperature given by

$$\begin{aligned}\sigma_{\rm noise} &= 0.37{\rm mK}\left(\frac{10^6{\rm m}}{A_{\rm tot}}\right)\left(\frac{5'}{\Delta\theta}\right)^2\left(\frac{1+z}{10}\right)^{4.6} \\ &\times\sqrt{\left(\frac{1\ {\rm MHz}}{\Delta\nu}\frac{1000\ {\rm hours}}{t_{\rm int}}\right)},\end{aligned} \tag{5.15}$$

where $A_{\rm tot}$ is the total effective area of array, θ is angular resolution, $\Delta\nu$ is frequency resolution and $t_{\rm int}$ is observing time. Considering SKA1 ($A_{\rm tot} = 4\times10^5[{\rm m}^2]$) and SKA2 ($A_{\rm tot} = 3\times10^6[{\rm m}^2]$) with 1000 hours of observation time and $\Delta\nu \sim 0.1$MHz, we obtain S/N = 6 and 18 at $z = 15$, and S/N = 2 and 8 at $z = 20$, for SKA1 and SKA2, respectively.

Finally, we would like to note that the variance and skewness are actually dependent on the angular resolution and survey area. This can be understood by the fact that they are expressed by the integration of power spectrum and bispectrum with respect to the wavenumber. In our calculation, we have fixed the box size and the number of grids in simulations to be (200 Mpc)^3 and 300^3, respectively. This is corresponding to 0.66 Mpc resolution or $\sim$ 3 arcmin at 80 MHz ($z = 17$). In Fig. 5.9, we show the evolution of skewness of the brightness temperature with varying the spacial resolution $0.66, 1.3$ and 2.0 Mpc. These correspond to 3 arcmin, 6 arcmin, 9 arcmin. and fixing the box size. The lowest resolution roughly corresponds to that of SKA2. It is seen that the peak at $z \sim 18$ is diminished for higher resolution, while the one at $z \sim 30$ is not affected. On the other hand, the change of sign is shifted slightly to higher redshift for higher resolution. More detailed study on the dependence of skewness on the resolution needs the understanding of the bispectrum of the brightness temperature fluctuations and this will be presented elsewhere.

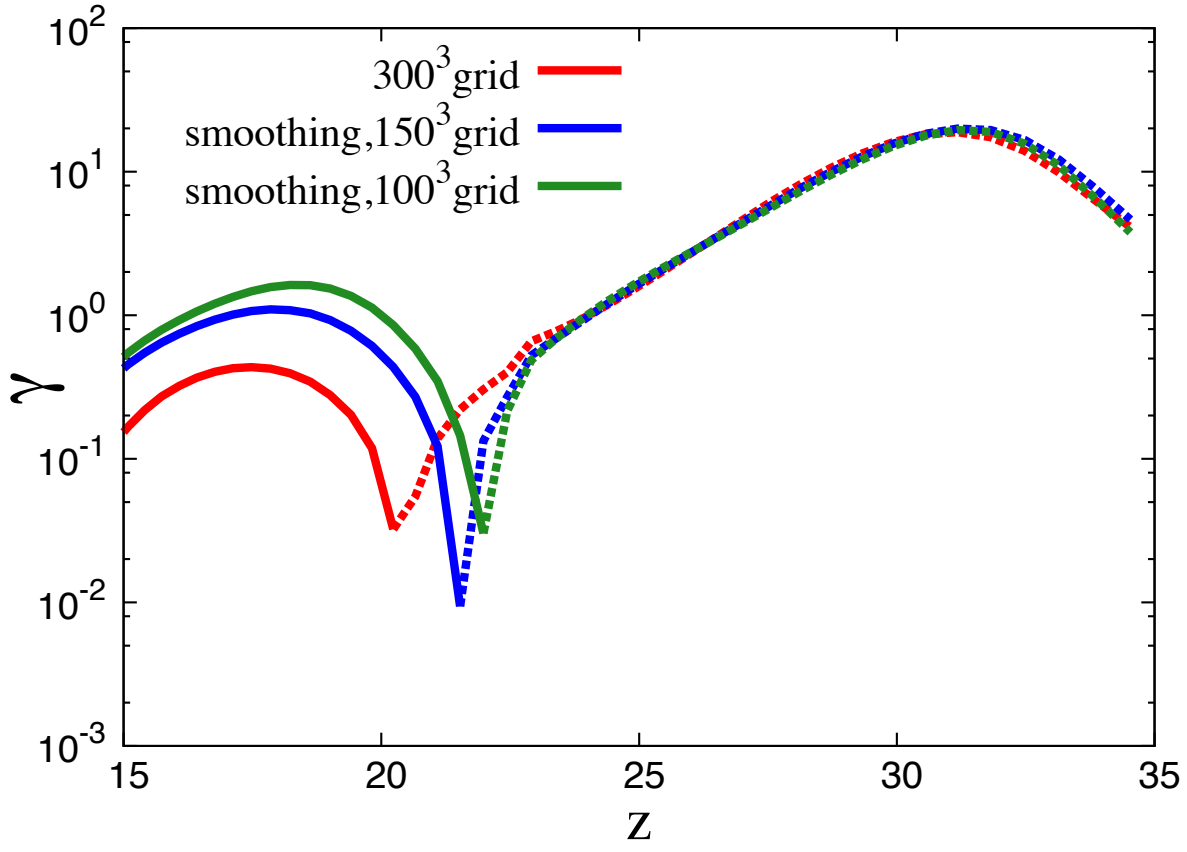

Figure 5.9: The evolution of the brightness temperature skewness varying the number of grids: 300^3 (fiducial, red), 150^3 (blue) and 100^3 (green). The latter two cases are calculated by smoothing the fiducial model.

Chapter 6

21 cm bispectrum

In previous chapter, we studied the variance and skewness of the 21 cm fluctuations to give a clear interpretation of the 21 cm power spectrum and find that skewness is a good indicator of the epoch when the X-ray heating becomes effective. Thus, the non-gaussian feature of the spatial distribution of the 21 cm signal is expected to be useful to investigate the astrophysical effects in the CD and the EoR because skewness can estimate the non-gaussian feature in a distribution. In this chapter, in order to investigate such a non-Gaussian feature in more detail, we focus on the bispectrum of the 21 cm signal. It is expected that the 21 cm brightness temperature bispectrum is produced by non-gaussianity due to the various astrophysical effects such as the Wouthysen-Field (WF) effect, the X-ray heating and reionization. We study the various properties of the 21 cm bispectrum such as scale dependence, shape dependence and the redshift evolution. And also we study the contribution from each component of the 21 cm bispectrum. We find that the contribution from each component has characteristic scale-dependent feature. In particular, we find that the bulk of the 21 cm bispectrum at z =20 comes from the matter fluctuations, while in other epochs it is mainly determined by the spin and/or neutral fraction fluctuations and it is expected that we could obtain more detailed information on the IGM in the CD and the EoR by using the 21 cm bispectrum in the future experiments, combined with the power spectrum and skewness. This chapter is based on [119]

6.1 Introduction

In previous chapter, we gave an interpretation to the time evolution of the 21 cm power spectrum and we find that the size of skewness is sensitive to the epoch when the X-ray heating becomes effective. Other work also reports the impact of the spin temperature fluctuations on the skewness [135] and there is a work which focuses on the redshift distortion as the indicator of the epoch where the X-ray heating is effective[37]. Herein we extend these previous works by considering the bispectrum to investigate the dependence of the skewness on scales because skewness is an integral of the bispectrum with respect to the wave number (see Appendix A). In a different work [144], we have already estimated errors from the thermal noise of detectors in estimating the bispectrum and we found that the 21 cm bispectrum would be detectable at large scales at $k \leq 0.1\mathrm{Mpc}^{-1}$ even by the current detectors on, such as, the MWA and PAPER. Further, the 21 cm bispectrum would be detectable even at small scales with SKA [144], and therefore the study of the bispec-

trum is timely and well motivated. Some previous works studied the 21 cm bispectrum [23, 97, 25, 94, 24]. These works, however, mainly focus on the bispectrum as a measurement of primordial non-gaussianity in matter fluctuations. In our study, we instead focus on non-Gaussianity in 21 cm fluctuations induced by astrophysical effects, whose size is expected to be larger than that in matter fluctuations. (For other probes of non-Gaussianity such as Minkowski functionals, see [49, 78, 60].)

6.2 Formulation and set up

6.2.1 Formulation for the 21 cm bispectrum

We have introduced the 21 cm power in eq.(6.1) as follows:

$$\langle \delta_{21}(\mathbf{k})\delta_{21}(\mathbf{k}^{'})\rangle = (2\pi)^3\delta(\mathbf{k}+\mathbf{k}^{'})P_{21}(\mathbf{k}), \tag{6.1}$$

where,

$$\delta_{21}(\mathbf{x}) \equiv \delta T_b(\mathbf{x}) - \langle \delta T_b\rangle. \tag{6.2}$$

If the statistics of the brightness temperature fluctuations is pure Gaussian, the statistical information on the brightness temperature should be completely characterized by the power spectrum, and in the above expression for the brightness temperature given by Eq. (4.40), if both of the spin temperature and the neutral fraction are completely homogeneous, the statistics of the brightness temperature fluctuations completely follows that of the density fluctuations δ_m. However, in the era of CD and EoR, it is expected that the spin temperature and the neutral fraction should be spatially inhomogeneous and the statistics of the spatial fluctuations of those quantities would be highly non-Gaussian due to the various astrophysical effects. Accordingly, the statistics of the brightness temperature fluctuations would deviate from the pure Gaussian and it should be important to investigate the non-Gaussian feature of the brightness temperature fluctuations. Although such a non-Gaussian feature can be investigated through the skewness of the one-point distribution functions as done in [118], the scale-dependent feature has been integrated out in the skewness. On the other hand, the higher order correlation functions in Fourier space such as a bispectrum and a trispectrum characterize the non-Gaussian features and also have the scale-dependent information. Here, in order to see the non-Gaussian feature of the brightness temperature fluctuations δ_{21}, we focus on the bispectrum of δ_{21} which is given by

$$\langle \delta_{21}(\mathbf{k}_1)\delta_{21}(\mathbf{k}_2)\delta_{21}(\mathbf{k}_3)\rangle = (2\pi)^3\delta(\mathbf{k}_1+\mathbf{k}_2+\mathbf{k}_3)B(\mathbf{k}_1,\mathbf{k}_2,\mathbf{k}_3). \tag{6.3}$$

In order to characterize the shape of the bispectrum in k-space, we use an isosceles ansatz which is defined as $k_1 = k_2 = k = \alpha k_3$ ($\alpha \geq 1/2$). For examples, in case with $\alpha \gg 1$ the shape of the bispectrum is often called as *squeezed type* or *local type*, in case with $\alpha = 1$ it is called as *equilateral type*, and in case with $\alpha = 1/2$ it is called as *folded type*. Note that we relax the configuration condition because we calculate the bispectrum from the grid point. We regard the length within the range of 10% of side of the triangle we desire as the that of triangle.

6.2.2 Calculation of the 21 cm bispectrum

In this chapter, we calculate the bispectrum of the brightness temperature fluctuations (the 21 cm bispectrum) by making use of 21 cmFAST [87, 88].

We perform simulations in a $(200\mathrm{Mpc})^3$ comoving box with 300^3 grids, which corresponds to 0.66 cMpc resolution or $\sim 12.7(14.1)$ arcsec at 80 (127) MHz ($z = 17$ (10)) and $1.07(1.19)\mathrm{deg}^2$ field of view at 80 (127) MHz ($z = 17$ (10)), from $z = 200$ to $z = 8$ adopting the following parameter set, $(\zeta, \zeta_X, T_{\rm vir}, R_{\rm mfp}) = (31.5, 10^{56}/M_\odot, 10^4\ \mathrm{K}, 30\ \mathrm{Mpc})$. Here, ζ is the ionizing efficiency, ζ_X is the number of X-ray photons emitted by source per solar mass, $T_{\rm vir}$ is the minimum virial temperature of halos which produce ionizing photons, and $R_{\rm mfp}$ is the mean free path of ionizing photons through the IGM. In our calculation, we also ignore, for simplicity, the gradient of peculiar velocity whose contribution to the brightness temperature is relatively small (a few %) [47]. We perform 10 realizations of simulations with different initial condition of density fluctuations and obtain the brightness temperature maps. Then we evaluate the average bispectrum as

$$\begin{aligned} abs[\overline{B(k)}] &= \frac{1}{N}\sum_{i=1}^{N} abs[B(k)]_i \\ &= \frac{1}{N}\sum_{i}^{N}(\mathrm{Re}[B(k)]^2 + \mathrm{Im}[B(k)]^2)_{i=1}^{1/2}. \end{aligned} \tag{6.4}$$

Here, N is the number of realizations and k is the absolute value of $\mathbf{k}$.

6.3 Result

In this section, we summarize our result for the 21 cm bispectrum.

6.3.1 Scale-dependence of the 21 cm bispectrum

First, in order to see the scale-dependence of the 21 cm bispectrum, we focus on the equilateral shape, that is, $\alpha = 1$ case for the isosceles ansatz discussed in the previous section. We plot the equilateral type bispectrum as a function of wave number k with 1-σ sample variance for several redshifts ($z = 10, 15, 20$ and 27) in Fig.6.1. Here, we use the normalized bispectrum which is given by $k^6 abs[\overline{B(k)}]$. $z = 10$ is a typical redshift during the EoR, and $z = 15$ and 20 are expected to be a transition time from CD to the EoR, while $z = 27$ is a typical time during CD. As you can see, the variance is relatively small and the cosmic variance is not so serious for the field size and wavenumbers we chose. From this figure, we can find that, except for the case with $z = 20$, the normalized bispectrum is almost scale-invariant for the equilateral shape. On the other hand, for $z = 20$, the normalized bispectrum has a scale-dependence as $\propto k^2$. Such difference is expected to depend on what component gives a dominant contribution to the 21 cm bispectrum and we will discuss this issue later.

Next, we show a comparison of bispectra of equilateral ($\alpha = 1$), folded ($\alpha = 1/2$) and squeezed ($\alpha = 10$) types in Fig. 6.2. Here, the bispectra are plotted as functions of k_3 for several redshifts. From this figure, we can see that the scales and shapes which mostly

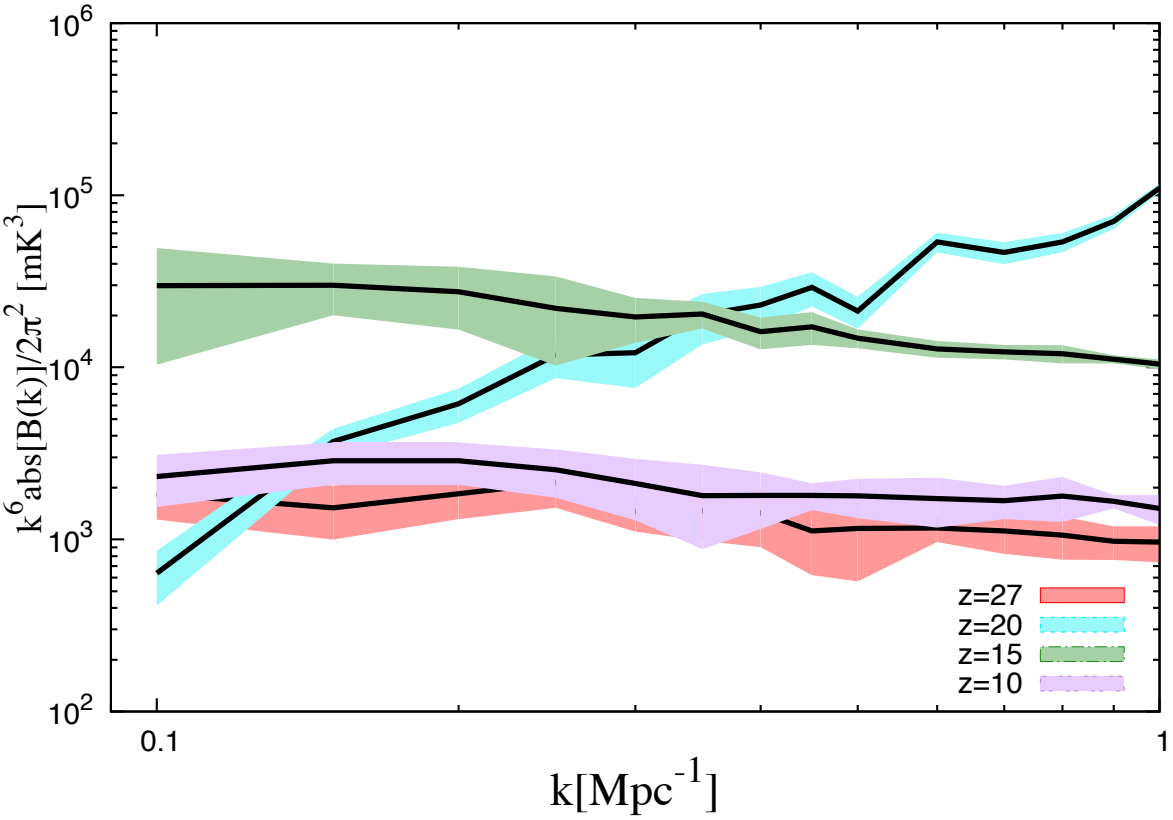

Figure 6.1: Equilateral type bispectra as functions of wave number at $z = 27$ (red), 20 (cyan), 15 (green), 10 (purple). The shaded region associated with each line represents 1-σ sample variance estimated from 10 realizations.

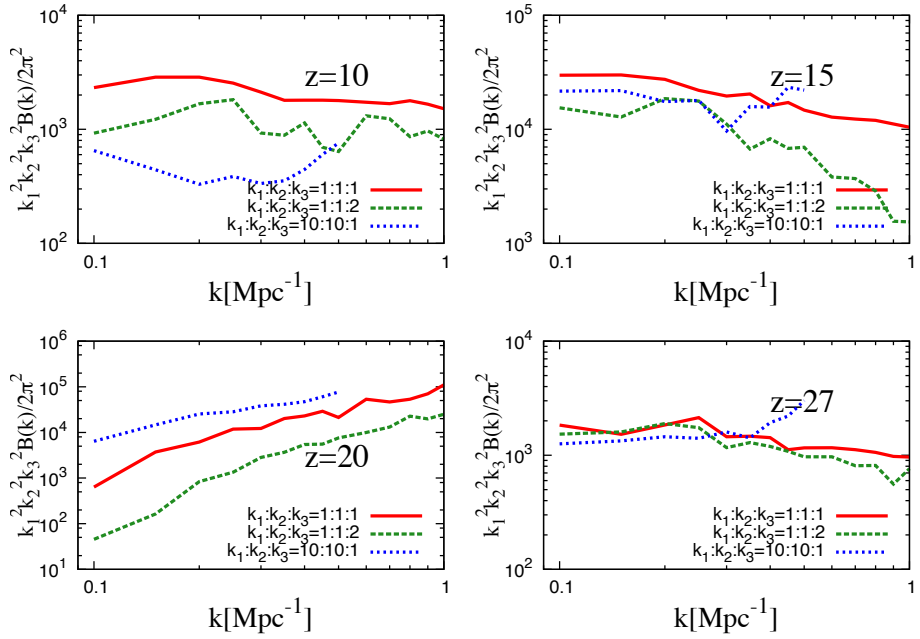

Figure 6.2: Scale dependence of bispectra for $(k_1 : k_2 : k_3) = (1 : 1 : 1), (1 : 1 : 2)$and $(10 : 10 : 1)$, as functions of k_3.

contribute to the skewness since skewness is the integral of bispectra (see Appendix A). In particular, smaller scales contributes to the skewness at $z = 20$ although the bispectrum is nearly scale invariant at other redshifts.

6.3.2 Redshift evolution of the 21 cm bispectrum

Next, we consider the redshift evolution of the 21 cm bispectrum. In Fig. 6.3, we show the bispectra as functions of redshift for several α: the equilateral shape ($\alpha = 1$), the folded shape ($\alpha = 1/2$) and the squeezed shape ($\alpha = 10$) with $k = 1.0$ Mpc^{-1}. For the equilateral and folded cases, we can see two peaks located at around $z = 20$ and 12. These peaks can also be seen in the power spectrum of the brightness temperature fluctuations, $P_{21}(k)$, with $k \simeq 1.0$ Mpc^{-1} (see Fig.5.1). On the other hand, in case with the squeezed shape, three peaks appear at around $z = 23$, 17, and 12. This feature is similar to that of the power spectrum with $k \simeq 0.1$ Mpc^{-1} [118]. For the squeezed type, we take the parameter α to be 10 and this means $k_3 = 0.1$ Mpc^{-1}. Hence, the squeezed-type 21 cm bispectrum is expected to be described in terms of not only the power spectrum with larger two wave number (k_1 and k_2 in our case) but also that with smaller one wave number (k_3 in our case) and also it would have the information about the correlation between the long and short wavelength modes in Fourier space or local nonlinearity in real space.

We will also investigate what physics cause such a correlation between the long and short wavelength modes in the 21 cm bispectrum in later subsection.

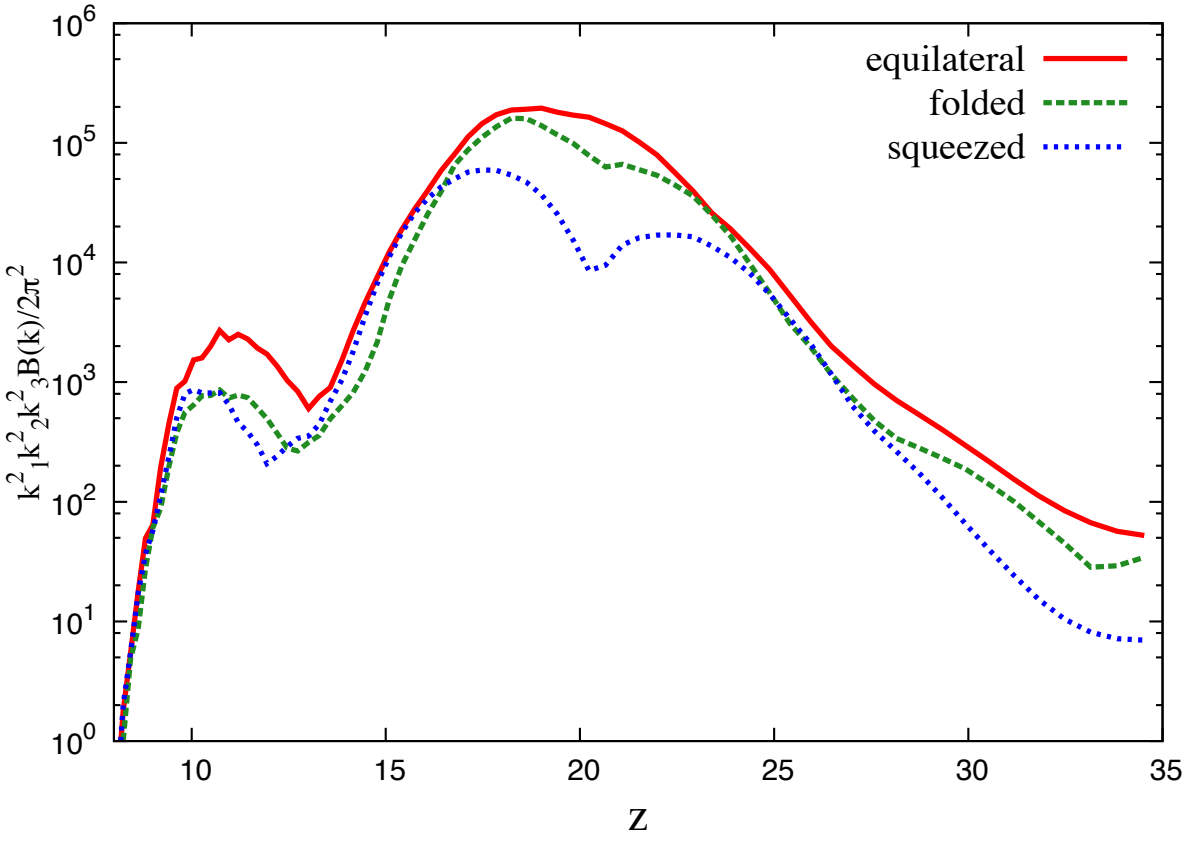

Figure 6.3: Comparison of bispectra of typical triangle configurations. We fix $k = 1.0$ Mpc^{-1} and take $\alpha = 1$ (equilateral: red solid line), $\alpha = 1/2$ (folded: green dashed line) and $\alpha = 10$ (squeezed: blue dotted line) for the isosceles ansatz.

6.3.3 Decomposition of the 21 cm bispectrum

By using Eq. (5.2), we can also decompose the 21cm bispectrum into auto- and cross-correlation of $\delta_m, \delta_{x_{\rm H}}$ and δ_η:

$$\begin{aligned} B_{\delta T_b} &= (\overline{\delta T}_b)^3[B_{\delta_m\delta_m\delta_m} + B_{\delta_{x_{\rm H}}\delta_{x_{\rm H}}\delta_{x_{\rm H}}} + B_{\delta_\eta\delta_\eta\delta_\eta} \\ &\quad +(\text{cross correlation terms}) \\ &\quad +(\text{higher order terms})]. \end{aligned} \tag{6.5}$$

In the above equation, the cross correlation terms and the higher order terms come from the fact that the brightness temperature is expressed as Eq. (5.2) and they should appear even if the statistics of $\delta_m, \delta_{x_{\rm H}}$ and δ_η are completely Gaussian. In this sense, the first three terms in the above expression, which are the auto-bispectra of $\delta_m, \delta_{x_{\rm H}}$ and δ_η, should be corresponding to the intrinsic non-Gaussian features of these components and we focus on these auto-bispectra below.

In Fig. 6.4, we plot the brightness temperature bispectrum and the above auto-bispectra terms for equilateral type as functions of redshift (upper panels). From this figure, we can see that the total bispectra are mostly contributed from the auto-bispectra of the matter density field, the fluctuations of the spin temperature and the neutral fraction, which are expressed as the first three terms in Eq. (6.5), for all redshifts. For comparison, the evolution of power spectra is also shown (lower panels) and we find that the behavior of each component is very similar between bispectrum and power spectrum. Such a correspondence is highly non trivial, since the bispectrum and power spectrum reflect different aspects of the statistical properties of the fluctuations as we have mentioned.

Let us try to interpret the behavior of bispectra, comparing that of power spectra which was detailed in previous chapter. First, fluctuations in neutral hydrogen fraction appear when reionization begins and become dominant as reionization proceeds ($z \lesssim 12$). The dip at $z \sim 14$ corresponds to the redshift when the average spin temperature becomes equal to the CMB temperature and the average brightness temperature $\overline{\delta T_b}$ vanishes. This dip appears in the contribution of matter fluctuations for the same reason. Thus, this dip is independent of the properties of fluctuations and this is why both the power spectra and bispectra from $\delta_{x_{\rm H}}$ and δ_m have a dip at the same redshift.

On the other hand, the spin temperature fluctuations are negligible at low redshifts ($z \lesssim 10$), because the spin temperature is much higher than the CMB temperature everywhere, that is, $\eta = 1 - T_\gamma/T_{\rm S}$ is very close to unity and independent of $T_{\rm S}$. However they substantially contribute at higher redshifts ($z \gtrsim 14$) and have two peaks at $z \sim 15$ and $z \sim 25$ at large scales while the higher-redshift peak is much less noticeable at small scales. The dip at $z \sim 23$ is induced by the onset of the X-ray heating. At higher redshifts ($z \gtrsim 23$), the spin temperature in dense region is lower than the average due to the WF effect, which couples the spin temperature to the kinetic temperature which is much lower than the CMB temperature. As a consequence, the probability distribution function (pdf) of the spin temperature is negatively skewed at this epoch. Contrastingly, at lower redshifts ($z \lesssim 23$), the X-ray heating becomes effective for our parameter set and the spin temperature in dense region rises rapidly so that the skewness of the pdf changes its sign. Thus, at the onset of the X-ray heating ($z \sim 23$), the pdf becomes close to Gaussian with relatively small width, that is, the skewness vanishes and the variance has a local minimum. Thus, in [118], it was suggested that the sign of skewness can be an indicator of the effectiveness of

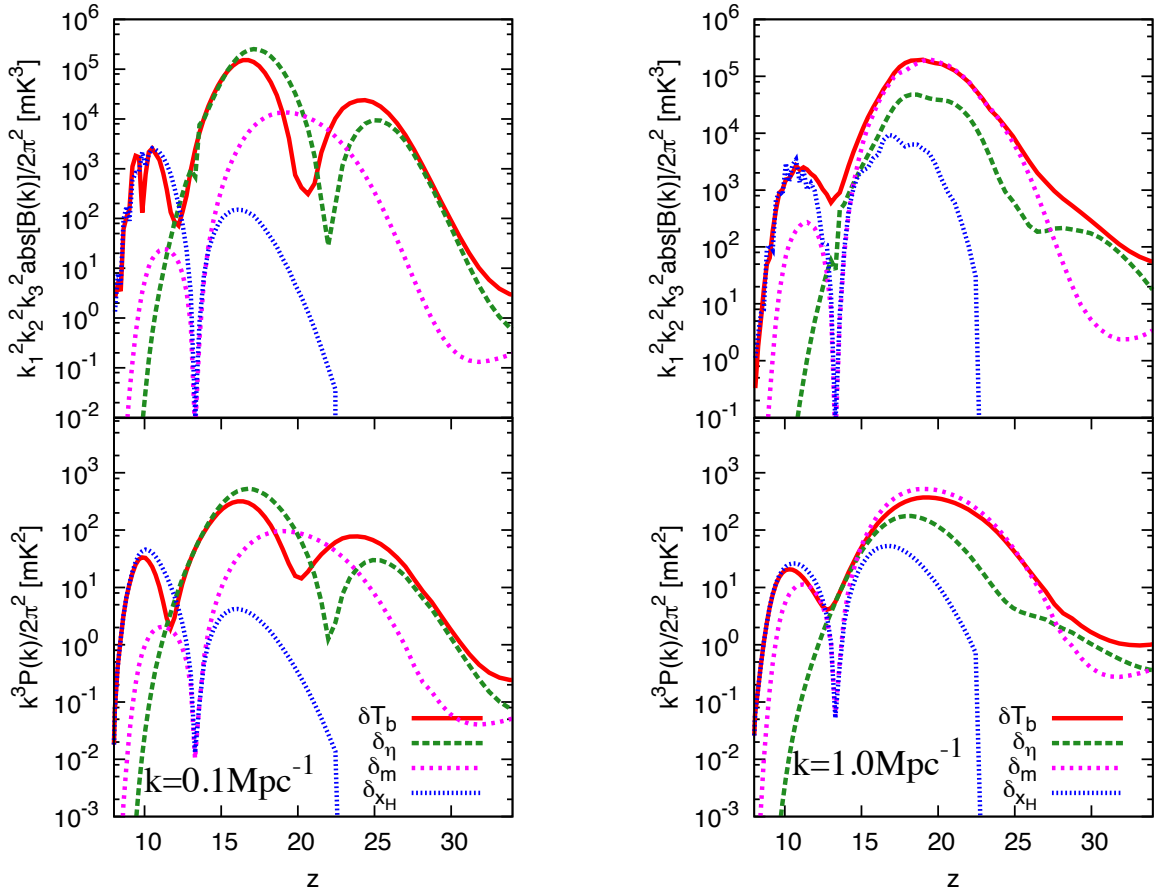

Figure 6.4: Components of the 21 cm bispectrum for equilateral type: the brightness temperature (red), the contribution from eta (green), matter fluctuations (blue) and neutral hydrogen fraction (magenta).

the X-ray heating. Remembering that the bispectrum is a measure of non-Gaussianity, it is natural that the dips in bispectrum and power spectrum are coincident with each other.

Before the EoR, the bispectrum, as well as the power spectrum, is mostly dominated by the spin temperature fluctuations at large scales and will be a good probe of astrophysical effects such as the WF effect and the X-ray heating. On the other hand, at small scales, the matter fluctuations are dominant and the bispectrum is of cosmological interest because it is induced by gravitational nonlinearity and, possibly, primordial non-Gaussianity (see, e.g., [115, 11, 68]).

Next, we focus on the shape dependence of the total bispectrum and its components. Fixing $k_3 = 1.0$ Mpc^{-1}, we plot contours of the bispectra in (k_1/k_3)-(k_2/k_3) plain in top of Fig. 6.5. Note that we do not use the normalized bispectrum, $k_1^2 k_2^2 k_3^2 B(k_1, k_2, k_3)$, but the unnormalized bispectrum, $B(k_1, k_2, k_3)$, here. We can see in what configuration of triangle the bispectra are strong. Here it should be noted that the triangle condition is not satisfied in the blank region and that the contours are symmetric with respect to a line

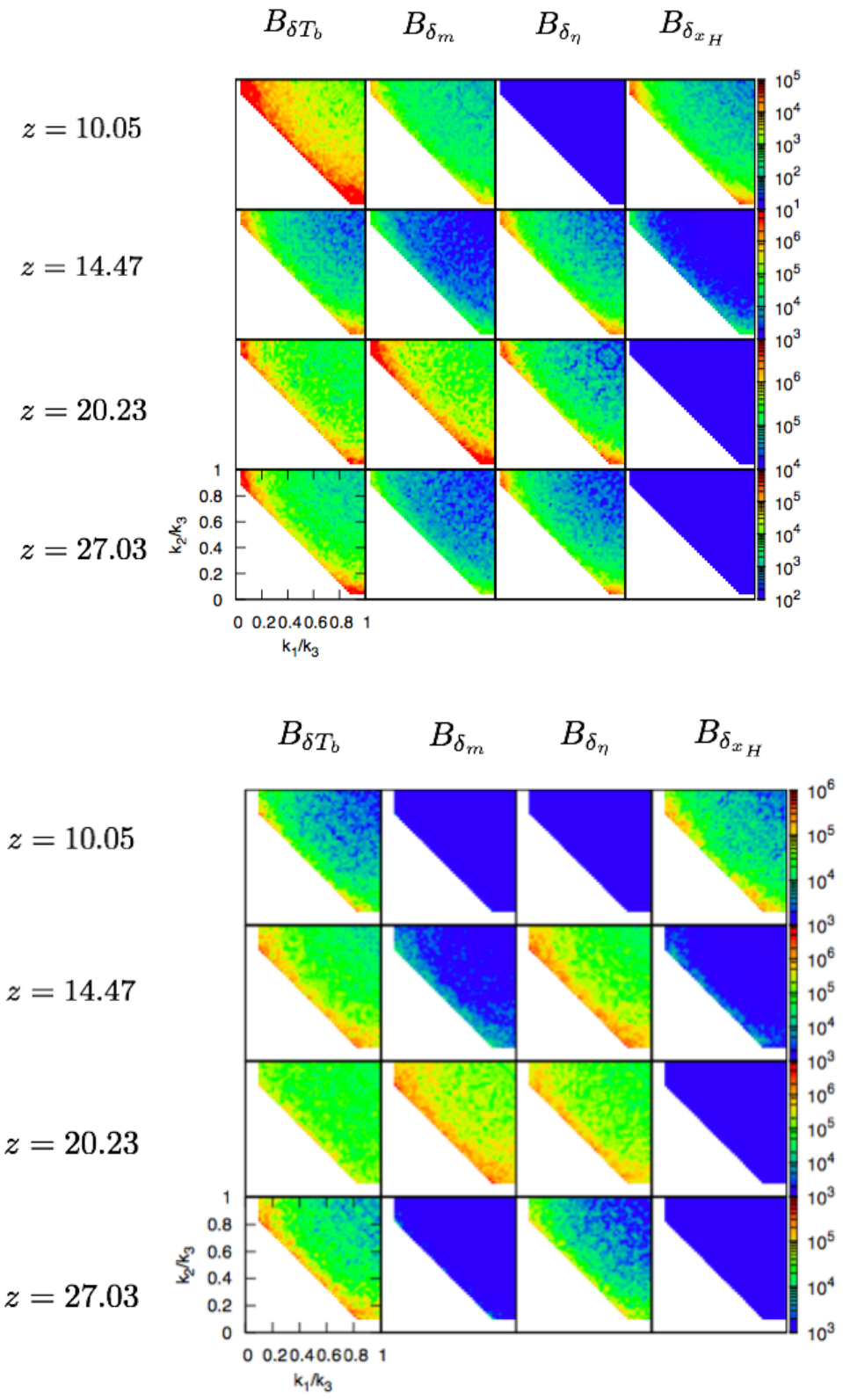

Figure 6.5: (Top) Contours of the total bispectrum and its components in k_1/k_3-k_2/k_3 plane with $k_3 = 1.0$ Mpc^{-1}. (Bottom) Contours of the total bispectrum and its components in k_1/k_3-k_2/k_3 plane with $k_3 = 0.4$ Mpc^{-1}.

$k_1/k_3 = k_2/k_3$.

At $z = 10.05$ when the EoR has proceeded to some extent, the total bispectrum is strong at folded and squeezed types. The contribution from neutral hydrogen fraction fluctuations is dominant at these configurations, while matter fluctuation is dominant at equilateral type. At $z = 14.47$, the dominant contribution comes from the spin temperature fluctuations and it is largest at squeezed type. The situation is similar at $z = 27.03$. At $z = 20.23$, both squeezed and folded type of the total bispectrum are strong. The contributions from matter and the spin temperature fluctuations are comparable at these configurations, while the former is dominant at equilateral type.

We also show the contour for $k_3 = 0.4$ Mpc^{-1} in bottom of Fig.6.5. Compared with the case of $k_3 = 1.0$ Mpc^{-1}, contributions from both matter and the spin temperature fluctuations are significant at $z = 20.23$. On the other hand, we find that the contribution from fluctuations of neutral hydrogen fraction at $z = 10.05$ is clear compared with the case of $k_3 = 1.0$ Mpc^{-1}. This helps us to extract the information on neutral hydrogen and it is better to see larger scales if we would like to know the information on neutral hydrogen fluctuations.

6.4 Discussion

In this chapter, we investigated the 21 cm bispectrum as a method to measure non-Gaussianity of the brightness temperature field.

First, we have shown the scale-dependence of the 21 cm bispectrum for the *equilateral-shape* at some redshifts. We found that the normalized 21 cm bispectrum seems not to have any characteristic scale in $0.1 \lesssim k/\mathrm{Mpc}^{-1} \lesssim 1.0$ for each redshift. For $z = 10, 15, 27$, the normalized bispectrum is almost scale-invariant, while for $z = 20$ it has a scale-dependence as $k^6 B \propto k^2$.

We have also shown the redshift evolution of the 21 cm bispectrum with fixed k for three types of the shape in k-space. We found that the redshift evolution of the 21 cm bispectrum for the equilateral and folded shapes basically traces that of the 21 cm power spectrum, but in case with the squeezed shape, we could see a different behavior and it can be understood by considering the coupling between the large- and small-scale modes.

Then, we studied the 21 cm bispectra by decomposing it into the contributions from the matter density field, the fluctuations in the spin temperature and the neutral fraction. From the redshift evolution, we found the dominant component at each redshift and scale. We also show the shape dependence of each component and compared it with that of the total 21 cm bispectrum. The shape dependence of each component looks similar to each other, but a slight difference also exists. Hence, by future precise observation it is expected that we would obtain the information about the non-Gaussian feature of these components separately.

As far as the matter bispectrum is concerned, there have been a lot of works which discuss the shape-dependence by using the second order perturbation theory and also numerical N-body simulation. Although a lot of works focus on the matter bispectrum at the lower redshift ($z \simeq 1.0$) or higher redshift ($30 \lesssim z \lesssim 100$ in the dark age) (e.g., [115, 11, 68, 116, 24, 94]), we can find that the shape of the matter bispectrum in our result is basically consistent with these previous works by extrapolation. By us-

ing the second order perturbation theory, the matter bispectrum can be expressed as $B_m(k_1, k_2, k_3) \propto P_m(k_1)P_m(k_2) + 2$ perms. with $P_m(k)$ being the matter power spectrum. For 0.1 $\mathrm{Mpc}^{-1} \lesssim k$, the matter power spectrum behaves as $\propto k^{-2\sim3}$. Based on this fact and the isosceles ansatz ($k_1 = k_2 = k = \alpha k_3$), we have $B_m(k, \alpha) \propto (1 + 2\alpha^{2\sim3})k^{-4\sim6}$, and hence the unnormalized matter bispectrum becomes larger as α increases is the largest in the squeezed shape [68].

Based on the above discussion about the matter bispectrum, let us revisit the behavior of the 21 cm bispectrum as shown in Fig. 6.1. As we have mentioned, in contrast to other redshifts, for $z = 20$ the normalized 21 cm bispectrum has a scale-dependence as k^2 in the equilateral shape. From Fig. 6.4, we find that at $z = 20$ the matter contribution relatively dominates over the 21 cm bispectrum, and hence the behavior of the 21 cm bispectrum is expected to trace that of the matter bispectrum at this redshift. Based on the expression obtained by the second order perturbation theory, the scale-dependence of the normalized matter bispectrum can be estimated as $\propto k^6 \times k^{-4\sim6} = k^{0\sim2}$. Hence, the behavior of the matter bispectrum could explain that of the 21 cm bispectrum at $z = 20$.

Naively, the spatial distributions of the spin temperature and neutral fraction should be considered as tracers of matter density field, that is, they could be treated equally with those of the halos and galaxies. Based on this consideration, the simplest way to express the spatial distributions of the spin temperature and neutral fraction is introducing a bias parameter, such as $\delta_i \propto b_i\delta_m$ ($i = \eta$ and x_{H}). If such a bias parameter is scale-independent, the behaviors of the bispectra of the spin temperature and neutral fraction are completely the same as that of the matter density field. However, we can see slight differences between these components in Fig. 6.5 and also 6.1. Hence, we expect that the bias parameter should have non-trivial scale-dependence due to the nonlinear or non-local transfer from the matter density field to the spin temperature and neutral fraction. We need to investigate this issue more deeply in future work.

The detectability of bispectrum is of critical interest. In the [144], we estimated the signal-to-noise ratio of bispectrum, developing a formalism to calculate the bispectrum contributed from thermal noise. It was found that SKA1 has enough sensitivity for $k < 0.3$ Mpc^{-1} for isosceles triangles, while LOFAR will have sensitivity for the peaks of the bispectrum as a function of redshift. Actually, galactic and extragalactic foreground will be a serious obstacle just as in the case of power spectrum and should be studied in detail.

There are some other approaches to measure non-Gaussianities in the brightness temperature field. For example, some studies focus on topological structure of the brightness temperature field such as Minkowski functionals [49, 78, 60]. This method is complementary to higher order statistics.

Chapter 7

Fisher analysis for the EoR parameters

In this chapter, we perform the Fisher analysis for the 21 cm bispectrum to forecast the EoR model parameters obtained by future observations. Further, we compare expected error on the EoR model parameters obtained by the 21 cm bispectrum with that obtained by the 21 cm power spectrum.

7.1 Introduction

Improvements of current instruments and foreground removal methods push observational 21 cm cosmology into new era. Ongoing projects such as MWA, LOFAR and PAPER have potential to detect the 21 cm power spectrum at the EoR and a future instrument SKA will be expected to detect the 21 cm power spectrum at higher redshift beyond the EoR [90, 107, 91]. Further, Yoshiura et al [144] shows that the 21 cm bispectrum at the EoR is also detectable by MWA and LOFAR at large scales $k < 0.3$ Mpc^{-1} and also detectable at both larger and smaller scales by SKA. As observational techniques develop, we expect to get much more information on the EoR from the 21 cm power spectrum and the bispectrum. In particular, what we would like to know is the answer for the questions that "what exactly can we learn information on the EoR model from observations?" and "can we refer to the nature of the EoR from the cosmic 21 cm signal?" In order to give answers for these questions, it is imperative to constrain the EoR model parameters from the cosmic 21 cm signal. Some previous works constrain the EoR parameters by using the Markov Chain Monte Carlo (MCMC) method or the Fisher forecast by applying them to the 21 cm power spectrum and the global 21 cm signal[102, 52, 76, 92, 56].

In this chapter, we perform parameter forecast by the Fisher analysis for both 21 cm power spectrum and 21 cm bispectrum with ongoing observation. We focus on MWA and LOFAR as supposed instruments. Previous work shows that the 21 cm power spectrum assuming MWA and LOFAR observations can constrain the EoR parameters[102]. However, no previous work constrain the EoR model parameters with the 21 cm bispectrum. The 21 cm bispectrum is thought to be more sensitive to change of the EoR parameters than those of power spectrum because the 21 cm bispectrum consists of three brightness tem-

perature values, whereas the 21 cm power spectrum consists of two brightness temperature values.

7.2 Parameter dependence of the 21 cm bispectrum

In this section, we study the parameter dependence of the 21 cm bispectrum in order to prepare Fisher forecast. We choose two key parameters as EoR model parameters. We briefly summarize the key parameters we choose as follow.

1. ζ, *ionizing efficiency*; ζ is composed by a number of parameters related to ionizing photons escaping from high redshift galaxies. f_{esc} is the fraction of ionizing photons escaping from galaxies into the IGM. f_* is the fraction converted from baryons to stars. N_γ is the number of ionizing photons per baryon in stars. n_{rec} is the recombination rate per baryon. With these parameters, ζ can be written by $\zeta = f_{esc} f_* N_\gamma / (1 + n_{rec})$[43]. In our calculation, we adopt $\zeta = 15$ as fiducial value to satisfy observed constraint on the ionization history.

2. $T_{\rm vir}$,*minimum virial temperature of halos producing ionizing photons*; $T_{\rm vir}$ parameterizes the minimum mass of halos producing ionizing photons at the EoR. Typically, $T_{\rm vir}$ is chosen to be 10^4K corresponding to the temperature that atomic cooling become effective. $T_{\rm vir}$ includes physics of the high redshift galaxy formation. If there is no radiative feedback, atomic cooling is thought to become effective at $T_{\rm vir}$=10^4K. Hydrogen molecule cooling becomes effective below this temperature. If stars or star forming galaxies begin to form in a halo and radiative feedback by such objects exists, virial temperature is expected to become higher since radiative feedback such as the photodissociation of H_2 prevents the gas from cooling (see sec3.2.2)[122]. On the other hand, positive feedback such as enhancement of H_2 molecules due to increase of electrons pushes decrease of virial temperature because cooling becomes more effective. We parameterize $T_{\rm vir}$ as a responsible parameter for uncertainties in radiative feedback effects referred above.

We show the parameter dependence of equilateral type of the 21 cm bispectrum as function of redshift in Fig.7.1. We adopt $\zeta = 15(fiducial), 20, 25$ and $T_{\rm vir} = 10^4(fiducial), 3 \times 10^4, 5 \times 10^4$[K]. From Fig.7.1, we can see that the peak of the 21 cm bispectrum shifts to larger redshift for larger ζ. This is because larger ζ means that more more photons can contribute to ionization of neutral hydrogen gas. This leads to the progress of the EoR. We also notice that the peak of the 21 cm bispectrum shifts to lower redshift for higher $T_{\rm vir}$. Since higher $T_{\rm vir}$ corresponds to large mass of halo, the formation of halos capable to produce ionizing photons becomes difficult. As the result of this, the EoR is delayed and the peak shifts to lower redshift.

7.3 Fisher information matrix

In order to forecast constraint on the EoR model parameters, we use the Fisher information matrix $\mathbf{F}_{ij}$. Given observational data, the maximum likelihood analysis gives a set of parameters which maximize the likelihood function $\mathcal{L}$ (the probability distribution function for measured data set as function of model parameters). The Fisher formalism assumes that

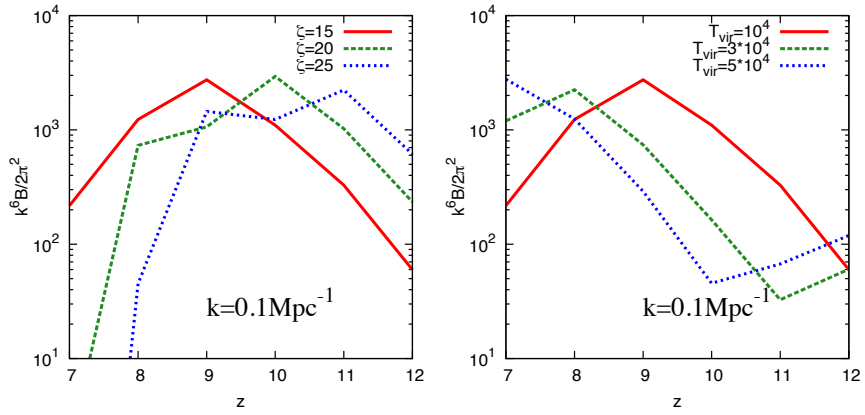

Figure 7.1: Equilateral type of the 21 cm bispectrum as function of redshift at $k = 0.1\mathrm{Mpc}^{-1}$ with varying $\zeta(left)$ and $T_{\rm vir}(right)$. We adopt $\zeta = 15(fiducial), 20, 25$ and $T_{\rm vir} = 10^4(fiducial), 3\times10^4, 5\times10^4$[K].

the likelihood function $\mathcal{L}$ follows a multi-dimensional Gaussian form in given parameters. By the Fisher analysis [22, 131], we can estimate the expected 1σ error for the model parameters with supposed instruments.

The Fisher matrix is defined as

$$\mathbf{F}_{ij} \equiv -\left\langle \frac{\partial^2 \ln \mathcal{L}}{\partial p_i \partial p_j} \right\rangle \Bigg|_{\vec{p}=\vec{p}_{\rm fid}} = \frac{1}{2}\left\langle \frac{\partial^2 \chi^2}{\partial p_i \partial p_j} \right\rangle \Bigg|_{\vec{p}=\vec{p}_{\rm fid}} \tag{7.1}$$

Where, $\vec{p}$ is the model parameter vector, $\vec{p} = (p_1, p_2, \cdots)$, and $\vec{p}_{\rm fid}$ is a set of fiducial model parameters, $\vec{p}_{\rm fid} = (p_{1,\rm fid}, p_{2,\rm fid}, \cdots)$. If we have N independent values for a certain physical value $x(\vec{p})$, the χ-squared value for $x(\vec{p})$ is given by

$$\chi^2(\vec{p}) = \sum_l^N \frac{[x_l(\vec{p}) - x_l(\vec{p}_{\rm fid})]^2}{\sigma_l^2} \tag{7.2}$$

σ_l is the observational error for $x_l(\vec{p})$. Noting that the Fisher matrix is evaluated at $\vec{p} = \vec{p}_{\rm fid}$, the Fisher matrix can be re-written by

$$\mathbf{F}_{ij} = \sum_l^N \frac{1}{\sigma_l^2} \frac{\partial x_i(\vec{p})}{\partial p_i} \frac{\partial x_i(\vec{p})}{\partial p_j} \Bigg|_{\vec{p}=\vec{p}_{\rm fid}} \tag{7.3}$$

In our case, we consider the Fisher matrix for the 21 cm power spectrum and the 21 cm bispectrum. The Fisher matrices for the 21 cm power spectrum and the 21 cm bispectrum are respectively given by

$$\mathbf{F}_{ij,\mathrm{PS}} = \sum_{l}^{N} \frac{1}{\sigma^2_{\mathrm{PS},l}} \frac{\partial P(k;\vec{p})}{\partial p_i} \frac{\partial P(k;\vec{p})}{\partial p_j}\bigg|_{\vec{p}=\vec{p}_{\mathrm{fid}}} \tag{7.4}$$

$$\mathbf{F}_{ij,\mathrm{BS}} = \sum_{l}^{N} \frac{1}{\sigma^2_{\mathrm{BS},l}} \frac{\partial B(k;\vec{p})}{\partial p_i} \frac{\partial B(k;\vec{p})}{\partial p_j}\bigg|_{\vec{p}=\vec{p}_{\mathrm{fid}}} \tag{7.5}$$

Here l expresses the l th bin of wave number. As one can see, in order to determine the Fisher matrices for both 21 cm power spectrum and 21 cm bispectrum, we need to estimate the errors on both 21 cm power spectrum and 21 cm bispectrum. We discuss the errors in next section. Given the Fisher matrix, we can estimate the expected 1-σ error of *i-th* parameter as follows:

$$\sigma_{p_i} = \sqrt{\mathbf{F^{-1}}_{ii}}, \tag{7.6}$$

and the covariance between *i-th* and *j-th* parameters is given by

$$\sigma_{ij} = \sqrt{\mathbf{F^{-1}}_{ij}}, \tag{7.7}$$

We will show the confidence regions of the EoR model parameters calculated by formalism above later. Note that the confidence regions obtained by the Fisher analysis include physically meaningless regions such as $T_{\mathrm{vir}} < 0$. This is because the Fisher analysis assumes the shape of χ^2 around fiducial values as quadratic form in term of the parameters [63]. In this case, we put on physically meaningful boundary condition for the confidence regions.

7.4 Thermal noise estimation

We estimate the thermal noise on both 21 cm power spectrum and 21 cm bispectrum to perform the Fisher forecast. First, we show the formalism to estimate the thermal noise for the 21 cm power spectrum based on [81]. Note that we assume probability distribution of the thermal noise for the brightness temperature obeys Gaussian shape.

Then, the thermal noise for the power spectrum is given by,

$$\begin{aligned}\delta P_N(k) &= \left[\sum_{\theta}\left(\frac{1}{P_N(k,\theta)/\sqrt{N_a}}\right)^2\right]^{-1/2} \\ &\approx \left[k^3 \int_{\arccos[\min(\frac{yk}{2\pi},1)]}^{\arcsin[\min(\frac{k_*}{k},1)]} d\theta\, \sin\theta \frac{\epsilon(n(k\sin\theta))^2 A_e^3 B^2 t_0^2}{(2\pi)^2 x^2 y \lambda^6 T_{\mathrm{sys}}^4}\right]^{-1/2},\end{aligned} \tag{7.8}$$

where P_N is the power spectrum of thermal noise, N_a is the number of pixels, k_* is the longest wave vector in transverse component corresponding to the maximum baseline length, λ is the observed wavelength, T_{sys} is the total system temperature, A_e is the effective area of antenna, B is the bandwidth, t_0 is total observing time and ϵ is constant factor set by 0.5. x and y are determined by cosmology(see [81]). The lower limit of the integral corresponds to the pixel size. In Fig.7.2, we show the scale dependence on both

21 cm power spectrum and thermal noise for various telescopes. Parameters for specifications of telescopes are shown in table 7.1.

redshift	8	10	12	17	$N_{\rm station}$
frequency [MHz]	158	129	109	79	
$T_{\rm sys}$ $[K]$	440	600	1000	1900	
A_e $[m^2]$ (MWA)	14	18	18	18	500
A_e $[m^2]$ (LOFAR)	512	600	900	900	24
A_e $[m^2]$ (HERA)	68	106	154	154	547
A_e $[m^2]$ (SKA)	462	728	962	962	866

Table 7.1: Parameters for telescopes: $T_{\rm sys}$ is the system temperature, A_e is the effective area of a station and $N_{\rm station}$ is the number of stations. The expanded MWA will have 500 antennae within a radius of 750 m with r^{-2} distribution [13]. LOFAR has 24 antennae within a radius of 2000 m with r^{-2} distribution [129]. HERA has 547 antennae within 200 m with constant distribution [102]. SKA will have 466 antennae within 600 m with r^{-2} distribution, 670 antennae within 1000 m, 866 antennae within 3000 m [26]. For simplicity, we assume that the antennae density is constant between 600 m to 1000 m and 1000 m to 3000 m, respectively. Further, we assume $t_0 = 1000$ hour for the total observing time and 6 MHz bandwidth.

Next, we estimate the thermal noise for the 21 cm bispectrum as similar as that for the power spectrum discussed above. The important point to note is that the bispectrum of thermal noise itself is actually zero because the thermal noise is assumed to be Gaussian distribution. Nonetheless, the variance of the noise bispectrum is non-zero and this contributes to the noise for the 21 cm bispectrum signal. The outline of derivation for the thermal noise contributing to the 21 cm bispectrum is almost similar as that for the power spectrum. The thermal noise due to the variance of the 21 cm bispectrum contributing to the 21 cm bispectrum signal is derived by [144] as

$$\begin{aligned}\delta B_N(k,K,\beta) &= \left[\sum_\theta \sum_\alpha \left(\frac{1}{\sqrt{N_a}}\sqrt{{\rm Cov}(B_1B_2)(k,K,\theta_1,\alpha)}\right)^{-2}\right]^{-1/2} \\ &= \frac{(2\pi)^{\frac{5}{2}}}{\sqrt{\Delta\theta_2}kK^{3/2}\epsilon}\left(\frac{x^2y\lambda^2}{A_e}\right)\left(\frac{T_{\rm sys}^2\lambda^2}{A_eBt_0}\right)^{\frac{3}{2}} \\ &\quad\times\left[\int d\theta_1\int d\alpha\sin\theta_1\sin\theta_2\sin\gamma(\theta_1,\alpha)\ n(\boldsymbol{k}_1)n(\boldsymbol{k}_2)n(\boldsymbol{k}_3)\right]^{-\frac{1}{2}}. \quad (7.9)\end{aligned}$$

For equilateral type of bispectrum, we set $K = k$ and $\beta = 2\pi/3$.

In Fig.7.3, we show the scale dependence of the 21 cm bispectrum with thermal noise estimated from the variance of the noise bispectrum for various telescopes.

From Figs.7.2 and 7.3, we can see that the noise increases at smaller scales in both bispectrum and power spectrum. This is because the number of baselines at smaller scales

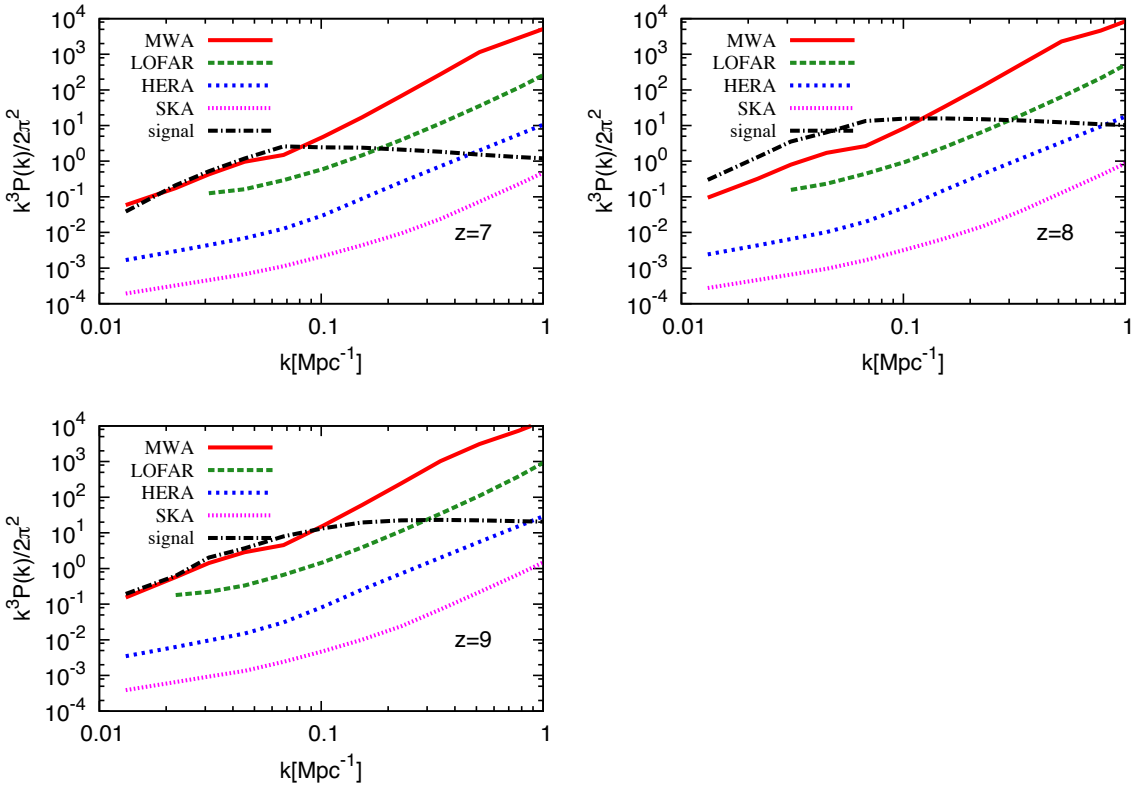

Figure 7.2: Comparison of the 21 cm power spectrum signal(dot-dashed line) with the thermal noise for various telescopes at z=7(*left top*), 8(*right top*), 9(*left bottom*). As supposed instruments, we choose MWA(solid line), LOFAR(long-dashed line), HERA(dotted line) and SKA(dashed line).

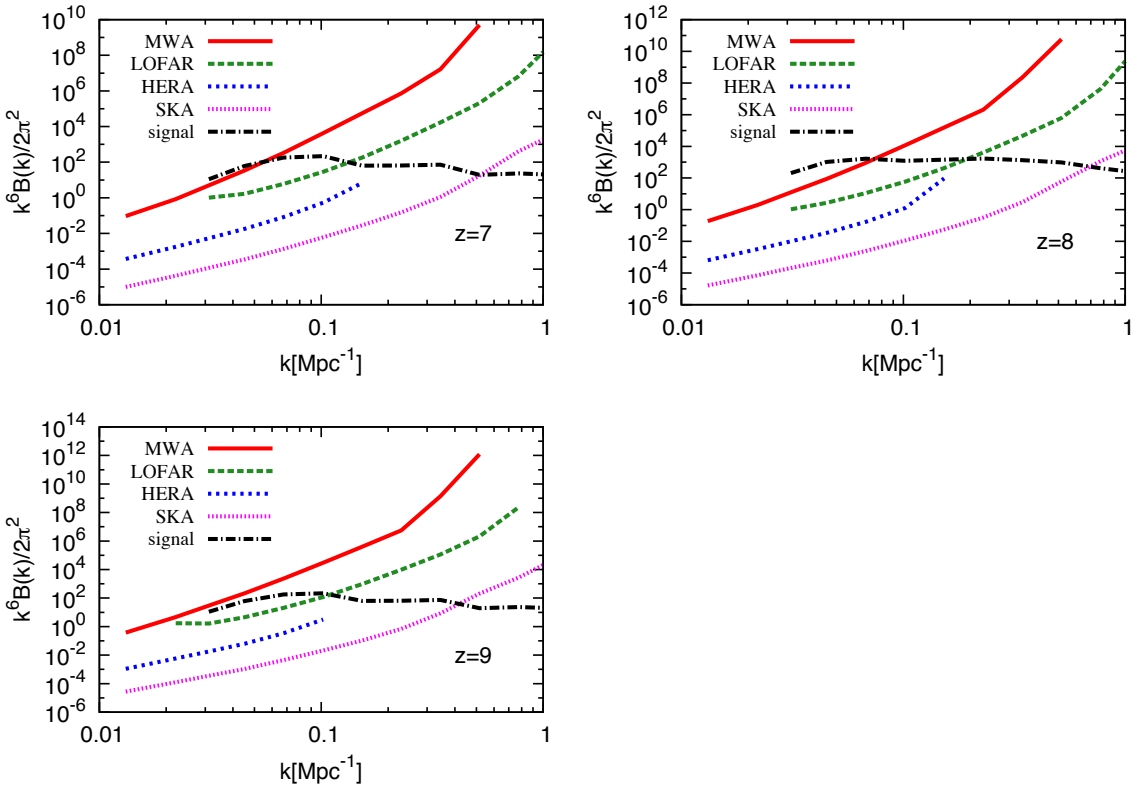

Figure 7.3: Comparison of the 21 cm bispectrum signal(dot-dashed line) with the thermal noise for various telescopes at z=7(*left top*), 8(*right top*), 9(*left bottom*). As supposed instruments, we choose the MWA(solid line), LOFAR(long-dashed line), HERA(dotted line) and SKA(dashed line).

corresponding to longer baseline is deficient. On the other hand, the sensitivity at large scales is limited by the field of view.

For both bispectrum and power spectrum noises, we cannot calculate the sensitivity at $k \lesssim 0.03\mathrm{Mpc}^{-1}$ for LOFAR telescope. This is because the number of antenna stations is small in the case of LOFAR telescope. Further, we notice that we also cannot calculate the bispectrum sensitivity at $k \gtrsim 0.2\mathrm{Mpc}^{-1}$ in the case of HERA telescope. The reason is that the number density of antennae outside core region in the case of HERA is small. Thus, triangles to be needed in order to calculate the bispectrum cannot be chosen by deficiency of antennae at small scales Compared the sensitivity for the power spectrum with that for the bispectrum, the signal to noise ratio in the case of the power spectrum is slightly larger that in the case of bispectrum. If we focus just on the sensitivity, the 21 cm power spectrum is more detectable than the bispectrum. However, estimation of the expected error does not depend on only sensitivity but also the rate of change for the power spectrum or bispectrum.

7.5 Result

We show the result of the Fisher analysis applying to the power spectrum and the bispectrum. Here, we focus on equilateral type of the bispectrum. As we referred before, we constrain the EoR model parameters assuming ongoing telescopes, MWA and LOFAR, to study how the bispectrum improves constraint on the EoR parameters. Note that we use both power spectrum and bispectrum for the Fisher analysis at k=0.03 -1.0 Mpc^{-1} divided into 13 bins.

First, we show constraints on the EoR model parameters obtained by both power spectrum and bispectrum at z=7, 8, 9 in Fig.7.4. The 1-σ contours obtained by the power spectrum assuming both MWA and LOFAR do not exclude $\zeta < 0$ and $T_{\mathrm{vir}} < 0$. These negative values are physically meaningless. Hence, we put on physically meaningful boundary condition on the parameter space and exclude negative value regions. Similarly, we put on same boundary condition for the contour obtained by the bispectrum assuming MWA.

As one can see, the constraint assuming LOFAR is tighter than that obtained by MWA in both power spectrum and bispectrum. This comes from that the sensitivity and resolution of LOFAR are better than those of MWA. The physical meaning of inclination of ellipse is referred as follows. If ζ becomes larger, neutral hydrogen atom is ionized more efficiently. Similarly, decreasing T_{vir} also drives progress of reionization. Both increasing ζ and decreasing T_{vir} play same role on reionization. Thus, these is degeneracy between these parameters. Although the degeneracies are not broken in the case of the power spectrum among z =7, 8, 9, the degeneracies among redshifts are broken in the case of the bispectrum.

Next, we compare constraint obtained by the power spectrum with that obtained by the bispectrum. We show the contours with 1-σ error in Fig.7.5 and show the values of 1-σ error for each telescope in Table.7.2. We also show the contours obtained by combination of the power spectrum with the bispectrum in Fig.7.5 and the values of 1-σ error in Table.7.3. We find that the constraints by the bispectrum are tighter than that by the power spectrum. We also find that LOFAR telescope puts on tighter constraints than MWA. We can see that the inclinations of contours are different between the power spectrum and the bispectrum.

This indicates that degeneracy is broken by combination of the power spectrum with the bispectrum.

z	7	8	9
$\sigma_{\zeta,\mathrm{PS}}$(MWA)	813	142	494
$\sigma_{\zeta,\mathrm{PS}}$(LOFAR)	171	20.2	65.0
$\sigma_{\mathrm{T_{vir}},\mathrm{PS}}$(MWA)	1.61×10^6	2.70×10^4	1.00×10^5
$\sigma_{\mathrm{T_{vir}},\mathrm{PS}}$(LOFAR)	3.39×10^5	3.91×10^4	1.31×10^5
$\sigma_{\zeta,\mathrm{BS}}$(MWA)	6.63	1.28	5.81
$\sigma_{\zeta,\mathrm{BS}}$(LOFAR)	0.819	0.0574	0.128
$\sigma_{\mathrm{T_{vir}},\mathrm{BS}}$(MWA)	8.22×10^3	2.37×10^3	8.22×10^3
$\sigma_{\mathrm{T_{vir}},\mathrm{BS}}$(LOFAR)	1.17×10^3	70.9	246

Table 7.2: 1-σ errors for ζ and $\mathrm{T_{vir}}$ estimated by the Fisher forecast applying to the power spectrum and the bispectrum.

z	7	8	9
$\sigma_{\zeta,\mathrm{combine}}$(MWA)	3.71	1.28	3.29
$\sigma_{\mathrm{T_{vir}},\mathrm{combine}}$(MWA)	6.17×10^3	2.37×10^3	7.95×10^3
$\sigma_{\zeta,\mathrm{combine}}$(LOFAR)	0.605	0.0574	0.128
$\sigma_{\mathrm{T_{vir}},\mathrm{combine}}$(LOFAR)	869	70.9	245

Table 7.3: Similar to Table.7.2, but these 1-σ errors are estimated by combination of the power spectrum with the bispectrum.

7.6 Discussion

In order to explore the EoR parameter region with MWA and LOFAR observations, we estimate expected 1-σ errors and constrain parameter region by the Fisher analysis with the 21 cm power spectrum and the bispectrum. First, we find that we can put tighter constraint on the EoR parameters with LOFAR than with MWA. This comes from that the thermal noise for LOFAR is lower than that for MWA and resolution of LOFAR is better than MWA. This means that the sensitivity of LOFAR is better than that of MWA. The difference of specification between MWA and LOFAR comes from effective area and maximum baseline length. Although the number density of antennae in core region for MWA is larger, larger effective area of LOFAR compensates deficiency of the less number density of antennae(eqs.(7.8) and (7.9) show how the thermal noise depends on effective area and on the number density of antennae).

Next, we find that the bispectrum can constrain the EoR parameters tighter than the power spectrum although signal to noise ratio of the power spectrum is better than that of the bispectrum. The reason why the bispectrum can give tight constraint is that derivative of the bispectrum with respect to the EoR parameters is much larger than that in the power spectrum. However, we know that the Fisher matrix can be determined by not only

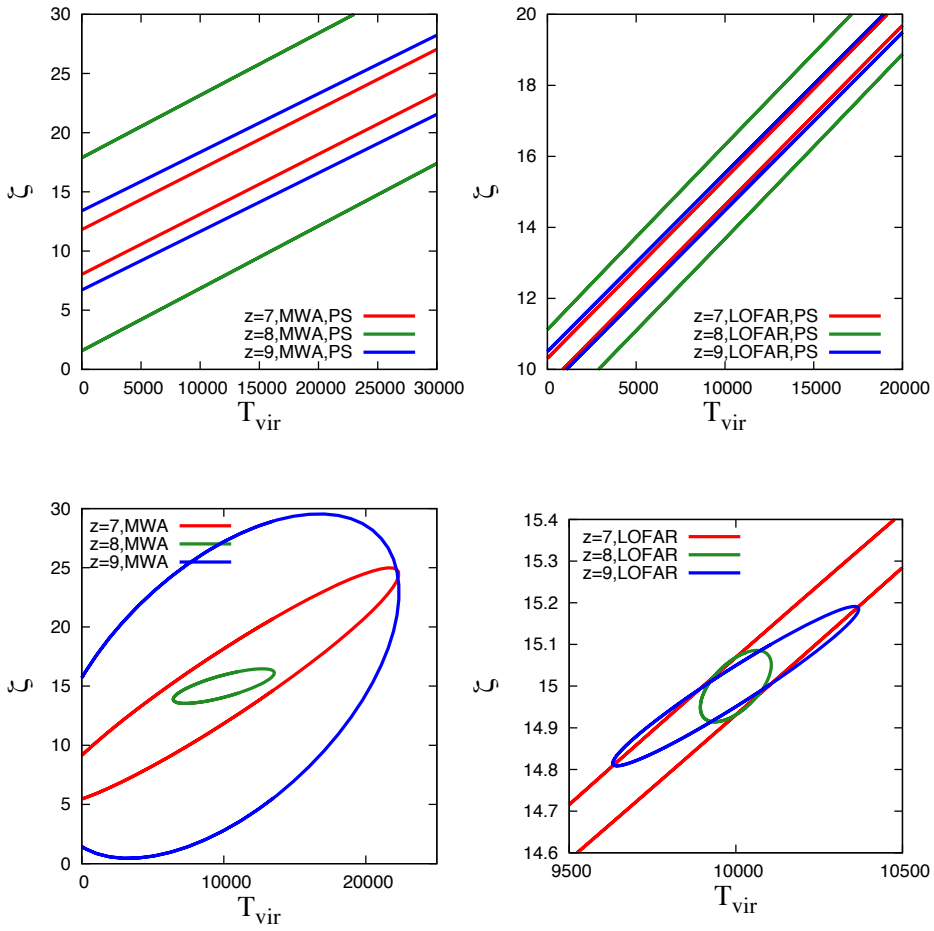

Figure 7.4: (*Top*) The 1-σ contours of the EoR model parameters obtained by the power spectrum assuming MWA(*left*) and LOFAR(*right*). (*Bottom*) Same one obtained by the bispectrum assuming MWA(*left*) and LOFAR(*right*). For both power spectrum and bispectrum, we focus on $z = 7, 8, 9$ where the cosmological 21cm signal expected to be detectable by MWA and LOFAR.

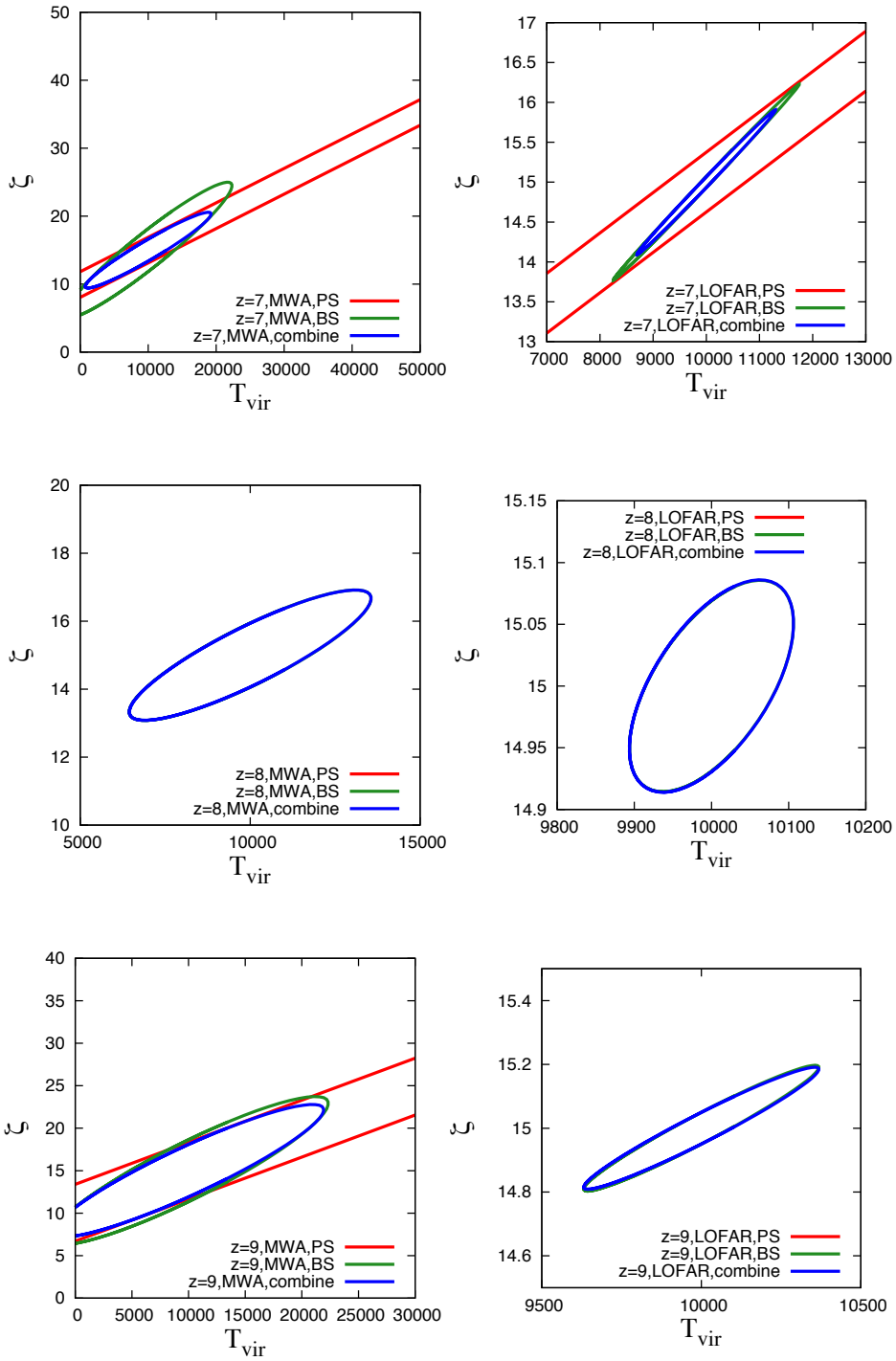

Figure 7.5: Similar to Fig.7.4, but these results are obtained by combining the power spectrum with the bispectrum at z=7(*top*), 8(*middle*), 9(*bottom*). At middle panels and right bottom panel, constraints from the power spectrum are too loose to be shown and constraint from the bispectrum determines expected error.

derivative of signal but also by the thermal noise. In order to study the balance between the derivative of the signal and the thermal noise, we show a ratio of square of derivative with respect to virial temperature and ionizing efficiency for the bispectrum and the power spectrum, $r = \left(\frac{\partial B}{\partial p_i}/\frac{\partial P}{\partial p_i}\right)^2$, and a ratio of square of the thermal noise error for MWA and LOFAR, $(\epsilon_P/\epsilon_B)^2$, in Fig.7.6. Both of them are function of wave number. Top of this figure implies that the derivative of the bispectrum with respect to both parameters is larger than that of the power spectrum ($r > 1$) except for the derivative with respect to virial temperature at z=7. Consequently, the derivative of the bispectrum contributes to the Fisher matrix more than that of the power spectrum (large Fisher matrix can put on tighter constraint). On the other hand, we can see how much the thermal error contributes to the Fisher matrix in the bottom of Fig.7.6. Although the signal of the bispectrum is larger than that of the power spectrum, the thermal noise of the bispectrum is also larger than that of the power spectrum. Therefore, an advantage of the large value of derivative of the bispectrum is offset by the thermal noise.

The difference among redshifts is remarkable for a ratio of the derivative. In particular, a ratio of the derivative is large at z=8,9 although there are slight differences for a ratio of the thermal noise among redshifts. From top and bottom of Fig.7.6, we notice that the dominant contribution to the Fisher matrix comes from larger scales ($k \lesssim 0.1\mathrm{Mpc}^{-1}$) since the thermal noise becomes smaller at larger scales. We also find that the Fisher matrix for the bispectrum becomes larger than that for the power spectrum by taking both derivative and thermal noise into account.

Finally, we find that the combination of the power spectrum with the bispectrum breaks degeneracy between $T_{\rm vir}$ and ζ in the case of MWA. While the constraint by combination of the bispectrum with the power spectrum with LOFAR is slightly improved than that obtained by the bispectrum only, the combination of the power spectrum with bispectrum with MWA gives tighter constraint more than that obtained by the bispectrum only. This can give tighter upper limit of ζ and $T_{\rm vir}$ than we perform the Fisher forecast by using the bispectrum or the power spectrum independently.

It should be emphasized that we ignore the sample variance and effect of foreground removal in our analysis for simplicity. In both case of the bispectrum and the power spectrum, the sample variance is thought to be effective at larger scales and foreground also affects larger scales[102]. Hence, we need to estimate these effects adequately to obtain more realistic results. This is our future work.

Some recent works forecast not only expected error on the EoR model parameters but also the parameters at the epoch of the X-ray heating[102, 52, 76, 92, 56, 33] based on the Fisher analysis or the Markov Chain Monte Carlo (MCMC) method for the power spectrum assuming PAPER. At SKA era, the constraint on the EoR model parameters will be improved compared with that at present. Therefore, we need to investigate whether the EoR model itself is valid as further step. The EoR model used in semi-numerical method is simple as introduced in sec 3.3. Hence, we actually need to include radiative feedback, recombination adequately in the EoR model. In order to do so, we have to perform numerical simulations for the process of reionization and should compare those results with observational data to get feedback from observations. We expect that semi-numerical approach such as 21cmFAST connects simulation results to observational data and that the parameter estimation also helps sophistication of the EoR model.

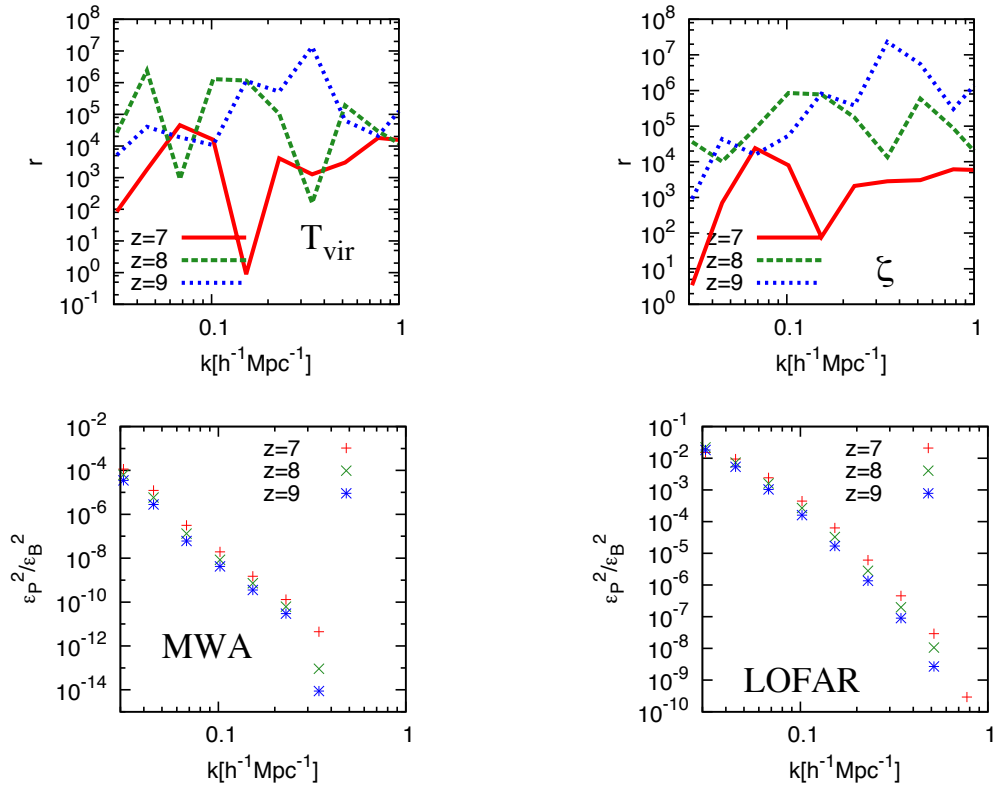

Figure 7.6: (*Top*) Ratio of square of the derivative of the bispectrum and the power spectrum with respect to virial temperature(*left*) and ionizing efficiency (*right*), $r = \left(\frac{\partial B}{\partial p_i} / \frac{\partial P}{\partial p_i}\right)^2$. (*Bottom*) the ratio of square of the thermal noise error for MWA(*left*) and LOFAR(*right*), $(\epsilon_P/\epsilon_B)^2$

Chapter 8

Conclusion

It has been expected that ongoing and upcoming radio interferometers would provide us with history of the Universe through the Dark Ages to the EoR via the 21 cm line signal from the IGM. For the coming eras in which we can observe the 21 cm line signal, we need to develop a method to extract information on the EoR and to understand physics around the EoR. Further, we have to investigate the detectability of the signal and estimate an expected error for the EoR model parameters to determine the EoR model accurately.

Considering the requirement above, we first studied the statistical properties of the cosmic 21 cm signal. In particular, we focused on the variance and skewness of the spin temperature as an indicator of the evolution of the thermal history. This is because various astrophysical processes such as the WF effect and the X-ray heating affect the spin temperature. In order to confirm that the spin temperature reflects effect of astrophysical processes, we studied the probability distribution function (PDF) of the spin temperature. We found that the skewness changes its sign when the X-ray heating becomes effective. This can be understood as follows: The spin temperature in neighborhood of the X-ray emitting sources approaches the kinetic temperature due to the WF effect. Hence, the PDF of the spin temperature has lower tails which correspond to the sources. And then, as the X-ray heating becomes effective, the spin temperature in neighborhood of sources starts to increase and tail shifts to higher value side. At the transition epoch where the X-ray heating becomes effective, the sign of the skewness changes from negative to positive. We also showed that the skewness at $z \sim 20$ would be detectable by next generation instrument such as SKA. Thus, we expect that skewness is a good indicator to investigate the epoch where the X-ray heating plays an important role.

Second, we investigated the 21 cm bispectrum, which is a higher order statistics to examine the non-gaussianity in the brightness temperature field due to various astrophysical processes. We actually calculated the scale and redshift dependence of the 21 cm bispectrum. We also calculated the components which consist of the 21 cm bispectrum (matter, the spin temperature and the neutral hydrogen fraction) and investigated the dependence of configuration of the 21 cm bispectrum. We found that the 21 cm bispectrum as function of redshift has a correlation between large and small modes in the squeezed-type while the equilateral and folded types of configuration basically trace the evolution of the 21 cm power spectrum. Further, we can know what component constituting of the 21cm bispectrum and configuration of the 21 cm bispectrum are remarkable at redshift we are interested in. We found following conclusions: At the EoR, the dominant component

and configuration of the 21 cm bispectrum come from the neutral hydrogen fraction with squeezed and folded type configurations. In particular, the effect of neutral hydrogen at large scales is prominent compared with that at small scales. From the Dark Ages to the pre-EoR, the dominant contribution comes from the spin temperature and matter components. At $z \sim 20$ where the X-ray heating begins, contributions from matter and the spin temperature are comparable.

Finally, we performed the Fisher analysis for the EoR model parameters, i.e, the virial temperature and ionizing efficiency, with the 21 cm bispectrum and the power spectrum. In this Thesis, we estimated expected the 1-σ error obtained by ongoing telescopes such as MWA and LOFAR. We found that the bispectrum can constrain the EoR model parameters more tightly than the power spectrum. In particular, this is remarkable in the case of assuming LOFAR telescope compared with MWA. In LOFAR telescope, the expected error is mainly determined by the bispectrum and the contribution from the power spectrum is quite small. In contrast, we found that combination of the power spectrum with the bispectrum assuming MWA telescope breaks degeneracy and puts on upper limit for both parameters although constraints are looser than that obtained by LOFAR. Consequently, we suggest that the 21 cm bispectrum is useful to constrain on the EoR model parameters and this helps to determine the model of the EoR and to understand physics of the EoR.

Our results are based on semi-numerical approach by using 21cmFAST for the calculation of the brightness temperature. Here, we briefly summarize the features of the 21cmFAST and discuss universality of what we found independent on the 21cmFAST. In the 21cmFAST, the evolution of matter fluctuations is calculated by the Zel'dovich approximation instead of performing a N-body simulation and identifying the spacial distribution of halos. However, we check that the matter fluctuations at scales less than $k \sim 5\mathrm{Mpc}^{-1}$ coincide with those obtained by N-body simulations. In our results, we focus on the scales less than $k = 1\mathrm{Mpc}^{-1}$. Thus, the Zel'dovich approximation is expected to be valid in our calculations. In order to judge whether a region is ionized or not, the 21cmFAST adopts an analytic method based on the excursion set formalism. For the ionization condition, this approach requires that the number of ionizing photons inside a region is larger than that of hydrogen atoms. The ionized bubble size distribution and the power spectrum produced by the 21cmFAST are in good agreement with those produced by radiative transfer simulations[88, 145]. Ionized bubbles are expected to be produced at overdense regions. The analytic model for the ionization field is based on biased matter fluctuations, which are calculated by the Zel'dovich approximation in our prescription. As we referred above, matter fluctuations calculated by the Zel'dovich approximation agree with those obtained by N-body simulations. Therefore, our results would be reliable for the statistical properties of ionized bubbles even if our calculation is based on semi-numerical approach. However, the semi-numerical method does not include the physics exactly needed to identify positions and the structure of the ionizing fronts. Thus, our results cannot refer to detailed physics of the EoR. Heating rate and Lyα background as well as ionization field also use an analytic model for calculation. In this analytic model, both the heating rate and the emissivity of Lyα photons are assumed to be proportional to the star formation rate density. This treatment may not be strictly precise and there are uncertainties(e.g. the properties of X-ray sources, distribution of heating sources, the epoch when heating of IGM occurs, initial mass function of first stars *etc*). However, we have a consensus on a scenario of the IGM thermal history as follows. After first stars form, WF effect becomes effective by Lyα

photons emitted by first stars and then the IGM is heated by X-ray photons. We found that skewness of the spin temperature changed its sign at the epoch when X-ray heating becomes effective independent on properties of heating sources. If the IGM thermal history is based on the scenario above, our discovery would be reliable because we confirm that our interpretation is reasonable by checking variance of the spin temperature, cross correlation between matter fluctuations and the spin temperature fluctuations, and probability distribution function of the spin temperature. All of them indicate that the epochs when heating becomes effective, obtained by them, are consistent with that obtained by skewness. Thus, our physical interpretation of skewness is thought to be reasonable although we have uncertainties of the epoch when WF effect and X-ray heating become effective attributed from uncertainties of the properties of heating sources. In addition to skewness, our interpretations related with the 21 cm bispectrum (such as redshift and configuration dependences of the 21cm bispectrum) would be reliable if we consider the standard thermal history scenario, although there are uncertainties of epochs when X-ray heating and reionization become effective.

We hope that the study in the Thesis can push forward the analysis of 21 cm signal brought by ongoing and upcoming observations and advance the understanding of physics at the EoR and the Dark Ages.

Appendix A

Relation between skewness and bispectrum

In this Appendix, we derive the relation between bispectrum and skewness. When we define the fluctuation of the brightness temperature δT_b as $\delta = (\delta T_b - \overline{\delta T_b})/\overline{\delta T_b}$, the skewness of the brightness temperature is defined by

$$\begin{aligned} \gamma &= \frac{1}{N}\sum_{i=1}^{N}(\delta T_{b,i} - \overline{\delta T_b}) \\ &= \frac{(\overline{\delta T_b})^3}{N}\sum \delta^3 \\ &= (\overline{\delta T_b})^3\langle\delta^3\rangle. \end{aligned} \tag{A.1}$$

Here N is the number of pixels. The definition of three-point correlation function for the brightness temperature ξ is expressed by $\xi(\mathbf{r}_1, \mathbf{r}_2) = \langle\delta(\mathbf{x})\delta(\mathbf{x}+\mathbf{r}_1)\delta(\mathbf{x}+\mathbf{r}_2)\rangle$. We can connect this three-point correlation function with ensemble average of δ^3 such as $\langle\delta^3\rangle = \xi(0,0)$. We know the relation between correlation function and bispectrum from Wiener-Khintchine relation described by

$$\xi(\mathbf{r}_1, \mathbf{r}_2) = \int \frac{d^3k_1}{(2\pi)^3}\int \frac{d^3k_2}{(2\pi)^3} e^{i(\mathbf{k}_1\cdot\mathbf{r}_1 + \mathbf{k}_2\cdot\mathbf{r}_2)} B(\mathbf{k}_1, \mathbf{k}_2, -\mathbf{k}_1 - \mathbf{k}_2). \tag{A.2}$$

Therefore, $\xi(0,0)$ can be expressed with bispectrum by

$$\xi(0,0) = \int \frac{d^3k_1}{(2\pi)^3}\int \frac{d^3k_2}{(2\pi)^3} B(\mathbf{k}_1, \mathbf{k}_2, -\mathbf{k}_1 - \mathbf{k}_2). \tag{A.3}$$

By using equation(A.2) and (A.3), we can obtain following one;

$$\gamma = (\overline{\delta T_b})^3 \int \frac{d^3k_1}{(2\pi)^3}\int \frac{d^3k_2}{(2\pi)^3} B(\mathbf{k}_1, \mathbf{k}_2, -\mathbf{k}_1 - \mathbf{k}_2), \tag{A.4}$$

This is the relation that connects skewness with bispectrum.

Bibliography

[1] Ali, Z. S., Parsons, A. R., Zheng, H., et al. 2015, ApJ, 809, 61

[2] Alpher, R. A., Bethe, H., & Gamow, G. 1948, Physical Review, 73, 803

[3] Alpher, R. A., & Herman, R. C. 1948, Physical Review, 74, 1737

[4] Baek. S, Semelin. B, Matteo. P. Di, Revaz. Y. Revaz and Combes. F arXiv:1003.0834 [astro-ph.CO].

[5] Barkana, R., & Loeb, A. 2001, Phys.Rep, 349, 125

[6] Barkana, R., & Loeb, A. 2004, ApJ, 609, 474

[7] Barkana, R., & Loeb, A. 2005, ApJ, 626, 1

[8] Barkana. R, & Loeb. A 2008, MNRAS, 384, 1069

[9] Bartolo.N, Komatsu.E, Matarrese.S and Riotto.S, Phys. Rept. **402**, 103 (2004) [astro-ph/0406398].

[10] Bennett, C. L., Banday, A. J., Gorski, K. M., et al. 1996, ApLL, 464, L1

[11] Bernardeau. F, Colombi.S, Gaztanaga.S and Scoccimarro. R Phys. Rept. **367**, 1 (2002) [astro-ph/0112551].

[12] Bond, J. R., Cole, S., Efstathiou, G., & Kaiser, N. 1991, ApJ, 379, 440

[13] Bowman, J. D., Morales, M. F., & Hewitt, J. N. 2006, ApJ, 638, 20

[14] Burles, S., Nollett, K. M., & Turner, M. S. 1999, arXiv:astro-ph/9903300

[15] Carilli. L. C, arXiv:1408.5317 [astro-ph.IM].

[16] Chapman, E., Zaroubi, S., & Abdalla, F. 2014, arXiv:1408.4695

[17] Chapman, E., Bonaldi, A., Harker, G., et al. 2015, Advancing Astrophysics with the Square Kilometre Array (AASKA14), 5

[18] Chen, X., & Miralda-Escudé, J. 2004, ApJ, 602, 1

[19] Chen, X., & Miralda-Escudé, J. 2008, ApJ, 684, 18

[20] Christian.P and Loeb.A, JCAP **1309** (2013) 014 [arXiv:1305.5541 [astro-ph.CO]].

[21] Ciardi, B., Inoue, S., Mack, K., Xu, Y., & Bernardi, G. 2015, Advancing Astrophysics with the Square Kilometre Array (AASKA14), 6

[22] Coe, D. 2009, arXiv:0906.4123

[23] Cooray. A Mon. Not. Roy. Astron. Soc. **363** (2005) 1049 [astro-ph/0411430].

[24] Cooray. A Phys. Rev. Lett. **97**, 261301 (2006) [astro-ph/0610257].

[25] Cooray. A, Li. C and Melchiorri.A Phys. Rev. D **77** (2008) 103506 [arXiv:0801.3463 [astro-ph]].

[26] Dewdney, P., Turner, W., Millenaar, R., McCool, R., Lazio, J. & Cornwell, T., 2013, "SKA1 System Baseline Design", Document number SKA-TEL-SKO-DD-001 Revision 1

[27] Dodelson.S, Modern cosmology, Academic Press

[28] Dicke, R. H., Peebles, P. J. E., Roll, P. G., & Wilkinson, D. T. 1965, ApJ, 142, 414

[29] Dillon, J. S., Liu, A., & Tegmark, M. 2013, Physical Review D, 87, 043005

[30] Dillon, J. S., Liu, A., Williams, C. L., et al. 2014, PRD, 89, 023002

[31] Eisenstein, D. J., Zehavi, I., Hogg, D. W., et al. 2005, ApJ, 633, 560

[32] Eisenstein, D. J., Weinberg, D. H., Agol, E., et al. 2011, The Astronomical Journal, 142, 72

[33] Ewall-Wice, A., Hewitt, J., Mesinger, A., et al. 2015, arXiv:1511.04101

[34] Fan. H. X, Carilli. L. C and Keating. B. G. Ann. Rev. Astron. Astrophys. **44** (2006) 415 [astro-ph/0602375].

[35] Fialkov. A, Barkana. A, Pinhas. A and Visbal. E, arXiv:1306.2354 [astro-ph.CO].

[36] Fialkov. A, Barkana. R and Visbal. E, arXiv:1402.0940 [astro-ph.CO].

[37] Fialkov, A., Barkana, R., & Cohen, A. 2015, Physical Review Letters, 114, 101303

[38] Fields, B. D. 2011, Annual Review of Nuclear and Particle Science, 61, 47

[39] Fixsen, D. J., Cheng, E. S., Gales, J. M., et al. 1996, ApJ, 473, 576

[40] Furlanetto, S. R., & Loeb, A. 2002, ApJ, 579, 1

[41] Furlanetto, S. R., Zaldarriaga, M., & Hernquist, L. 2004, ApJ, 613, 1

[42] Furlanetto, S. R., Zaldarriaga, M., & Hernquist, L. 2004, ApJ, 613, 16

[43] Furlanetto. S, Oh. P. S and Briggs. F, Phys. Rept. **433** (2006) 181 [astro-ph/0608032].

[44] Furlanetto, S. R., & Furlanetto, M. R. 2007a, MNRAS, 374, 547

[45] Furlanetto, S. R., & Furlanetto, M. R. 2007b, MNRAS, 379, 130

[46] Furlanetto. S and Loeb. A *The FIRST GALAXIES IN the Universe*, Princeton series in astrophysics, 2013

[47] Ghara. R, Choudhury. R. T and Datta. K. K, arXiv:1406.4157 [astro-ph.CO].

[48] Gamow, G. 1948, Physical Review, 74, 505

[49] Gleser. L, Nusser. A Ciardi. B, & Desjacques.V 2006, MNRAS, 370, 1329

[50] Gnedin, N. Y., Kravtsov, A. V., & Chen, H.-W. 2008, ApJ, 672, 765

[51] Greig, B., Mesinger, A., & Pober, J. C. 2015, arXiv:1509.02158

[52] Greig, B., & Mesinger, A. 2015, MNRAS, 449, 4246

[53] Gunn, J. E., & Peterson, B. A. 1965, ApJ, 142, 1633

[54] Guth, A. H. 1981, PRD, 23, 347

[55] Harker. J. A. G, Zaroubi. S, Thomas. M. R, Jelic. V, Labropoulos. P, Mellema. G, Iliev. I. T and Bernardi. G *et al.*, arXiv:0809.2428 [astro-ph].

[56] Harker, G. J. A., Mirocha, J., Burns, J. O., & Pritchard, J. R. 2015, arXiv:1510.00271

[57] Hasegawa, K., & Semelin, B. 2013, MNRAS, 428, 154

[58] Hirano, S., Hosokawa, T., Yoshida, N., et al. 2014, ApJ, 781, 60

[59] Hirata, C. M. 2006, MNRAS, 367, 259

[60] Hong.S. E, Ahn. K, Park. C et al. 2014, Journal of Korean Astronomical Society, 47, 49

[61] Hosokawa, T., Yoshida, N., Omukai, K., & Yorke, H. W. 2012, ApJL, 760, L37

[62] Hubble, E. 1929, Proceedings of the National Academy of Science, 15, 168

[63] Ideguchi, S., Takahashi, K., Akahori, T., Kumazaki, K., & Ryu, D. 2014, PASJ, 66, 5

[64] Iliev, I. T., Whalen, D., Mellema, G., et al. 2009, MNRAS, 400, 1283

[65] Iwata, I., Inoue, A. K., Matsuda, Y., et al. 2009, ApJ, 692, 1287

[66] Jelić, V., Zaroubi, S., Labropoulos, P., et al. 2008, MNRAS, 389, 1319

[67] Jelić, V., Zaroubi, S., Labropoulos, P., et al. 2010, MNRAS, 409, 1647

[68] Jeong, D., & Komatsu, E. 2009, ApJ, 703, 1230

[69] Joachimi, B., Shi, X., & Schneider, P. 2009, A&A, 508, 1193

[70] Komatsu. E *et al.* [WMAP Collaboration], Astrophys. J. Suppl. **192** (2011) 18 [arXiv:1001.4538 [astro-ph.CO]].

[71] Konno, A., Ouchi, M., Ono, Y., et al. 2014, ApJ, 797, 16

[72] Lacey, C., & Cole, S. 1993, MNRAS, 262, 627

[73] Lidz. A, Zahn. O, McQuinn. M, Zaldarriaga. M and Dutta. S, Astrophys. J. **659** (2007) 865 [astro-ph/0610054].

[74] Liu, A., Parsons, A. R., & Trott, C. M. 2014, PRD, 90, 023018

[75] Liu, A., Parsons, A. R., & Trott, C. M. 2014, PRD, 90, 023019

[76] Liu, A., & Parsons, A. R. 2015, arXiv:1510.08815

[77] Livio. Mario, Nature 479,7372,2011

[78] Lee. K. G, Cen. R, J. R., III. Gott, & H. Trac 2008, ApJ, 675, 8

[79] Loeb. A and Barkana. R, Ann. Rev. Astron. Astrophys. **39**, 19 (2001) [astro-ph/0010467].

[80] Loeb. A and Wyithe. S, Phys. Rev. Lett. **100**, 161301 (2008) [arXiv:0801.1677 [astro-ph]].

[81] McQuinn, M., Zahn, O., Zaldarriaga, M., Hernquist, L., & Furlanetto, S. R. 2006, ApJ, 653, 815

[82] McQuinn, M., Hernquist, L., Zaldarriaga, M., & Dutta, S. 2007,MNRAS, 381, 75

[83] Mao. Y, Tegmark. M, McQuinn. M, Zaldarriaga. M and Zahn. O, Phys. Rev. D **78**, 023529 (2008) [arXiv:0802.1710 [astro-ph]].

[84] Matsubara. T 現代宇宙論, 東京大学出版会, 2010

[85] Meiksin, A. 2000, Perspectives on Radio Astronomy: Science with Large Antenna Arrays, 37

[86] Mellema. G, Koopmans. L. V. E, Abdalla. F. A. et al 2013, Experimental Astronomy, 36, 235

[87] Mesinger. A and Furlanetto. S, arXiv:0704.0946 [astro-ph].

[88] Mesinger. A, Furlanetto. S, Cen. R,2011, MNRAS, 411, 955

[89] Mesinger. A, Ferrara. A and Spiegel. D. S arXiv:1210.7319 [astro-ph.CO].

[90] Mesinger. A, Ewall-Wice. A and Hewitt. J, 2014, MNRAS, 439,3262

[91] Mesinger, A., Ferrara, A., Greig, B., et al. 2015, Advancing Astrophysics with the Square Kilometre Array (AASKA14), 11

[92] Mirocha, J., Harker, G. J. A., & Burns, J. O. 2015, ApJ, 813, 11

[93] Miralda-Escudé, J., Haehnelt, M., & Rees, M. J. 2000, ApJ, 530, 1

[94] Muñoz, J. B., Ali-Haïmoud, Y., & Kamionkowski, M. 2015, arXiv:1506.04152

[95] Osterbrock. D. E, *Astrophysics of gaseous nebulae and active galactic nuclei*, University Science Books, 1989.

[96] Penzias, A. A., & Wilson, R. W. 1965, ApJ, 142, 419

[97] Pillepich. A, Porciani. C and Matarrese. S, Astrophys. J. **662** (2007) 1 [astro-ph/0611126].

[98] Planck Collaboration, Ade, P. A. R., Aghanim, N., et al. 2014, A& A, 571, A22

[99] Planck Collaboration, Aghanim, N., Arnaud, M., et al. 2015, arXiv:1507.02704

[100] Pober, J. C., Parsons, A. R., Aguirre, J. E., et al. 2013, ApJL, 768, L36

[101] Pober. D. C. J. J. C, Parsons. A. R. , Aguirre. J. E. , Ali. Z, Bowman. J, Bradley.R. F, Carilli. C. R and DeBoer. D.R *et al.*, arXiv:1408.3389 [astro-ph.CO].

[102] Pober. J. C, Liu. A, Dillon. A. J. S, et al. 2014, ApJ, 782, 66

[103] Press, W. H., & Schechter, P. 1974, ApJ, 187, 425

[104] Pritchard. J. R and Furlanetto. S. R, Mon. Not. Roy. Astron. Soc. **376** (2007) 1680 [astro-ph/0607234].

[105] Pritchard, J. R., & Furlanetto, S. R. 2006, MNRAS, 367, 1057

[106] Pritchard, J. R., & Loeb, A. 2012, Reports on Progress in Physics, 75, 086901

[107] Pritchard, J., Ichiki, K., Mesinger, A., et al. 2015, Advancing Astrophysics with the Square Kilometre Array (AASKA14), 12

[108] Robertson, B. E., Furlanetto, S. R., Schneider, E., et al. 2013, ApJ, 768, 71

[109] Robertson, B. E., Ellis, R. S., Furlanetto, S. R., & Dunlop, J. S. 2015, ApJL 802, L19

[110] Rottgering. H, New Astron. Rev. **47** (2003) 405 [astro-ph/0309537].

[111] Rybicki, George B., and Alan P. Lightman. *Radiative processes in astrophysics*. John Wiley & Sons, 2008.

[112] Santos. M. G, Amblard. A, Pritchard. J et al. 2008, ApJ, 689, 1

[113] Santos. M. G, Silva. M. B, Pritchard. J. R, Cen. R,& A. Cooray. 2011, A & A, 527, A93

[114] Sato, K. 1981, MNRAS, 195, 467

[115] Scoccimarro. R, Astrophys. J. **544**, 597 (2000) [astro-ph/0004086].

[116] Sefusatti. E, Crocce. M and Desjacques. V, Mon. Not. Roy. Astron. Soc. **406**, 1014 (2010) [arXiv:1003.0007 [astro-ph.CO]].

[117] Shimabukuro. H, Ichiki. K, Inoue. S, & Yokoyama. S 2014, PRD, 90, 083003

[118] Shimabukuro. H, Yoshiura. S, Takahashi. K, Yokoyama. S & Ichiki, K. 2015, Mon. Not. Roy. Astron. Soc. , 451, 4986

[119] Shimabukuro. H, Yoshiura. S, Takahashi. K, Yokoyama. S, & Ichiki. K 2015, arXiv:1507.01335

[120] Smoot, G. F., Bennett, C. L., Kogut, A., et al. 1992, ApJ letter, 396, L1

[121] Spergel, D. N., Verde, L., Peiris, H. V., et al. 2003, ApJS, 148, 175

[122] Sobacchi, E., & Mesinger, A. 2013, MNRAS, 432, 3340

[123] Sokasian, A., Yoshida, N., Abel, T., Hernquist, L., & Springel, V. 2004, MNRAS, 350, 47

[124] Steidel, C. C., Pettini, M., & Adelberger, K. L. 2001, ApJ, 546, 665

[125] Tegmark, M., Blanton, M. R., Strauss, M. A., et al. 2004, ApJ, 606, 702

[126] Tingay. S. J, Goeke. R, Bowman. J. D, Emrich. D, Ord. S. M, Mitchell. D. A, Morales. M. F and Booler. T *et al.*, arXiv:1206.6945 [astro-ph.IM].

[127] Trac, H., Cen, R., & Loeb, A. 2008, ApJL, 689, L81

[128] Trott, C. M., Wayth, R. B., & Tingay, S. J. 2012, ApJ, 757, 101

[129] van Haarlem, M. P., Wise, M. W., Gunst, A. W., et al. 2013, A&A, 556, AA2

[130] Venkatesan, A., Giroux, M. L., & Shull, J. M. 2001, ApJ, 563, 1

[131] Verde, L. 2010, Lecture Notes in Physics, Berlin Springer Verlag, 800, 147

[132] Verner, D. A., Ferland, G. J., Korista, K. T., & Yakovlev, D. G. 1996, ApJ, 465, 487

[133] Visbal. E, Barkana. R, Fialkov. A, Tseliakhovich. D and Hirata. C, arXiv:1201.1005 [astro-ph.CO].

[134] Watkinson. C. A and Pritchard. J. R, Mon. Not. Roy. Astron. Soc. **443**, 3090 (2014) arXiv:1312.1342 [astro-ph.CO].

[135] Watkinson, C. A., & Pritchard, J. R. 2015, arXiv:1505.07108

[136] Wise, J. H., & Cen, R. 2009, ApJ, 693, 984

[137] Wise, J. H., Abel, T., Turk, M. J., Norman, M. L., & Smith, B. D. 2012, MNRAS, 427, 311

[138] Wise, J. H., Demchenko, V. G., Halicek, M. T., et al. 2014, MNRAS, 442, 2560

[139] Wouthuysen. S. A, Astronomical Journal, 57,31

[140] Yajima, H., Choi, J.-H., & Nagamine, K. 2011, MNRAS, 412, 411

[141] Yokoyama. S, Matsubara. T, & Taruya. A 2014, PRD, 89, 043524

[142] Yoshida. N, Omukai. K, Hernquist. L, & T. Abel 2006, ApJ, 652, 6

[143] Yoshida, N., Omukai, K., & Hernquist, L. 2008, Science, 321, 669

[144] S. Yoshiura, H. Shimabukuro, K. Takahashi, et al. 2015, Mon. Not. Roy. Astron. Soc. 451, 4785

[145] Zahn, O., Mesinger, A., McQuinn, M., et al. 2011, MNRAS, 414, 727

[146] Zaroubi, S., Thomas, R. M., Sugiyama, N., & Silk, J. 2007, MNRAS, 375, 1269

[147] Zygelman, B. 2005, ApJ, 622, 1356